


12-2020

## Nuclear-targeted gold nanoparticles enhance the effects of radiation therapy with and without liposomal delivery

Maureen Aliru

Follow this and additional works at: [https://digitalcommons.library.tmc.edu/utgsbs\\_dissertations](https://digitalcommons.library.tmc.edu/utgsbs_dissertations)

 Part of the [Atomic, Molecular and Optical Physics Commons](#), [Biological and Chemical Physics Commons](#), [Lipids Commons](#), [Medicinal-Pharmaceutical Chemistry Commons](#), [Neoplasms Commons](#), [Other Medical Sciences Commons](#), [Quantum Physics Commons](#), and the [Radiation Medicine Commons](#)

### Recommended Citation

Aliru, Maureen, "Nuclear-targeted gold nanoparticles enhance the effects of radiation therapy with and without liposomal delivery" (2020). *The University of Texas MD Anderson Cancer Center UTHealth Graduate School of Biomedical Sciences Dissertations and Theses (Open Access)*. 1059.  
[https://digitalcommons.library.tmc.edu/utgsbs\\_dissertations/1059](https://digitalcommons.library.tmc.edu/utgsbs_dissertations/1059)

This Dissertation (PhD) is brought to you for free and open access by the The University of Texas MD Anderson Cancer Center UTHealth Graduate School of Biomedical Sciences at DigitalCommons@TMC. It has been accepted for inclusion in The University of Texas MD Anderson Cancer Center UTHealth Graduate School of Biomedical Sciences Dissertations and Theses (Open Access) by an authorized administrator of DigitalCommons@TMC. For more information, please contact [digitalcommons@library.tmc.edu](mailto:digitalcommons@library.tmc.edu).

NUCLEAR-TARGETED GOLD NANOPARTICLES ENHANCE THE EFFECTS OF  
RADIATION THERAPY WITH AND WITHOUT LIPOSOMAL DELIVERY

by

Maureen Lisa Aliru, BSBE.

APPROVED:



---

Sunil Krishnan, M.D.  
Advisory Professor



---

Junjie Chen, Ph.D.



---

Sang Hyun Cho, Ph.D.



---

Konstantin Sokolov, Ph.D.



---

R. Jason Stafford, Ph.D.

---

APPROVED:

---

Dean, The University of Texas  
MD Anderson Cancer Center UTHealth Graduate School of Biomedical Sciences

NUCLEAR-TARGETED GOLD NANOPARTICLES ENHANCE THE EFFECTS OF  
RADIATION THERAPY WITH AND WITHOUT LIPOSOMAL DELIVERY

A

DISSERTATION

Presented to the Faculty of

The University of Texas

MD Anderson Cancer Center UTHealth

Graduate School of Biomedical Sciences

in Partial Fulfillment

of the Requirements

for the Degree of

DOCTOR OF PHILOSOPHY

by

Maureen Lisa Aliru, B.S.

Houston, Texas

August, 2020

Copyright © 2020  
Maureen L. Aliru  
ALL RIGHTS RESERVED.

This dissertation or any portion thereof  
may not be reproduced or used in any manner whatsoever  
without the express written permission of the author.



*To my family back here and back home in Uganda, for your  
unremitting love, support, prayers and faith in me and the pursuit  
of my dreams.*

## **Acknowledgements**

I would like to express my deepest gratitude to my mentor and advisor, Sunil Krishnan. I am indebted to him for taking me under his wings in the lab and guiding me beyond the research. Sunil's zeal for science, passion for innovation, communication skills as a leader and scientist, meticulous attention to detail, and commitment to teaching and science have inspired me and will continue to do so. From an inexperienced rotating student, Sunil's guidance catalyzed my transformation to a better equipped scientist with higher intellectual wisdom and technical aptitude to tackle problems.

Similarly, my committee comprising of Sunil, Jason Stafford, Sang Hyun Cho, Konstantin Sokolov, Junjie Chen and formerly, Russell Broaddus offered constructive feedback when I started off my journey and helped shape the direction of this thesis endeavor. I am indebted to them, as well as members of the Krishnan Lab, past and present, for playing such a pivotal role in this time of my life. Tati, Monica, Allison, Carlos, Keith, Parmesh, Pankaj, Yuri, Bhanu, Lakshmi, Jessica and so many more. Maria Angelica Cortez and many more in neighboring labs all contributed their time, knowledge and friendship. Thank you Drs. Ramesh Tailor and Narayan Sahoo for the time put into radiation experiments. Altogether, I learned and came to appreciate the importance of patience, flexibility and resilience in research. The members of the Small Animal Imaging Facility (namely Charles Kingsley and Kiersten Maldonado), and the High-Resolution Electron Microscopy Facility (Kenneth Dunner Jr) were extremely resourceful given their experience and abundant knowledge in animal experiments and microscopy. The camaraderie displayed by lab members and the research staff was invaluable in constantly challenging me to develop and improve as an independent researcher.

I am indebted to my MD/PhD family and GSBS for their unwavering support from the start of my MD training, through my PhD and even to the start of residency. The guidance and support are unparalleled and more than I could expect for my time here. I'd also like to acknowledge the

Medical Physics program for accepting an MD/PhD student with a background mainly in medical sciences and taking a chance to allow me to see my thesis through. Thank you to Dr. Richard Wendt for the guidance and annual Christmas gifts to all the students. The friendships and understanding are what helped me through such a time. I don't believe I can mention everyone who has supported me and whose friendship has meant so much to me over this experience, please know that your presence made a difference for me. I'm fortunate to have met so many wonderful individuals and developed steadfast friendships.

Finally, I'd like to acknowledge my friends and family who have supported me for as long as I could remember, regardless of how far-fetched my ideas were/are at times. Bernard, thank you for the endless dinners and laughter during our game nights. Lekitta Nelson, words cannot describe our journey, and our unbreakable bond. Thank you for your patience, unwavering support. My mother who had the courage to move to a different continent with 3 young children, knowing she had a lifetime of hardship ahead, but enduring, nonetheless, to provide us with a better future. My brothers, Dennis and Derrick, who have been with me and grown up to be amazing human beings in their own right, I'm so very proud of you. Aunt Regina, thank you for taking me in and just being my rock, regardless of what else is happening in the world. This is for you all. I am so incredibly fortunate to have been blessed with the family and friends I have, and honored to exist at the very same moment of time as you. I am grateful I get to spend this life with you all by my side. I look forward to more adventures with you. Thank you!

# NUCLEAR-TARGETED GOLD NANOPARTICLES ENHANCE THE EFFECTS OF RADIATION THERAPY WITH AND WITHOUT LIPOSOMAL DELIVERY

Maureen Lisa Aliru, B.S.B.E.\*

Advisory Professor: Sunil Krishnan, M.B.B.S., M.D.

Less than 10% of pancreatic cancer patients are eligible for curative resection, and clinical trials evaluating chemoradiation in locally advanced patients with unresectable disease have been largely disappointing. New and creative therapeutic approaches are needed to address the unmet need for treatment options. The objective of this thesis is to advance radiosensitization of treatment-resistant densely desmoplastic pancreatic cancer using nanoparticles to surmount biological barriers to effective particle distribution for DNA-targeting.

Clinical translation of radiosensitizing nanoparticles has stalled owing to technical challenges. Current strategies to use AuNPs for radiosensitization require large quantities of gold, kilovoltage x-rays, immediate irradiation after intravenous administration, and repetitive administrations of AuNPs prior to each radiation dose during a course of fractionated radiotherapy. To overcome these challenges, the next generation of AuNPs should be engineered with 2 design criteria: compatibility with multiple radiation platforms, and appropriate *in vivo* biodistribution for radiation dose enhancement at low gold quantities.

To address this, nuclear-targeted gold nanoparticles (nAuNPs) are developed as payloads for the thermosensitive liposomes (TSLs). The nAuNP-loaded liposomes are biocompatible carriers capable of penetrating the biophysical barriers and reach deep inside the tumor. Non-invasive thermal stimulation then releases the nanoparticle load at the intended site of cellular uptake. The nuclear targeting of gold nanoparticles enhances the local effects of

radiation via generation of short-range secondary electrons in the proximity of the DNA in aggressive cancer clones.

To test nAuNPs as a radiosensitizing payload of the TLSs, a three-phase plan is presented. Phase I focuses on AuNP cellular distribution, demonstrating signal specific nuclear localization. Phase II appraises radiosensitizing effects of nAuNPs *in vitro*. Finally, Phase III demonstrates *in vivo* biodistribution and anti-tumor efficacy of the nAuNPs with and without TLSs in xenograft models of human pancreatic adenocarcinoma. This 3-phase study advances triggered-release of nuclear-targeted nanoparticles as a radiosensitizing modality for localized cancer therapy. This work provides a framework for the development of a readily deployable class solution for radiosensitization in a variety of tumors.

## **Table of Contents**

<b>Copyright</b>	iii
<b>Dedications</b>	iv
<b>Acknowledgements</b>	v
<b>Abstract</b>	vii
<b>Table of contents</b>	ix
<b>List of Illustrations</b>	xi
<b>List of Tables</b>	xiii
<b>Abbreviations</b>	xiv

## **Chapter I: Background and Motivation**

1.1 Pancreatic cancer	1
1.2 Radiation therapy	8
1.3 Nanotechnology	14
1.4 Thesis overview	21

## **Chapter II: Cellular nanoparticle distribution**

2.1 Abstract	23
2.2 Introduction	24
2.3 Results and Discussion	26
2.4 Conclusion	45
2.5 Supporting Information	47
2.6 Materials and Methods	49

### **Chapter III: *in vitro* radiosensitization**

3.1 Abstract	51
3.2 Introduction	52
3.3 Results and Discussion	54
3.4 Conclusion	75
3.5 Supporting Information	77
3.6 Materials and Methods	79

### **Chapter IV: *in vivo* biodistribution and anti-tumor efficacy**

4.1 Abstract	81
4.2 Introduction	83
4.3 Results and Discussion	85
4.4 Conclusion	99
4.5 Supporting Information	101
4.6 Materials and Methods	102

### **Chapter V: Summary**

### **Appendix – Common methods**

### **Bibliography**

### **Vitae**

## List of Illustrations

### Chapter I

Figure 1.1: Pancreatic cancer development	2
Figure 1.2: Diagnostic computed tomography (CT) of pancreatic cancer	3
Figure 1.3: Electromagnetic spectrum	9
Figure 1.4: DNA damage schematic	12
Figure 1.5: Size comparison of nanoparticles	15
Figure 1.6: Design considerations for nanoparticle synthesis	18
Figure 1.7: Graphical thesis overview	22

### Chapter II

Figure 2.1: Chapter II graphical overview	24
Figure 2.2: AuNS synthesis and characterization	27
Figure 2.3: Spectrophotometric analysis of AuNS	28
Figure 2.4: Size evaluation of AuNSs	31
Figure 2.5: Surface charge evaluation of AuNSs	32
Figure 2.6: AuNS uptake and cytotoxicity	35
Figure 2.7: MiaPaCa-2 AuNS localization	38
Figure 2.8: Panc-1 AuNS localization	39
Figure 2.9: Subcellular localization of AuNSs	41
Figure 2.10: Subcellular localization of AuNSs in Panc-1 cells	42
Figure 2.11: Subcellular localization of AuNSs in MiaPaCa-2 cells	43
Figure 2.12: AuNS mass spectrometry imaging	47
Figure 2.13: EDX analysis of unconjugated and conjugated AuNS	48



### Chapter III

Figure 3.1: Chapter III graphical representation	52
Figure 3.2: Clonogenic survival analysis	56
Figure 3.3: Reactive oxygen species production	59
Figure 3.4: DNA DSB evaluation	61
Figure 3.5: COMET assay	63
Figure 3.6: Split dose clonogenic assay	65
Figure 3.7: Cell cycle analysis: HPDE	68
Figure 3.8: Cell cycle analysis: Panc-1	69
Figure 3.9: Cell cycle analysis: MiaPaCa-2	70
Figure 3.10: Seahorse assay for cellular metabolism	72
Figure 3.11: TMRE assay	74
Figure 3.12: Identification of primary objects	77
Figure 3.13: Representative cell cycle histograms	78

### Chapter IV

Figure 4.1: Graphical representation of chapter IV studies	82
Figure 4.2: AuNS biodistribution studies.	86
Figure 4.3: <i>In vivo</i> AuNS toxicity.	88
Figure 4.4: Panc-1 TDG studies.	90
Figure 4.5: <i>In vivo</i> MiaPaCa-2 tumor growth delay and survival studies.	92
Figure 4.6: TSL characterization and release kinetics.	94
Figure 4.7: TSL biodistribution.	96
Figure 4.8: <i>In vivo</i> tumor growth delay with TSLs.	98
Figure 4.9: TSL synthesis schematic.	101

## Chapter V

Figure 5: Chapter V graphical summary.

97

### List of Tables

Table 1.1: Pancreatic cancer staging definitions	5
Table 2.1: AuNS characterization	29
Table 2.2: Stability of AuNS formulations per UV-Vis spectra	30
Table 2.3: Size stability of AuNS formulations per DLS	31
Table 2.4: Surface charge stability of AuNS formulations per zeta potential	32
Table 3.1: Dose enhancement factors and radiobiological effectiveness	55
Table 3.2: Radiation enhancement factors as a function of LET	58
Table 3.3: Recovery ratios for split dose assay.	65

## Abbreviations

ATP	Adenosine triphosphate
AuNP(s)	Gold nanoparticle(s)
AuNS(s)	Gold nanosphere(s)
pAuNS	PEGylated gold nanosphere
sAuNS	Gold nanosphere conjugated with scrambled peptide
nAuNS	Gold nanosphere conjugated with nuclear localization sequence
BCA	Biocinchoninic acid, mBCA – microBiocinchoninic acid
CPP	Cell penetrating peptide
CTAB	Cetyltrimethylammonium bromide
DAPI	4',6-diamidino-2-phenylindole
DF	Dark field microscopy
DLS	Dynamic light scattering
DMEM	Dulbecco's Modification of Eagle's Medium
EDX	Energy-dispersive X-ray spectroscopy
EPR	Enhanced permeability and retention
FBS	Fetal bovine serum
Gy	Gray (J/kg)
HIV	Human immunodeficiency virus
HPDE	Human pancreatic ductal epithelial cells
HR	Homologous recombination
ICP-MS	Inductively coupled plasma mass spectrometry
kDa	Kilodalton
LET	Linear energy transfer
LINAC	Linear accelerator
LM	Light microscopy

MDA	MD Anderson Cancer Center
MTT	3-(4,5-dimethylthiazol-2-yl)-2,5-diphenyltetrazolium bromide
NAD(P)H	Nicotinamide adenine dinucleotide phosphate
NES	Nuclear export sequence
NHEJ	Non-homologous end joining
NLS	Nuclear localization sequence
NPC	Nuclear pore complex
OD	Optical density
PFA	Paraformaldehyde
PBS	Phosphate buffered saline (1x)
PE	Plating efficiency
PEG	Poly (ethylene glycol)
RBE	Radiobiological effectiveness
RGD	Arginylglycylaspartic acid
rt	Room temperature
RT	Radiation Therapy
SD	Standard deviation
SE	Standard error
SF	Surviving fraction
SPR	Surface plasmon resonance
RME	Receptor-mediated endocytosis
TGD	Tumor growth delay
TEM	Transmission electron microscopy
TMRE	Tetramethylrhodamine, ethyl ester
UV-Vis	Ultraviolet-visible

# **Chapter I: Background and motivation**

## **1.1 Pancreatic cancer**

### **Natural history and pathology**

Pancreatic cancer is a disease that presents both diagnostic and treatment challenges. It is currently the fourth leading cause of cancer mortality in the US and slated to become the second by 2030.[1, 2] The first attempted account of pancreatic cancer by Giovanni Battista Morgagni in 1761 reported lesions in the pancreas that were largely unsubstantiated due to the lack of histological analysis at that time.[3] Jacob Mendez Da Costa later revised Morgagni's original work and recorded several cases, one of which actually reported a microscopic diagnosis of adenocarcinoma.[4] Several decades later, this was followed by the advent of resection attempts in the form of pancreaticoduodenectomies which were subsequently popularized as the Whipple procedure.[5-10] As discussed later, this type of surgery described in the 20<sup>th</sup> century still persists as the only potentially curative treatment option for pancreatic cancer in 2019 despite the advancements in diagnostic and treatment techniques.

Pathologically, pancreatic cancer is described as an adenocarcinoma that develops from the ductal epithelium of the exocrine portion of the gland. Ductal adenocarcinoma is the most common neoplasm, accounting for 85% of pancreatic lesions. Although the literature describes no direct causative factors of pancreatic cancer, the most frequently linked risk factors include family history, smoking, diabetes mellitus, obesity, chronic pancreatitis and the presence of cysts.[11] Briefly, pancreatic cancer progresses through precursor lesions characteristically described as pancreatic intraepithelial neoplasias (PanINs), which cultivate clonal genetic and epigenetic alterations.(Fig. 1.1) Less frequently, pancreatic cancer can evolve from mucinous cystic lesions that advance into intraductal papillary mucinous neoplasms (IPMNs).[12]

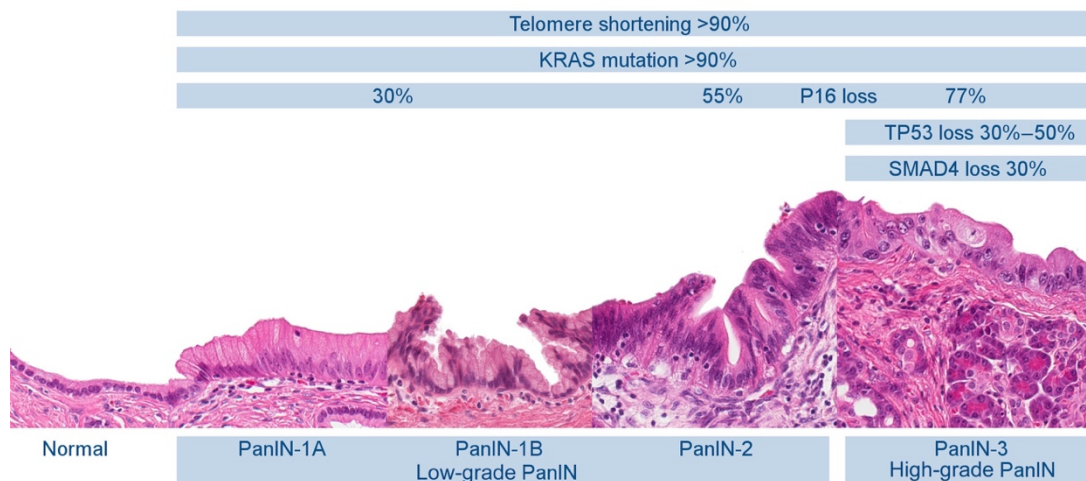


Figure 1.1: Pancreatic cancer development. Progression through the stages of pancreatic intraepithelial neoplasias (PanINs) associated with increasing cellular atypia. PanIN-1 represents minimal atypia progressing to formation of micropapillae. There is loss of cellular polarity in PanIN-2, and PanIN-3 demonstrates severe nuclear and architectural atypia. Figure reprinted with permission from publisher. *Noe M, Brosens LA. Pathology of Pancreatic Cancer Precursor Lesions.*[13]

## Clinical presentation and diagnosis

Symptoms of pancreatic cancer commonly appear later in the course of the disease, which is evidenced by the difficulty of early detection and limited curative treatment options. The majority of patients present with tumors in the head of the pancreas which cause common bile duct compression with increasing tumor size. This results in obstructive jaundice causing patients to notice pale-colored stools, dark urine, yellowing of the skin and conjunctival icterus. Due to the decreased production of pancreatic enzymes, patients usually can experience weight loss, as well as new onset type 2 diabetes mellitus. With more advanced disease, patients can present with abdominal pain radiating to the back which can be indicative of nerve involvement by the tumor. Altogether, the physical examination is non-specific for pancreatic cancer but may incite additional diagnostic tests given patient demographics and previously mentioned risk factors.[14]

The next step in management usually involves imaging by means of computed tomography (CT) with a pancreatic protocol. This allows for visualization of the primary tumor with respect to surrounding organs and blood vessels, as well as any disease metastasis. The tumor typically appears as a poorly enhancing lesion with low attenuation on CT in comparison to surrounding tissues. (Fig. 1.2) Additional imaging modalities that may prove useful include magnetic resonance imaging (MRI) or endoscopic ultrasound (EUS). Once diagnosed using CT, the treatment team usually proceeds with an EUS with fine needle aspiration (FNA) for cytological confirmation of tumor diagnosis. Carbohydrate antigen 19-9 (CA 19-9) is the only US Food and Drug Administration (FDA) approved biomarker for pancreatic cancer and is usually tested for at diagnosis. CA 19-9 is a sialylated Lewis (a) antigen with a reported sensitivity and specificity of roughly 80%.[15] Although beneficial for following disease progression and response to treatment, CA 19-9 is currently not recommended for screening due to its low positive predictive value.

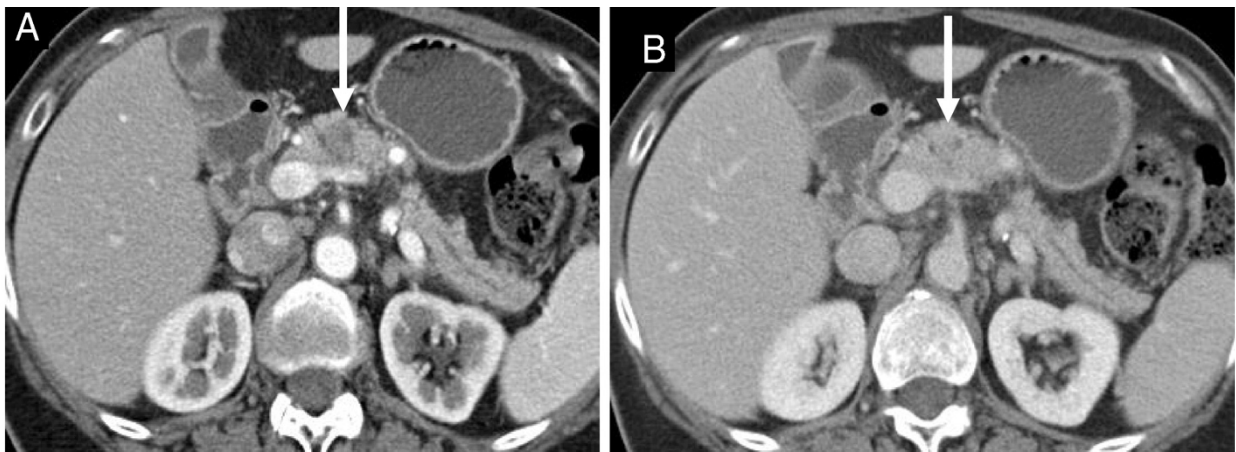


Figure 1.2: Computed tomography (CT) of pancreatic cancer for diagnosis. Contrast enhanced axial images in: (A) parenchymal phase showing a low-attenuation mass in the body of the pancreas and (B) venous phase demonstrating isointense mass relative to surrounding parenchyma. Figure reprinted with permission from publisher. Yeh R, Steinman J, Luk L, Kluger MD, Hecht EM. *Imaging of pancreatic cancer: what the surgeon wants to know*. [16]

Prognosis and treatment for pancreatic cancer is usually based upon the TNM staging. This classification system categorizes patients into one of 3 stages: resectable, locally advanced or metastatic disease (Table 1).[17-19] With CT imaging providing 70-85% accuracy for resection prediction, a positron emission tomography (PET) scan can be useful to determine suspected metastatic disease.[20-22] Additionally, a laparoscopy can be performed to examine the peritoneum and abdomen in some cases of tumor occurrence in the pancreatic body or tail. The median survival is 17-23 months for patients presenting with resectable disease treated with adjuvant chemotherapy, 8-14 months for patients presenting with locally advanced pancreatic cancer, and 4-6 months for patients who present with metastatic disease.[23] Furthermore, some patients with resectable disease fall into a subcategory of technically resectable status, but carry a high risk of a margin-positive resection due to the degree of vascular involvement.



Table 1: Pancreatic cancer staging definitions per the 7<sup>th</sup> and 8<sup>th</sup> editions of the TNM system by AJCC/UICC. Table adapted from AJCC guidelines.

		7 <sup>th</sup>				Stage	8 <sup>th</sup>			
	T1	Tumor limited to pancreas, ≤ 2cm in greatest dimension	T	N	M		T	N	M	Maximum tumor diameter ≤ 2cm
	T2	Tumor limited to pancreas, > 2cm in greatest dimension	T1	N0	M0	<b>IA</b>	T1	N0	M0	Maximum tumor diameter > 2, ≤ 4cm
	T3	Tumor extends beyond pancreas, no involvement of celiac axis or SMA	T2	N0	M0	<b>IB</b>	T2	N0	M0	Maximum tumor diameter > 4cm
	T4	Tumor involves celiac axis or SMA (unresectable)	T3	N0	M0	<b>IIA</b>	T3	N0	M0	Tumor involves celiac axis, CHA or SMA
	N0	No regional lymph node metastasis	T1-3	N1	M0	<b>IIB</b>	T1-3	N1	M0	No regional LN metastasis
	N1	Regional lymph node metastasis	T4	Any N	M0	<b>III</b>	T4 (Any T)	Any N (N2)	M0	Metastasis in 1-3 regional lymph nodes
	N2	–	Any T	Any N	M1	<b>IV</b>	Any T	Any N	M1	Metastasis in ≥ 4 regional lymph nodes
	M0	No distant metastasis								No distant metastasis
	M1	Distant metastasis								Distant metastasis

\*AJCC – American Joint Committee on Cancer; UICC – Union for International Cancer Control; SMA – superior mesenteric artery

## **Treatment strategies**

Surgery, chemotherapy and radiation are the backbones of pancreatic cancer treatment. The current standard of care for early-stage disease is surgery and adjuvant therapy. Surgery is determined by the anatomic location of the tumor with a pancreaticoduodenectomy (Whipple) performed for lesions confined to the head of the pancreas, and a distal pancreatectomy for lesions in the body or tail. Although previously investigated for treatment of pancreatic tumors, total pancreatectomies are generally reserved for patients with large or multilocular tumors due to the high rate of post-operative complications.[24] Several trials such as GITSG, ESPAC-3, RTOG 9704 and many more established the survival advantage of adjuvant chemotherapy when compared to observation.[25-29] These studies looked at chemotherapy regimens consisting of 5-fluorouracil (5-FU) and gemcitabine).

For locally advanced pancreatic cancer (LAPC), however, there are several on-going trials to establish the best treatment strategy for these patients. Chemoradiation options with gemcitabine reported down-staging of roughly 30% for patients with LAPC to resectable disease, allowing for resection and leading to median survival similar to those patients presenting with resectable disease.[23] Newer chemotherapy regimens such as FOLFIRINOX (combination 5-FU, irinotecan and oxaliplatin) and Abraxane (liposomal formulation of paclitaxel) have also shown improved survival in this patient population.[19] In the metastatic setting, a combination of the aforementioned chemotherapy regimens with or without erlotinib has also shown promise.

As previously discussed, only a minority of patients, less than 10%, present with disease amenable to a margin-negative resection, the only potentially curative treatment for pancreatic cancer. Even with this curative-intent surgery, the 5-year overall survival rate is only 15-25%.[30] Among patients with locally advanced pancreatic cancer (LAPC) where the tumor has not metastasized but involves retroperitoneal vascular structures that preclude surgical resection, roughly 60-70% achieve a short-lived partial response with a progression-free survival range of 4-6 months after chemoradiation therapy (CRT), an even smaller subset (<15%) are adequately

down staged for potential resectability.[31, 32] Contrary to the common perception that all patients with pancreatic cancer succumb to the disease as a result of distant metastasis, recent evidence reveals that complications from local tumor progression significantly contribute to disease-related mortality even with standard dose CRT.[33] Consequently, there is a pressing need for selective enhancement of tumor responses to local therapies; and besides surgery, RT is the only other form of localized therapy for pancreatic cancer.

## 1.2 Radiation therapy

### Radiation physics

Aforementioned, radiation therapy (RT) is one of the cornerstones of cancer therapy, and one of the only forms of truly localized therapy in pancreatic cancer. The inception of RT followed Roentgen's discovery of X-rays in 1895, and Becquerel's discovery of radioactivity in 1896. Since then, technological advances in X-ray production have aimed at higher energies, intensities, different particle types, improved treatment planning and delivery methods, such as intensity modulated beams. In RT, penetrating radiation is emitted from either radioactive sources, also known as brachytherapy, or delivery apparatuses such as linear accelerators (LINACs). RT is sometimes delivered using special accelerators and exotic particles such as protons, neutrons,  $\pi$  mesons and other heavy ions.[34]

Radiation is categorized into two major classes based on its capacity to ionize matter: non-ionizing and ionizing radiation – Fig. 1.3.[35] Apparent by the name, non-ionizing radiation cannot ionize matter. Ionizing radiation either directly ionizes matter via charged particles such as electrons, protons, alpha particles and heavy ions, or indirectly ionizes through neutral particles such as neutrons and photons – X-rays or gamma rays.[34, 36] Through Coulomb interactions, directly ionizing radiation particles deposit energy through the charged particle to orbital electrons of atoms in the medium. Indirectly ionizing particles, however, first produce charged particles, e.g. photons causing release of electron or positrons, which then deposit energy through direct Coulomb interactions. Both forms of radiation are used for clinical management of malignant diseases.

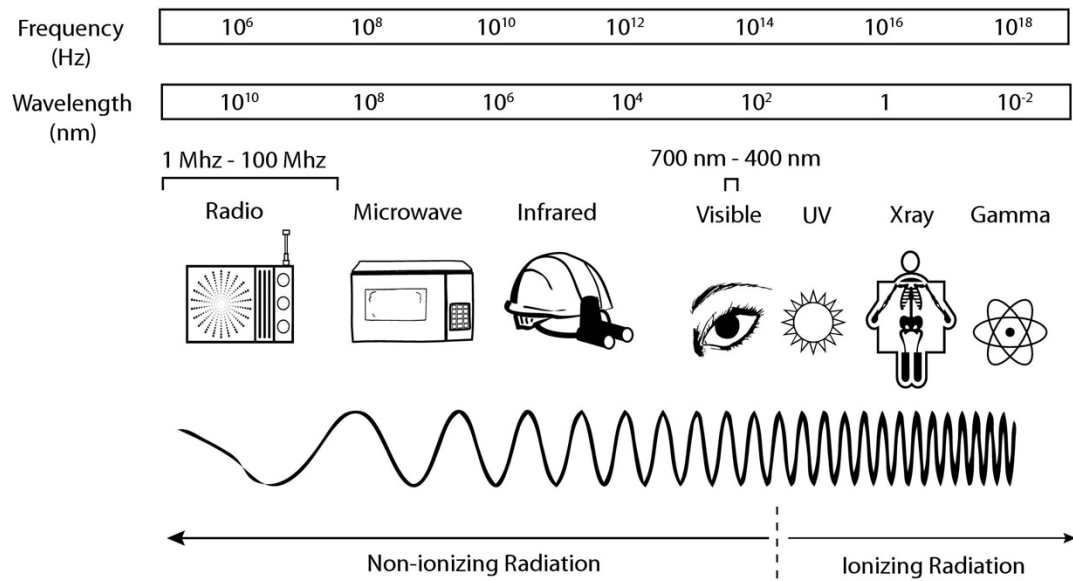


Figure 1.3: Electromagnetic spectrum. Depiction of non-ionizing (lower frequency/higher wavelength) and ionizing (lower frequency/higher wavelength) types of radiation. Ionizing RT are used for imaging and therapy because they carry more energy used to penetrate tissues.

Figure reprinted with permission from publisher. *Tonnessen BH, Pounds L. Radiation physics.*[35]

Clinical LINACs typically operate at an energy range from 10 kVp to 50 MV, and the beam results from deceleration of electrons within metallic targets. The kinetic energy of the electrons is transformed into mostly heat in the target (~99%), with a lesser fraction emitted as X-ray photons. These resultant photons are categorized as either bremsstrahlung or characteristic X-rays. Bremsstrahlung X-rays, also known as continuous X-rays, result from Coulomb interactions between the atomic nuclei of the target material and incident particles. This interaction results in a deceleration of the incident particle and partial loss of its kinetic energy (KE). This loss of kinetic energy produces bremsstrahlung photons (radiative loss). The continuous spectrum of these photons is due to the fact that their energy ranges anywhere from zero to the KE of the incident particle. Consequently, the bremsstrahlung spectrum produced depends on the thickness of the target, atomic number (Z) of the target and the energy of the incident photons.[34, 36]

Similarly, characteristic X-rays are derived from Coulombic interactions or photoelectric absorption interactions. These interactions, however, occur between orbiting atomic electrons of the target material and incident particles (in a typical clinical linear accelerator, these are electrons or photons). In this interaction, an energy difference is produced by the ejection of the orbital electron from its shell and filling of this vacancy by another electron from a higher energy level shell or sub-shell. This difference in energy of the two is subsequently emitted from the atom as a characteristic photon (X-ray), or transferred to another surrounding orbital electron, which is also ejected in the form of Auger or Coster-Kronig electrons. The photons discharged through the transitions of electronic shells or sub-shells comprise of discrete energies that are 'characteristic' of precise target atoms in which the transitions occur, hence the name characteristic X-rays.

### **Radiation biology**

Radiobiology denotes the effects of electromagnetic radiation on biological systems through ionization reactions. These effects depend on the quality and quantity of radiation, as well as the biological system affected. Moreover, irradiation of biological systems results in a series of processes previously described as the physical, chemical and biological phases that vary in time and scale.[37] Radiation energy, usually over 10 eV (electron volts) produces ionizations which yield effects that range from cell cycle disturbances and mutations, to DNA damage and cell death. Within cells, radiation interacts with water or DNA to produce direct (DNA is damaged by radiation) or indirect (damaged perpetrated via free radical produced by radiation) effects. Since water accounts for roughly 70% of the total cell mass, there is a higher probability of radiation interacting with water, and less with DNA given the tightly folded double strand structure in the nucleus. When direct DNA damage occurs, the result is usually reproductive cell death in which metabolic function remains intact but the cells are incapable of undergoing mitosis. During indirect damage, the radiation particle has enough energy to cause ejection of an electron from the orbital shell of a nearby atom such as water or gold. In the case of water, the

electron is ejected from the hydrogen atom resulting in dissociation into a hydrogen and hydroxyl-free radical. The free radicals formed through radiolysis of water are highly reactive and capable of causing DNA damage after migration to the nucleus.[37, 38]

Although several measurements pertain to radiation, absorbed dose is the major metric used in radiobiology to assess the potential for biochemical changes. As radiation traverses an absorbing medium, it can pass through the material unaffected or deposit energy that produces interactions along this path. Absorbed dose is the non-stochastic quantity utilized for radiation. With indirectly ionizing radiation, kinetic energy is first imparted to secondary charged particles (KERMA – kinetic energy released per unit mass). These particles can then transfer some of their energy to the medium (as absorbed dose) or lose some in the form of radiative losses (such as bremsstrahlung, annihilation). Absorbed dose is considered biologically effective and was previously measured in units called 'rad' or radiation absorbed dose. The current SI unit is gray (Gy).[36, 37] For reference, 1 Gy (100 cGy) is equivalent to absorption of 1 joule of radiation energy per kilogram of absorbing material, and 1 Gy (100 cGy) is equal to 100 rads.

However, absorbed dose alone is not adequate for defining net biological effectiveness of varying radiation types. Linear energy transfer (LET) measures the energy imparted to the medium as the ionizing particle travels through, and is used to quantify effects of varying radiation modalities on biological systems – Fig. 1.4.[39] Aforementioned, dose is deposited as the ionizing particle deposits energy along the track, however, distinct forms of radiation yield variable numbers of ionizations along the particle's path. From a microdosimetric view, biologic effectiveness is based on the energy deposition pattern defined density or spacing of ionization events.[40] Ionization events in close proximity within a given length result in higher energy deposition and therefore, greater biological effectiveness per unit for the given radiation. This is measured in keV/μm, and depends on the mass and charge of the particle. Consequently, heavier particles yield more ionization events per tract in comparison to photons which generate secondary electrons with negligible mass. For reference, a 250 keV X-ray (photons) has an LET roughly 2.0 keV/μm, compared to an α-particle with an LET range of 100 – 150 keV/μm. Of note,

LET can increase with decreasing particle energy radiation because the number of ionizations increases as the particle slows down.[41]

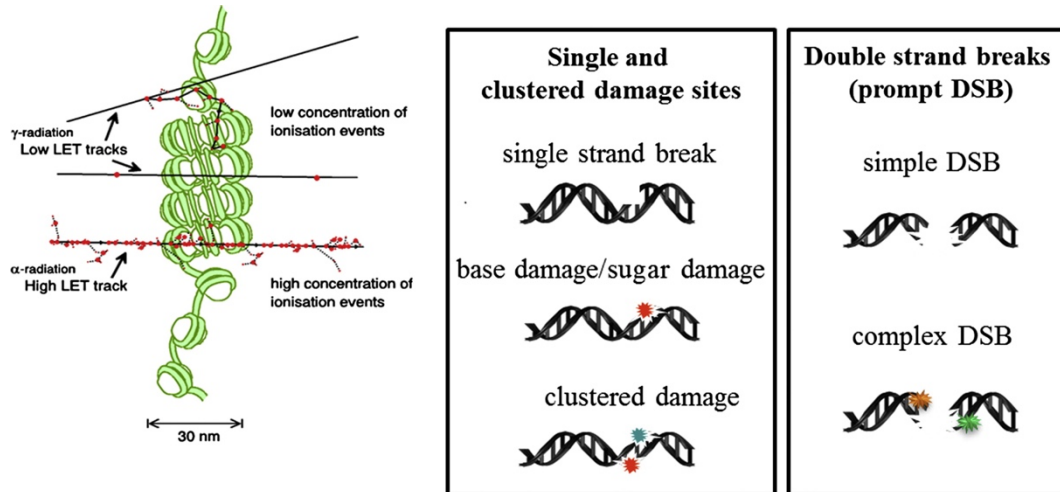


Figure 1.4: DNA damage schematic. Depending on the quality of RT (LET), DNA damage can range from single or clustered sites to simple or complex DSBs. Lower LET. Figure reprinted with permission from publisher. Lomax ME, Folkes LK, O'Neill P. *Biological consequences of radiation-induced DNA damage: relevance to radiotherapy*. [39]

Relative biological effectiveness (RBE) denotes the relative amount of damage to biological tissues by different types of radiation, given a fixed absorbed dose – i.e., amount of ionizations. Per the International Committee on Radiological Protection (ICRP), '[t]he RBE of one radiation compared with another is the inverse ratio of the absorbed dose producing the same effect.' This allows for comparison of different types of radiation with varying LETs producing the same biologic effect. Notably, LET and RBE are linearly correlated. RBE increases with LET up to roughly 100 keV/μm, after which RBE decreases due to the 'over-kill effect'. [37] This endpoint is generally as radiobiologic cell death in which the cell loses reproductive ability – also known as a 'reproductive'; or 'clonogenic' death. In this case, the cell remains physically and metabolically active for a time following exposure to radiation, with some cells even undergoing a few cycles of mitosis prior to permanent termination of vital functions.



Historically, the cell death endpoint is determined using an *in vitro* plating method that generates cell survival curves. The fraction of surviving colonies is logarithmically plotted against the corresponding radiation dose. The goal is to utilize radiation to decrease the population of clonogenic cells, thereby achieving tumor control. The linear-quadratic or 'alpha-beta' formula is used to fit the survival data on the premise that radiation-induced lethal lesions in cells results from association of sublesions.  $\alpha$  represents the rate of cell kill via a single-hit and  $\beta$  denotes the rate through a two-hit mechanism. Cell survival curves are illustrations of dose-response curves to assess the response of tissues to RT.

Clinical radiobiology explores the correlation between physical absorbed dose and the consequential biological response. As such, any benefit adapting the treatment strategy to improve the effects on tumors must be balanced with the consideration of the effect in normal tissues. First analyzed by Holthusen in 1936, dose-response curves are generated for comparison between tumor and normal tissues to generate a therapeutic index.[37, 42] The therapeutic index is defined as the tumour response given a defined amount of normal tissue damage. Subsequently, the therapeutic window defines the potential difference between tumour response and the tolerated dose as a measure surrogate cost-benefit analysis of the treatment. Radioprotectors and radiosensitizers are compounds that can influence the therapeutic index by shifting either the normal tissue curve to the right (protector) or the tumour curve to the left (sensitizer), allowing for implementation of different and potentially more effective treatment strategies.[43, 44] Nanotechnology can play a role in delivery and enhancement of radiation therapy.

## **1.3 Nanotechnology**

### **Nanomaterials**

With an academic shift away from a big picture collective based on anatomy and physiology to a more molecular viewpoint, the biological sciences can, and have, benefited immensely from the advantages of nanotechnology. The integration of nanoscale principles with biological systems has driven the advancement of expertise to empower biomedical research. Studies on biological mechanisms, pathways and processes are conducted at the nanoscale level with physical and chemical techniques enabling improved imaging and control of the properties of atoms, proteins, and larger molecular structures such as the cell membrane.

Nanoscience involves the study of structures of nanoscale (1-100nm) in at least one physical dimension, while nanotechnology encompasses real world application of these structures. Physicist Richard Feynman first discussed the concepts of nanomaterials in 1959 with his talk 'There's Plenty of Room at the Bottom,' and the term 'nanotechnology' was coined over a decade later by Professor Norio Taniguchi.[45, 46] Compared to molecules and atoms, nanomaterials are substantially larger in size, which allows for distinctive behavior and properties. These features are often superior to those of bulk materials because most atoms on nano-sized objects are on or near the surface resulting in weaker bonds and more reactive properties.

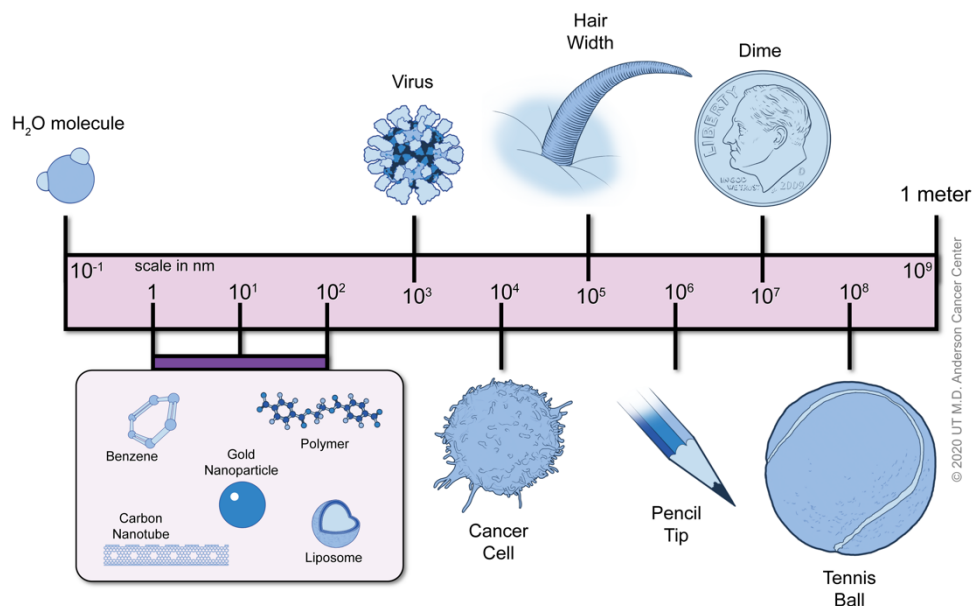


Figure 1.5: Size comparison of nanoparticles. Schematic of scale of some common nanomaterials relative to a water molecule, organic compounds (virus), cells, hair follicle and normal household items.

The two major factors contributing are surface effects and quantum effects which are favorable for dense loading of ligands to these structures.[47] The enhanced surface phenomena result from the high surface area to volume ratio due to the size of nanomaterials. Furthermore, the quantum effects or discontinuity in behavior is caused by the confined delocalization of electrons on the surface of the nanomaterials also imparted by the small size of these particles. Together, these features allow for physiochemical properties unique to these particles, such as surface functionalization of various moieties in order to bestow features permitting multiple purposes simultaneously. Examples of these applications in biotechnology include, but are not limited to, targeting receptors gene regulation, imaging and treatment.[48-55] Our ability to control synthesis and functionalization of materials at the nanoscale allows for tailored design and applications of nanotechnology in interdisciplinary research areas.

Nanoparticles are typically classified into 2 types: naturally occurring or anthropogenic nanoparticles.[56] Natural nanoparticles are ubiquitous and formed through organic physical, chemical and biological processes such as hydrolysis, weathering, erosion, photochemical reactions and many more. These types of nanoparticles include geogenic fullerenes, iron-oxides, sea salt, some metals (such as silver and gold), magnetite and many more. Anthropogenic nanoparticles are purposely manufactured to serve particular purposes and include metallic nanoparticles, carbon nanotubes (CNTs), polymeric nanoparticles and many more. Although there exists a myriad of fabrication techniques, these typically fall into two major categories: top-down or bottom-up approaches.[57-59] On one hand, the top-down approach involves manipulation of a bulk sample to removal material and form a nanoscale structure. (ref) On the other hand, a bottom-up technique entails construction of nanostructures from atomic or molecular foundations. Moreover, both can methods are employed to design NPs with specific properties for intended use.

Driven by innovations in chemistry and synthesis techniques, nanomaterials are fabricated with varying properties that allow for construction of a vast mixture of nanoparticle characteristics. These include: physical properties (size, geometry, hydrodynamic size, porosity); surface properties (functionalization, hydrophilic/hydrophobicity, charge, density); targeting moieties (proteins, aptamers, targeting antibodies); and chemical composition (superparamagnetic oxide nanoparticles, quantum dots, nanocages, carbon nanotubes).[60-62] The increasing variety in the properties of each class of nanoparticles results is distinct *in vitro* and *in vivo* profiles such as stability, toxicity, drug release kinetics, blood clearance, intracellular localization and tissue accumulation. Furthermore, the capability to manipulate material properties at the nanoscale level sets the foundation for the development of innovative diagnostic and imaging agents for disease detection, as well as treatment.

## **Nanoparticle-based medical applications**

Drug delivery is widely studied in the field of nanomedicine, leading with the highest number of commercialized products, publications and patents.[63] Diagnostically, nanoparticles allow for detection at the molecular level, and therapeutically, they enable targeted delivery and controlled release of agents. With an ever-increasing research impetus for the application of nanotechnology in medicine, nanoparticles are under investigation for use in the diagnosis and treatment of illnesses such as malignancies, inflammatory and cardiovascular diseases.[64, 65] Therefore, objectives such as safety, sustainability and tissue-targeted delivery of therapeutics and contrast agents are further studied to create more effective therapies.

Key objectives of delivery systems include release of therapeutics at the desired dose, for a specified duration, and to the desired anatomic location. These objectives apply in the setting any administration route, be it systemic, transdermal, oral, parenteral or pulmonary. Any material recognized as foreign entering the bloodstream is absorbed by phagocytes with the capability to remove them. However, phagocytes do not specifically absorb objects roughly 200nm or less, which allows nanoparticles to travel freely throughout the body.[66] The small size of nanoparticles further increases their mobility by allowing for easier diffusion than solid particles. Drug delivery has evolved drastically since initial accounts of sustained drug release procedures in the 1970's.[67] The field now includes new classes of delivery methods including environmental (pH, temperature, osmosis), diffusion controlled, ligand or chemically controlled conditions.[60, 65, 67-70]

Diagnostically, properties of elements such as iodine and barium with a high atomic number (Z) have historically been used as contrast agents for imaging. These imaging techniques utilize the high X-ray attenuation coefficients of these materials to produce improved contrast.[71] The higher energy absorption coefficients, relative to surrounding tissue, allows the presence of these materials to result in increased dose delivery to surrounding tissue; thereby expanding the potential for the use of high-elements as contrast agents in a therapeutic setting.

Metallic nanoparticles, specifically, have diverse applications in medicine, catalysis, engineering, and several fields. This diversity is largely conferred by their optical, fluorescent, electronic and magnetic properties. The variety of applications stem from two qualities: 1) surface plasmon excitation that allows for examination of their distinct optical characteristics across the vis-NIR band, and 2) surface modification to improve *in vitro* and *in vivo* properties.[72] Gold nanoparticles are one of the most popular class of nanomaterials used in biomedical applications.

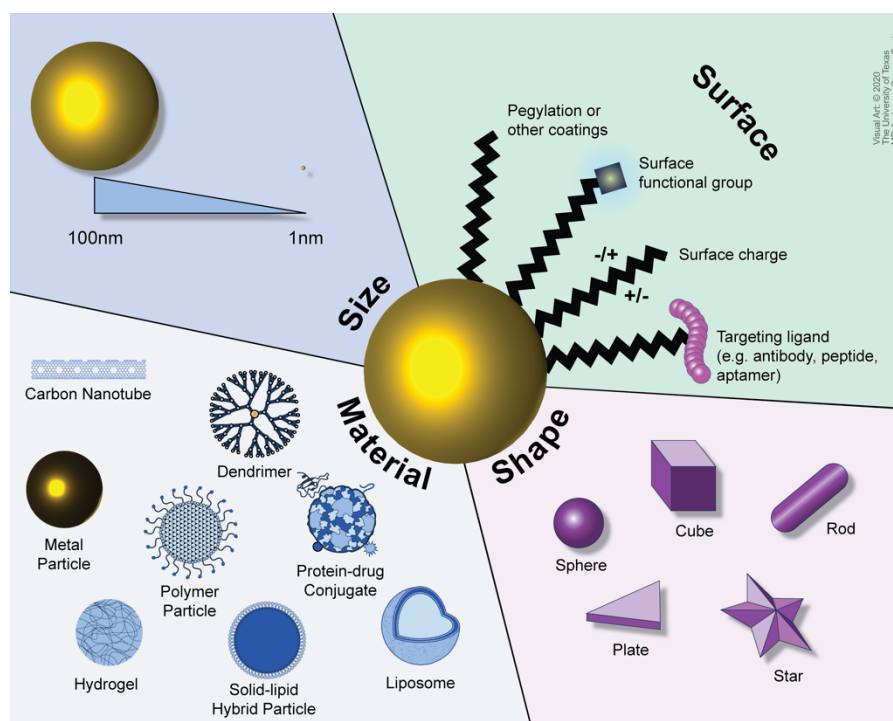


Figure 1.6: Design considerations for nanoparticle synthesis. Final nanoparticle construct depends on the intended use. Properties such as type of material, size, shape and surface functionalization can be tailored to optimize the function envisioned.

## Gold nanoparticles

Due to their unique chemical, optical, electronic and magnetic properties, gold nanoparticles have wide applications in the field of bionanotechnology. Dating back to the 5<sup>th</sup> century, B.C., gold nanoparticles (AuNPs) were used for decorations of ceramics and as ingredients in medicinal concoctions.[73] It wasn't until 1857 that Michael Faraday first recognized that the optical properties observed in structures containing the nanoparticles were due to the differences in the size of particles; a difference which resulted in the variety of colours used for decoration of the ceramics and glass.[74] Several contributions from Zsigmondy, Svedberg, Langevin and many others illuminated concepts of synthesis, ultracentrifugation and continuous Brownian motion that led to better understanding and implementation of AuNPs in science and medicine. Biomedical applications of AuNPs range from imaging, diagnostics, targeted delivery and therapy.

As a high Z element, GNPs have high X-ray attenuation coefficients that lead to improved contrast. Additionally, the high energy absorption coefficients allow for increased dose deposition when present in the irradiated medium. The interest in this application of AuNPs has increased with over thousands of articles published to date. Early work by Hainfeld demonstrated AuNP radiosensitization potential through uptake and tumor control with the combination treatment of AuNPs with kilovoltage RT.[75] This resulted in theoretical and experimental studies to further explore the radiosensitizing effects of AuNPs. The general consensus is that AuNPs sensitize to ionizing radiation in both the *in vitro* and *in vivo* settings. This has been established for RT types ranging from electrons, photons (keV and MV), to charged particles, which further supports the broad clinical applicability of AuNPs.[76] However, macroscopic dose model predictions for the level of radiosensitization effects of AuNPs underestimate the effects observed experimentally, thereby hampering optimization.

AuNPs studies utilize varying formulations in size, shape and surface moieties which have all demonstrated noteworthy effects on sensitization. Moreover, AuNP-mediated radiosensitization is also dependent on the system studied, with varying responses among cell lines, as well as *in vivo* model systems. Altogether, these uncertainties hinder the expansion of AuNPs into clinical

practice with key issues of particle development for optimal targeting, cost effective delivery and validation mechanisms. The ideal AuNP design considers the type of disease and its microenvironment, the biodistribution of the AuNPs *in vivo*, and the interaction with off-target tissues.

In that regard, AuNPs afford a rigid, well-defined foundation for surface modification with different moieties or targeting ligands. The synthesis of monodisperse AuNPs with varying sizes and shapes is relatively straightforward.[77] UV-Vis spectrometry can easily detect the strong surface plasmon peak, and dynamic light scattering can characterize the hydrodynamic size and surface charge using Mie scattering. The optical properties of AuNPs also allows for designing formulations of nanoparticles that can be tracked overtime for stability, and within *in vivo* systems. Thorough characterization of the physiochemical properties, pharmacokinetics, biodistribution and molecular mechanisms are required to set the foundation for future integration into clinical practice.



## 1.4 Thesis overview: hypothesis, objectives and structure

Despite recent advances in research, cancer remains the leading cause of morbidity and mortality worldwide. Radiation therapy (RT), alone and in combination with other therapies, affords a wide range of therapeutic options, with over half of all patients receiving RT at some point in their treatment. The therapeutic efficiency of RT, however, is mainly limited by toxicity and increasing resistance of cancer cells. Consequently, the study of radiosensitizers has emerged as a promising field to address these issues. Among these studies, the field of nanotechnology plays a key role in both the therapeutic approach and as platforms for drug delivery. Gold nanoparticles (AuNPs), in particular, have attracted increasing research interest for the physical and chemical properties that lend these particles very well for use as radiosensitizers.

This thesis enterprise addresses a clinically pertinent need in cancer therapy for tumor-localized radiation dose enhancement. The approach includes deep penetration of on-demand triggered-release of nuclear-targeted gold nanoparticle formulations that strongly sensitize tumors to radiotherapy. This would lay the foundation for a physically, biologically and pre-clinically characterized radiation response modulation strategy with the potential to be widely applied as a turnkey class solution across multiple tumor types. The central hypothesis is that AuNPs packaged in thermosensitive liposomes (TSLs) accumulate passively in the perivascular space of tumors, and hyperthermia facilitates release of the gold nanoparticles deep into the tumor parenchyma; and that cellular internalization, especially nuclear targeting, significantly improves the efficacy of AuNP-mediated radiosensitization by directly modulating tumor radiation response as a result of increased DNA damage from radiation therapy. I test this hypothesis in the following chapters.

Chapters 2 – 4 explore the critical unanswered questions relating to the fate of gold nanoparticles at the cellular level and consequent biological effects, as well as penetration of the biophysical barriers of pancreatic cancer tumor models by the TSLs. The overall experimental design is displayed in Figure x below. Chapter 2 reports the development of gold nanoparticles and the sub-cellular localization of the conjugate nanoparticles. Chapter 3 examines the *in vitro*

radiosensitization capability of the gold nanoparticles and postulated mechanisms of local dose enhancement. Chapter 4 ascertains the *in vivo* accumulation of the gold nanoparticle conjugates with and without thermosensitive liposomes, and the tumor killing efficacy. Chapter 5 provides a summary, discussion and potential future directions. The general design of this thesis is depicted in Fig. 1.7.

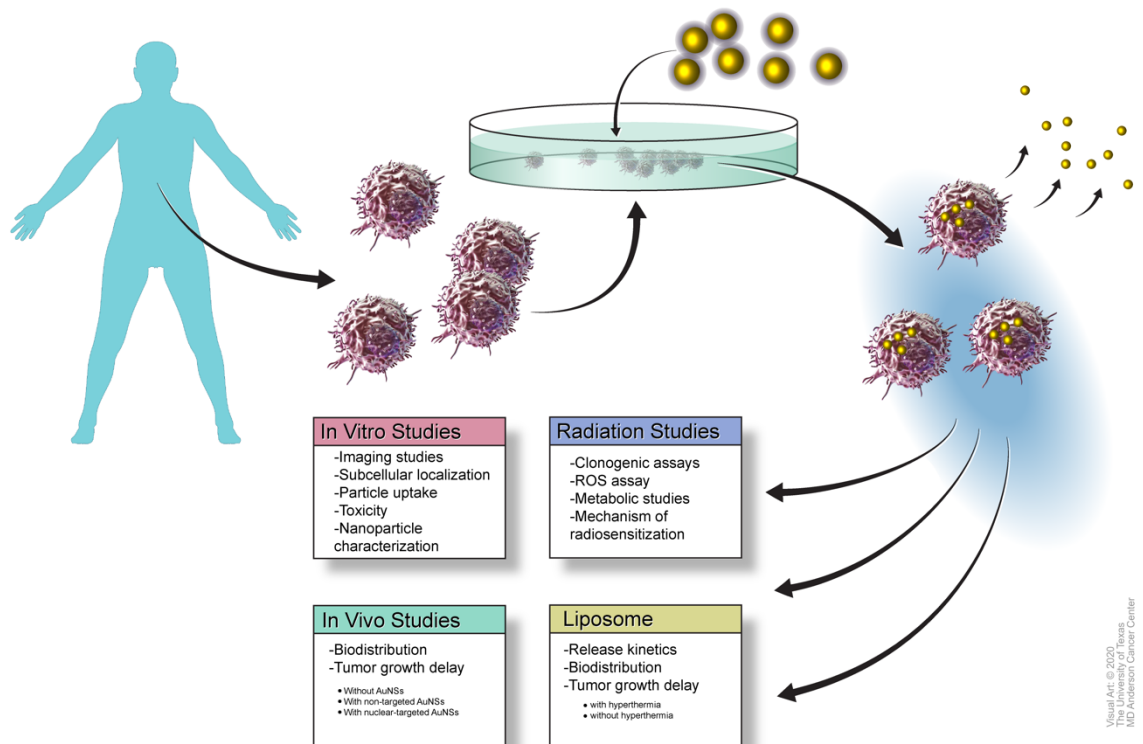


Figure 1.7: Graphical thesis overview. Deidentified human pancreatic tumour cells are used for evaluation for gold nanoparticle radiosensitization *in vitro*, as well as to establish *in vivo* tumours to assess their efficacy in combined treatment.

## Chapter II: Cellular nanoparticle distribution

### 2.1 Abstract

With increasing clinical interest in nanoparticles as drug delivery (clinical trials) or treatment enhancement agents for cancer, mechanistic investigations of the physiochemical properties can result in improved delivery strategies. In the context of radiation in which the main target is DNA, it follows that targeting of nanoparticles to the nucleus can produce a pronounced effect in terms of enhancing the effects of radiation. Here, we investigate the feasibility of designing and fabricating gold nanoparticles capable of transport into the cell nucleus (Figure 2.1). We consider various strategies including nanoparticle parameters such as size and charge, targeting moieties, conjugation chemistries, nanoparticle treatment time and cellular confluence at the time of treatment. Panc-1 (pancreatic cancer cell line) is used as an original model and these experiments are further validated in a second pancreatic cancer cell line (MiaPaCa-2), as well as a normal pancreas cell line (HPDE). Final nanoparticle design consists of spherical gold nanoparticles 4 to 5 nm in diameter of the core, with a final hydrodynamic size  $< 15\text{nm}$  as measured by dynamic light scattering, and surface charge  $< +5\text{mV}$  as determined by zeta potential. Optical density as measured by spectrophotometry serves as an initial surrogate marker prior to further characterization. Imaging data using dark field microscopy, confocal microscopy and transmission electron microscopy captures the cellular level distribution. Inductively coupled plasma mass spectrometry quantitates the uptake of the nanoparticles. Cellular fractionation and subsequent quantification of gold uptake further confirm sub-cellular localization of the nanoparticles.

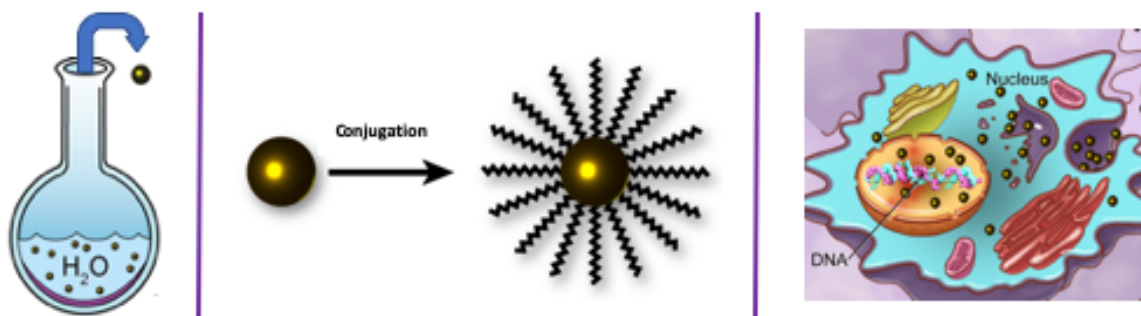


Figure 2.1. Chapter II graphical overview. Synthesis, conjugation and characterization of AuNS. Assessment of AuNS sub-cellular localization.

## 2.2 Introduction

Recent advances in the design of nanoparticles (NPs) has resulted in a broader number of applications for imaging, drug delivery and therapeutics. [78-80] For gold nanoparticles (AuNPs), these applications rely on the shape, size and surface functionality of the nanoparticles. Furthermore, these characteristics are greatly partial to the physiochemical conditions at the time of NP synthesis, such as reaction temperature, gold to reducing agent ratio, presence of surfactants and stirring rate.[81] Moreover, effectual use of these particles necessitates overcoming biological barriers, accumulation in specific tissues and subcellular compartments, and prolonged circulation.[82, 83] As such, the properties of AuNPs commonly evaluated include size, shape, interaction with light (usually via optical density measurements), surface charge and surface chemistry or functionalization status.

Due to their notable scattering cross section ( $\sim 10^{-10} \text{ cm}^2$ ), metal particles can be imaged under white-light illumination. The oscillating electromagnetic field of the light induces an oscillation of free electrons in the metal NP with light exposure. The electron oscillation at the particle surface results in a charge difference in the ionic lattice. This tnhe causes a dipole oscillation in the direction of the electric field of the light. The specific frequency at which this oscillation is at the maximum is known as the surface plasmon resonance (SPR).[84-86] The

SPR results in a strong absorption of incident light measurable by UV-Vis (ultraviolet-visible) spectrometry. Another optical property of metal NP is the total light extinction. This is the loss of electromagnetic wave energy after passing through matter, and results from absorption and scattering processes. Absorption occurs when the energy is dispersed due to inelastic mechanisms. Scattering happens when the energy causes electrons in the matter to oscillate and emit photons at the same frequency as incident light (Rayleigh scattering) or at a shifted frequency (Raman scattering). The SPR, total extinction and scattering are commonly studied using Mie theory.[87] As alluded to, the SPR for metal particles, AuNPs in our case, can be tuned across the visible spectrum and near infrared by simply altering the particle size and shape.[88, 89] As such, the interaction of AuNPs with light provides an accurate technique to evaluate and track other properties such as size, shape and functionalization status.

Given that the main target of RT is cell DNA, we hypothesized that targeting the gold nanoparticles to the nucleus with localization close to the DNA would result in an increased incidence of DNA damage upon radiation. Therefore, we design 4-5nm gold nanospheres (AuNSs) here to explore the mechanistic aspects of targeting them to the nucleus *in vitro*. In particular, we examined the change in AuNS properties such absorbance, size (using dynamic light scattering – DLS) and charge as we conjugated targeting moieties to the surface. In order to achieve subcellular localization, the targeted AuNSs need to traverse the cellular membrane and nuclear membrane, for the targeted particles. We underscore the utility of a nuclear localization sequence (NLS) molecule at the surface of the AuNSs on subcellular targeting to the cell nucleus.

## 2.3 Results and discussion

Therapeutic applications of nanoparticles in cancer require either localization to the tumor microenvironment or cellular internalization for *in vitro* studies to minimize effects from the presence of particle in culture media. Here, we design experiments to evaluate the uptake of gold nanoparticles within cells, and specifically, into the cell nucleus for the group conjugated with the NLS.

### Synthesis and characterization of AuNS conjugates

We synthesize 4-5nm gold nanospheres (AuNSs) as base particles for further modification. The bare AuNSs are then conjugation with poly(ethylene) glycol (PEGylated) to yield control particles (pAuNS), and further decorated with one of two peptide sequences to generate either a second control particle group with a scrambled peptide sequence similar in size and molecular weight to the NLS but consisting of different amino acids (sAuNS), or nuclear-targeted nanoparticles (nAuNS) with an NLS. The conjugation schema is illustrated in Figure 1. AuNS formation is confirmed using transmission electron microscopy (TEM) images revealing monodisperse particles uniform in size (Figure 2.2). Notably, the PEGylated and further conjugate groups of the AuNSs appear identical to bare AuNS on TEM imaging. Quantification using the microBCA assay estimated 950-1000 peptides per gold nanoparticle.

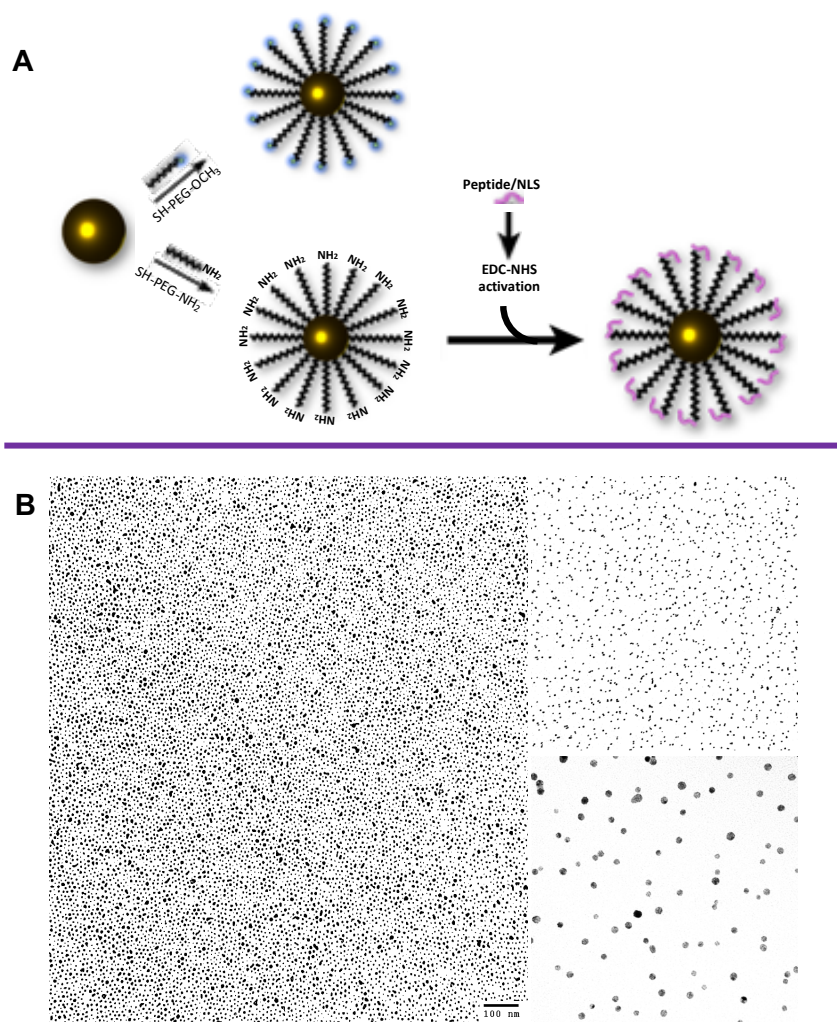


Figure 2.2. AuNS synthesis and characterisation. (A) Schematic of AuNS conjugation with mPEG to create pAuNSs (top); bifunctional PEG (bottom) followed by coupling by the EDC/NHS reaction to create sAuNSs or nAuNSs. (B) TEM images of synthesized AuNSs demonstrating uniform and monodisperse particles. Scale bars 20nm and 100nm.

Due to their optical properties, AuNP stability is easily assessed using the surface plasmon resonance (SPR) band. The colour of the AuNS solution during synthesis is dependent on the SPR, and can be an immediate indicator for particle size or aggregation prior to further PEGylation. Ultraviolet-visible (UV-Vis) spectra confirm a peak absorption band (SPR) for the bare AuNS (513 nm) in MilliQ water that resulted in slight red shifts upon PEGylation (pAuNS) at 514 nm and subsequently, a nuclear localization sequence (nAuNS) or a scrambled peptide sequence (sAuNS) – 516 nm for both. These absorbance peaks remained stable with additional synthesis and conjugation cycles as represented by the consistent standard deviation in measurements (Figure 2.3 and Table 2.1).

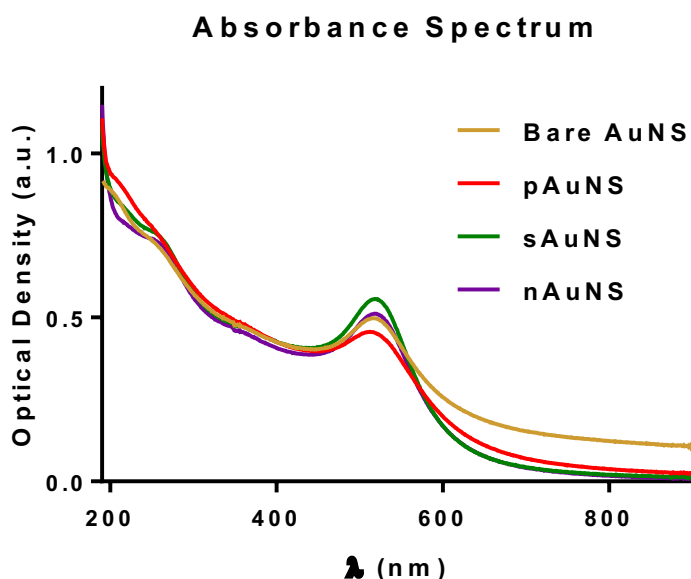


Figure 2.3: Spectrophotometric analysis of AuNS. UV-Vis spectra of AuNSs. There is a slight red shift in peak absorbance observed from bare AuNS as the particle is PEGylated, then conjugated with a peptide sequence.



Table 2.1: AuNS characterization

AuNS Formulation	Peak Absorbance	Size	Zeta Potential
Bare AuNS	513 ± 3nm	5.28 ± 1.5nm	-14.7 ± 6.4mV
pAuNS	514 ± 3nm	11.56 ± 3.9nm	-3.54 ± 7.1mV
sAuNS	516 ± 3nm	13.95 ± 2.7nm	0.013 ± 6.1mV
nAuNS	516 ± 3nm	14.34 ± 3.1nm	2.81 ± 10mV

Peak absorbance on UV-vis spectroscopy, hydrodynamic diameter (size) on dynamic light scattering and surface charge (zeta potential) on zeta potentiometry of different AuNS formulations presented as mean ± standard deviation.

In addition to UV-Vis spectroscopy, dynamic light scattering (DLS) and Zeta-potential measurements confirm electrokinetic properties of the AuNS conjugates. PEGylation generally leads to an increase in hydrodynamic size by roughly 10 – 30 nm. Size measurements calculated per DLS verify an increase in hydrodynamic diameter with PEGylation and subsequent conjugation with either peptides used. The resultant particles suspended in water exhibit near-neutral surface charge (ranging from -3.54 to +2.93 mV zeta potentials). In fact, measurements of absorbance and size reveal stable conjugates up to one-month post-synthesis, whereas zeta potential measurements started trending upwards around three weeks post-synthesis (Figures 2.4 – 2.5, and Tables 2.2 – 2.4).

Table 2.2: Stability of AuNS formulations per UV-Vis spectra

AuNS Formulation	Day of Synthesis	Day 3 Post-Synthesis	Day 7 (Week 1)	Week 2	Week 3	Week 4
Bare AuNS	513 ± 3nm	513 ± 3nm	512 ± 3nm	513 ± 3nm	514 ± 3nm	513 ± 3nm
pAuNS	514 ± 3nm	514 ± 3nm	514 ± 3nm	514 ± 3nm	514 ± 3nm	514 ± 3nm
sAuNS	516 ± 3nm	516 ± 3nm	516 ± 3nm	516 ± 3nm	516 ± 3nm	516 ± 3nm
nAuNS	516 ± 3nm	516 ± 3nm	516 ± 3nm	516 ± 3nm	516 ± 3nm	516 ± 3nm

Stability of AuNS formulations over time as determined by UV-vis absorbance spectroscopy. AuNS formulations were stored at 4°C and peak absorbance was measured at different time points up to 4 weeks from synthesis. Values are mean ± standard deviation.

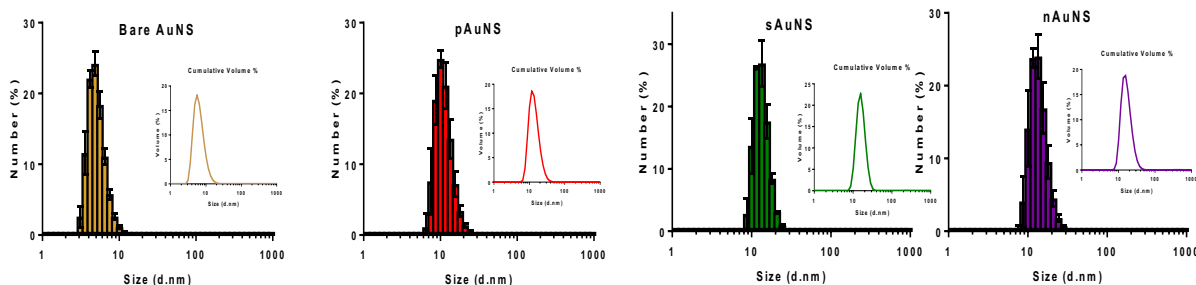


Figure 2.4: Size evaluation of AuNSs. Representative dynamic light scattering measurements of AuNS formulations confirming progressive increase in size as bare AuNSs are decorated with PEG and then the peptide sequence.

Table 2.3: Size stability of AuNS formulations per DLS measurements.

AuNS Formulation	Day of Synthesis	Day 3 Post-Synthesis	Day 7 (Week 1)	Week 2	Week 3	Week 4
Bare AuNS	5.28 ± 1.5nm	5.7 ± 2.3nm	5.2 ± 2.4nm	5.9 ± 1.9nm	6.7 ± 2.0nm	9.87 ± 2.9nm
pAuNS	11.56 ± 3.9nm	11.4 ± 2.4nm	11.91 ± 3.1nm	11.46 ± 2.9nm	11.82 ± 2.6nm	11.57 ± 2.7nm
sAuNS	13.95 ± 2.7nm	13.72 ± 3.5nm	13.79 ± 3.1nm	14.09 ± 4.2nm	14.05 ± 3.3nm	13.87 ± 3.0nm
nAuNS	14.34 ± 3.1nm	14.27 ± 3.4nm	14.29 ± 3.4nm	14.43 ± 3.2nm	14.78 ± 3.7nm	14.57 ± 3.2nm

Stability of AuNS formulations over time as determined by dynamic light scattering. AuNS formulations were stored at 4°C and hydrodynamic diameters were measured at different time points up to 4 weeks from synthesis. Values are mean ± standard deviation.

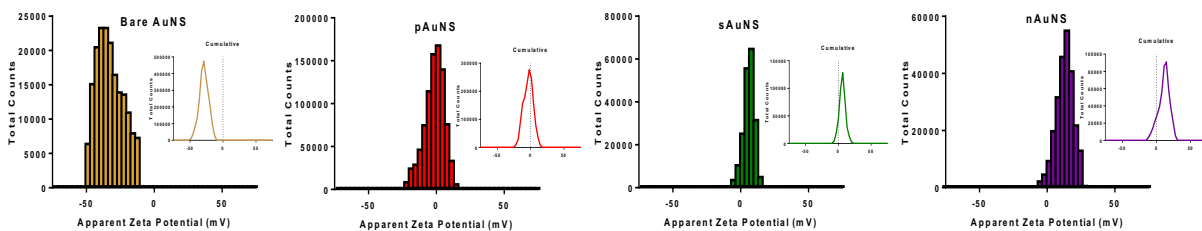


Figure 2.5: Surface charge evaluation of AuNSs. Representative zeta potential measurements of AuNS formulations confirming near neutral surface charge when bare AuNSs are decorated with PEG or the peptide sequence.

Table 2.4: Surface charge stability of AuNS formulations per zeta potential measurements.

AuNS Formulation	Day of Synthesis	Day 3 Post-Synthesis	Day 7 (Week 1)	Week 2	Week 3	Week 4
Bare AuNS	-14.7 ± 6.4mV	-17.7 ± 13mV	-13.1 ± 9.3mV	-18.9 ± 5.1mV	-28.6 ± 7.1mV	-29.3 ± 8.9mV
pAuNS	-3.54 ± 7.1mV	-2.91 ± 10mV	-3.01 ± 11mV	-1.49 ± 12mV	-0.29 ± 10mV	1.25 ± 8.0mV
sAuNS	0.013 ± 6.1mV	0.98 ± 4.0mV	1.16 ± 7.3mV	0.013 ± 6.1mV	6.23 ± 4.8mV	4.53 ± 4.2mV
nAuNS	2.81 ± 10mV	1.14 ± 3.3mV	2.81 ± 10mV	2.93 ± 9.0mV	10.6 ± 6.1mV	11.0 ± 8.1mV

Stability of AuNS formulations over time as determined by zeta potentiometry. AuNS formulations were stored at 4°C and surface charge was measured at different time points up to 4 weeks from synthesis. Values are mean ± standard deviation.

The SPR band intensity and wavelength is stronger for noble metals, especially gold, and dependent on factors affecting electron charge density at particle surface.[90, 91] These factors include particle size, shape, composition and the surrounding medium dielectric constant. Any variations in the SPR band are indicative of particle stability such that any changes in color of the solution, or SPR band position and shape denote particle aggregation or size and shape variations. As such, the consistency in solution color and absorbance peaks signify reliability in the synthesis and conjugation techniques for every preparation as well as the stability of these particles prior to experimental use, as evidenced in this chapter.

### **AuNS cellular toxicity and uptake**

The cell membrane is a phospholipid bilayer that acts as a selectively permeable barrier to control the entry and expulsion of substances in and out the cell.[92, 93] Passive and active transport allow passage of materials through the membrane. Passive transport occurs via diffusion down a concentration gradient whereas active transports requires adenosine triphosphate (ATP) for movement against the concentration gradient. Charged biomolecules are taken up through endocytosis, classified into phagocytocysis and pinocytosis. Pinocytosis, the mechanism of internalization for small particles in the nanometer range, is further classified into clathrin and caveolae-mediated, or clathrin- and caveolae-independent endocytosis.[94] The size, shape, surface charge or functionalization and hydrophilicity or hydrophobicity further affect cellular internalization, route of uptake and cytotoxicity of nanoparticles.

Although gold nanoparticles are biocompatible, surface ligands and charge can affect cell uptake and viability. A previous study established no *in vitro* toxicity of gold nanoparticle concentrations as high as 1.5 nM with minimal effect on cell proliferation over two doubling times.[95] This study also demonstrated that serum-containing media significantly reduced the internalization of AuNPs due to adsorption of the proteins to the AuNP surface, and interruption of cellular membrane-AuNP interactions. Therefore, we test the effect of gold nanosphere

(AuNS) treatment on cells using the colorimetric MTT assay evaluating metabolic activity via the NAD(P)H pathway. Treatment with AuNSs alone showed no effect on cell viability up to 5 days following treatment of Panc-1 and MiaPaCa-2 pancreatic cancer cells on an MTT assay (Figure 2.6a). The treatment concentration of AuNSs for further *in vitro* studies was chosen based on these experiments and preliminary clonogenic assay results.

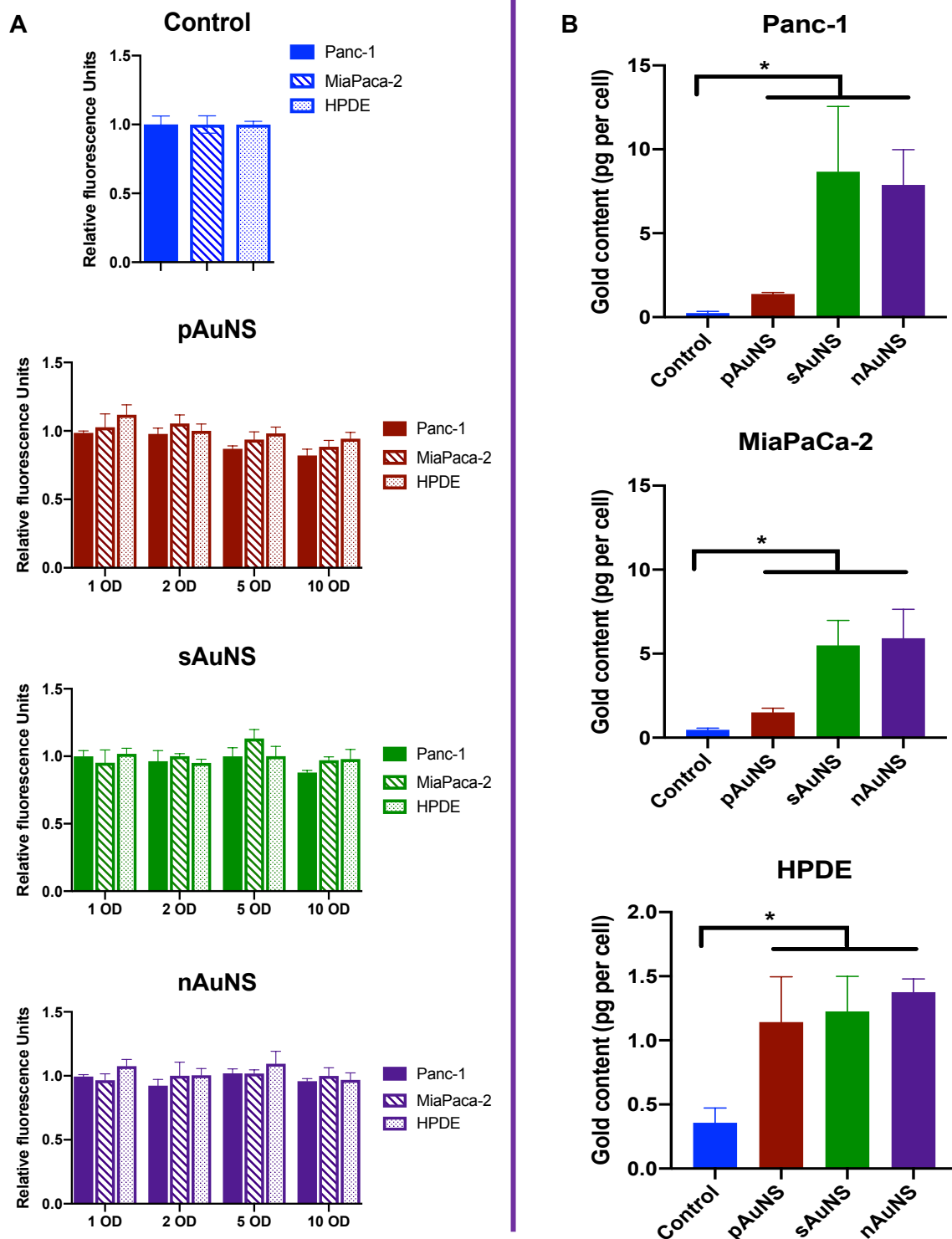


Figure 2.6: AuNS cytotoxicity and uptake. (A) Cellular toxicity studies in Panc-1, MiaPaca-2 and HPDE cells using the MTT assay. Fluorescent intensity measurements are normalized to the values obtained in control (no AuNS-treated) groups. (B) ICP-MS measurement of gold uptake in all three cell lines normalized to the cell count prior to sample preparation for analysis.

While minimizing particle aggregation and protein adsorption, PEGylation also reduces cellular internalization.[95] A 2009 study established a molecular weight of 2 kDa for PEG, based on optimal chain length and surface density saturation, resulted in the least uptake in an *in vitro* macrophage study.[96] As such, this molecular weight of PEG is used for AuNS modifications in all experiments. Additionally, a cell penetrating peptide (CPP), RGD in our case, is employed to facilitate cellular uptake. However, following comparison with no CPP treatment that reveal greater uptake levels without the CPP, subsequent experiments were performed with no CPP treatment. In both cell lines, inductively coupled plasma mass spectrometry (ICP-MS) quantitative elemental analysis of gold noted greater gold uptake following sAuNS and nAuNS treatment than pAuNS treatment ranging from 1 – 15 picograms/cell (Figure 2.6b).

Conjugation of AuNSs with biomolecules that anchor to cell surface receptors is a method used to amplify internalization into cells. As briefly discussed, the major internalization pathway for non-targeted AuNSs is via receptor-mediated endocytosis (RME), evidenced by decreased uptake at low temperatures or ATP-depleted conditions.[97-100] This method of uptake, however, results in entrapment of the particles in intracytoplasmic vesicles followed by degradation or excretion from the cell, which limits the potential applications. Delivery to subcellular sites, such as mitochondria, golgi apparatus or endoplasmic reticulum, could improve drug effect at the intracellular site action and minimize off-target consequences.



## **Sub-cellular localization**

The cell nucleus is an ideal target for drug delivery because it is the central focus of the cell's genetic information. For RT, the nucleus is of particular interest because DNA in cancer cells is the main target for RT damage. In eukaryotic cells, the nucleus is isolated from the cytoplasm by the double-layered nuclear envelope traversed by nuclear pore complexes (NPCs). Specific ligands such as nuclear localization sequences (NLSs) or nuclear export sequences (NESs) are required to transport macromolecules across NPCs.[101, 102] Proteins known as karyopherins facilitate movement in (importins) or out (exportins) of the nucleus through the NPC by binding to the macromolecule and docking it to the respective side of the NPC.[102, 103] Therefore, attachment of macromolecules to NLS drives their accumulation in or around the nucleus.

We utilize an NLS molecule derived from the Human Immunodeficiency Virus (HIV) transactivator of transcription (TAT) peptide for nuclear targeting. We compare subcellular localization of these gold nanoparticles targeted to the nucleus (nAuNS) to no particle treatment (control) and treatment with either pAuNSs or sAuNSs. Qualitative dark field microscopy showed a colocalization of nAuNS signal with a nuclear stain (DAPI) while a generalized cytoplasmic distribution was observed in both Panc-1 and MiaPaCa-2 cells for pAuNS and sAuNS particles. The spatial distribution of gold within cells was qualitatively different with dark field microscopy of both cells showing localization of the nAuNSs in the nucleus (stained with DAPI) while the sAuNSs showed a more generalized cytoplasmic distribution (Figures 2.7 – 2.8).

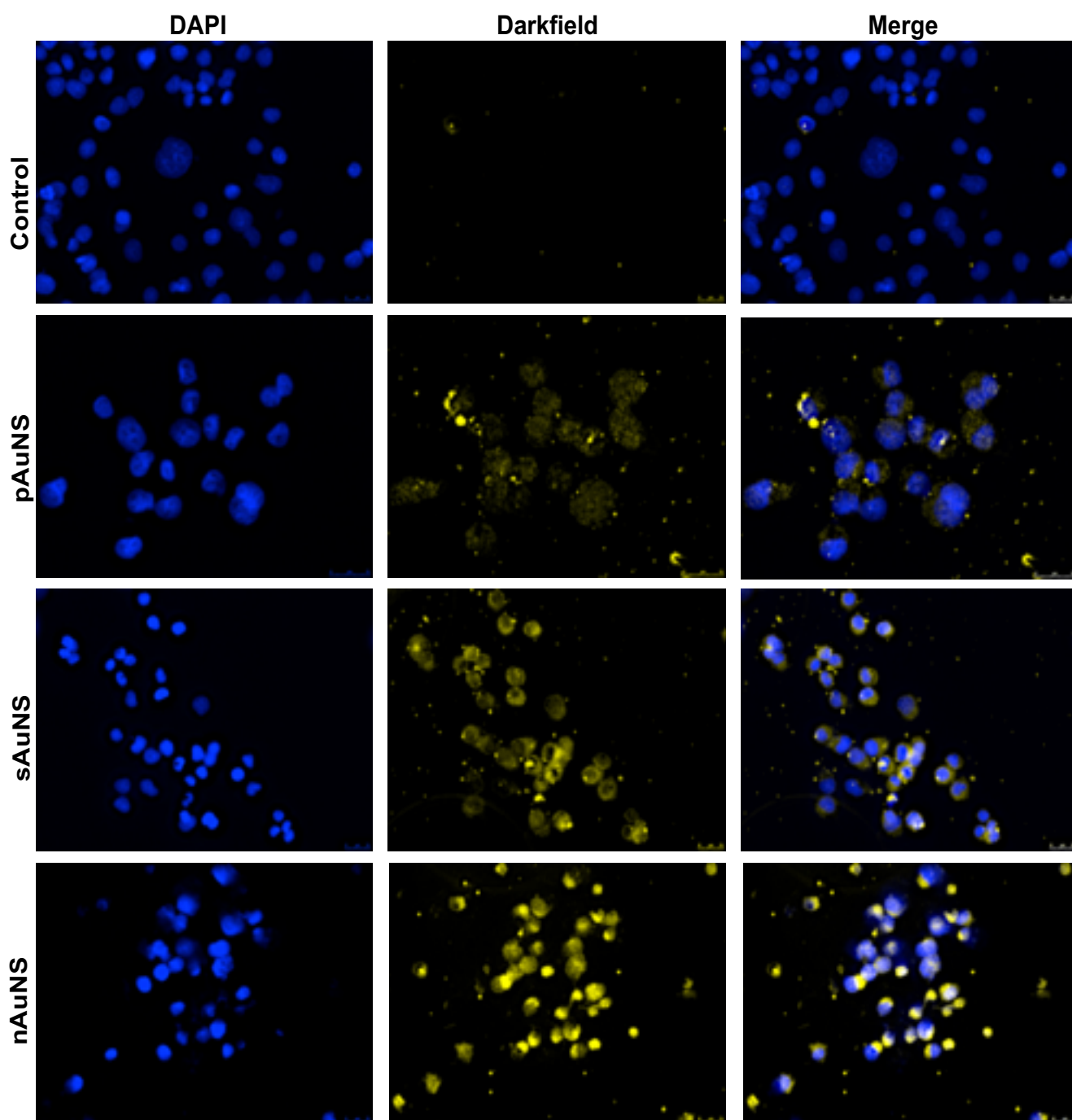


Figure 2.7: MiaPaCa-2 AuNS localisation. Uptake studies qualitatively assessed using dark field microscopy confirmed minimal pAuNS internalization but abundant sAuNS and nAuNS uptake, with greater co-localization of nAuNSs with nuclear DAPI stain than pAuNSs or sAuNSs.

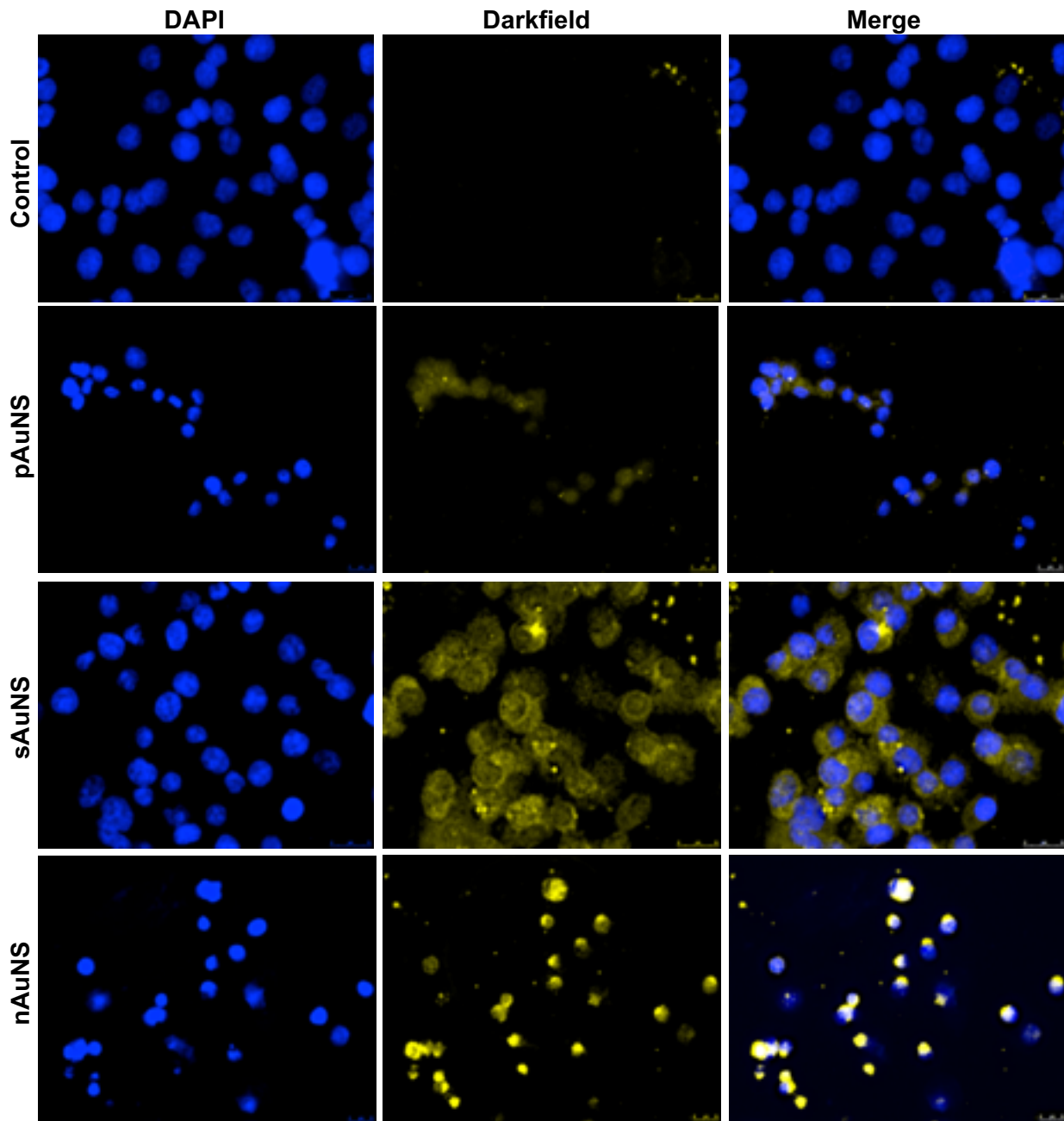


Figure 2.8: Panc-1 AuNS localisation. Similar to MiaPaCa-2 results, Panc-1 dark field studies confirmed minimal pAuNS internalization but abundant sAuNS and nAuNS uptake, with greater co-localization of nAuNSs with nuclear DAPI stain than pAuNSs or sAuNSs.

This dichotomy was further validated when cellular cytoplasmic and nuclear fractions were separated, as confirmed by Western blot, and gold uptake was higher in the nucleus with nAuNSs than pAuNSs or sAuNSs (Figure 2.9). Gold uptake in cell fractions is normalized to protein content, explaining the higher gold levels in the nuclear compared to the fractions. TEM images of Panc-1 and MiaPaCa-2 cells showed greater numbers of nAuNSs outside the endosomes and in the nucleus than pAuNSs and sAuNSs. Representative images are shown in Figures 2.10 – 2.11.

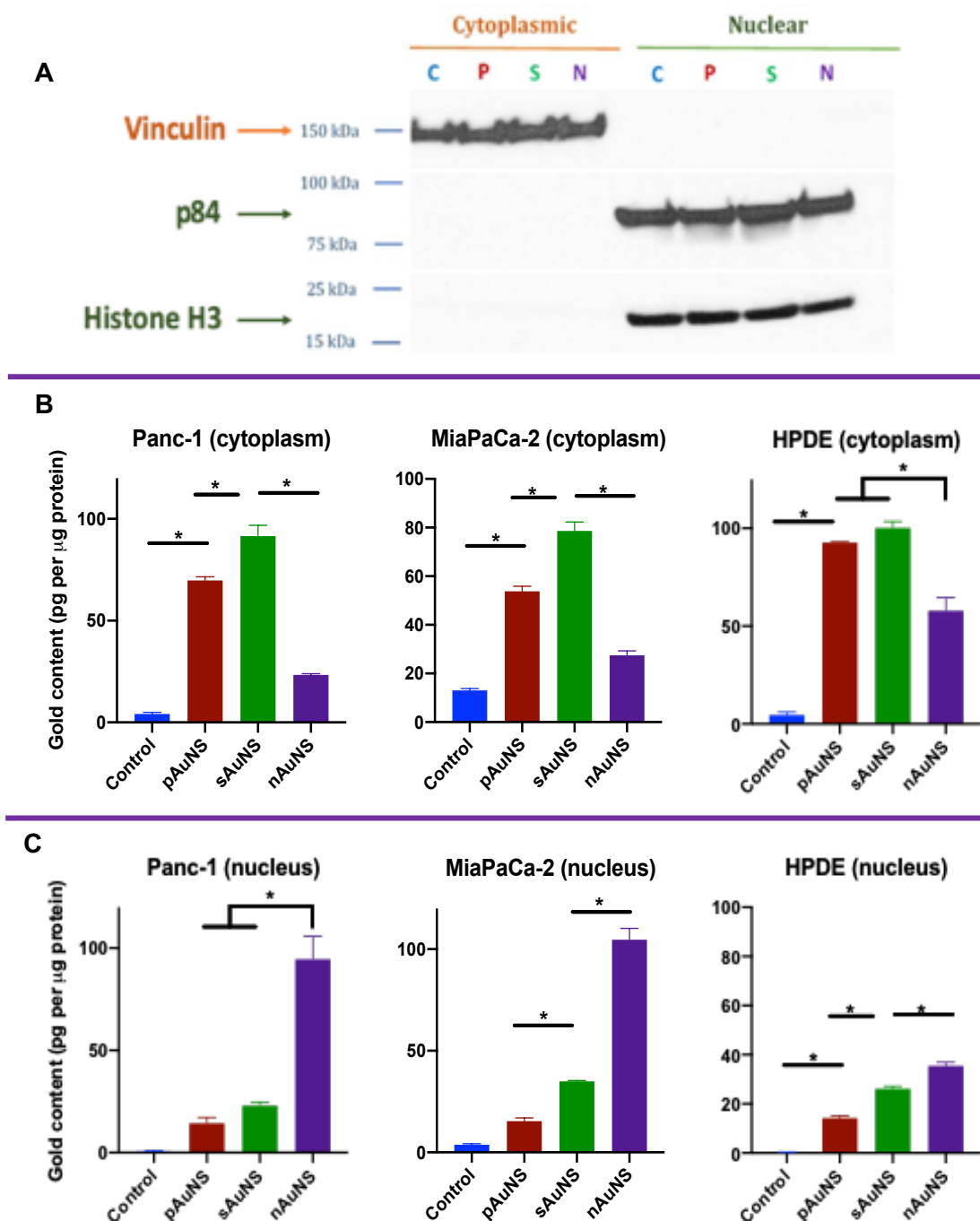


Figure 2.9: Subcellular localization of AuNSs. (A) Western blot confirmation of subcellular fractionation with vinculin denoting cytoplasmic fraction, and p84 and histone H3 indicating nuclear fractions. (B – C) ICP-MS quantification of elemental gold content in cytoplasmic vs. nuclear fractions in all three cell lines normalized to the cell count prior to sample preparation for analysis, or amount of protein per Western blot analysis.

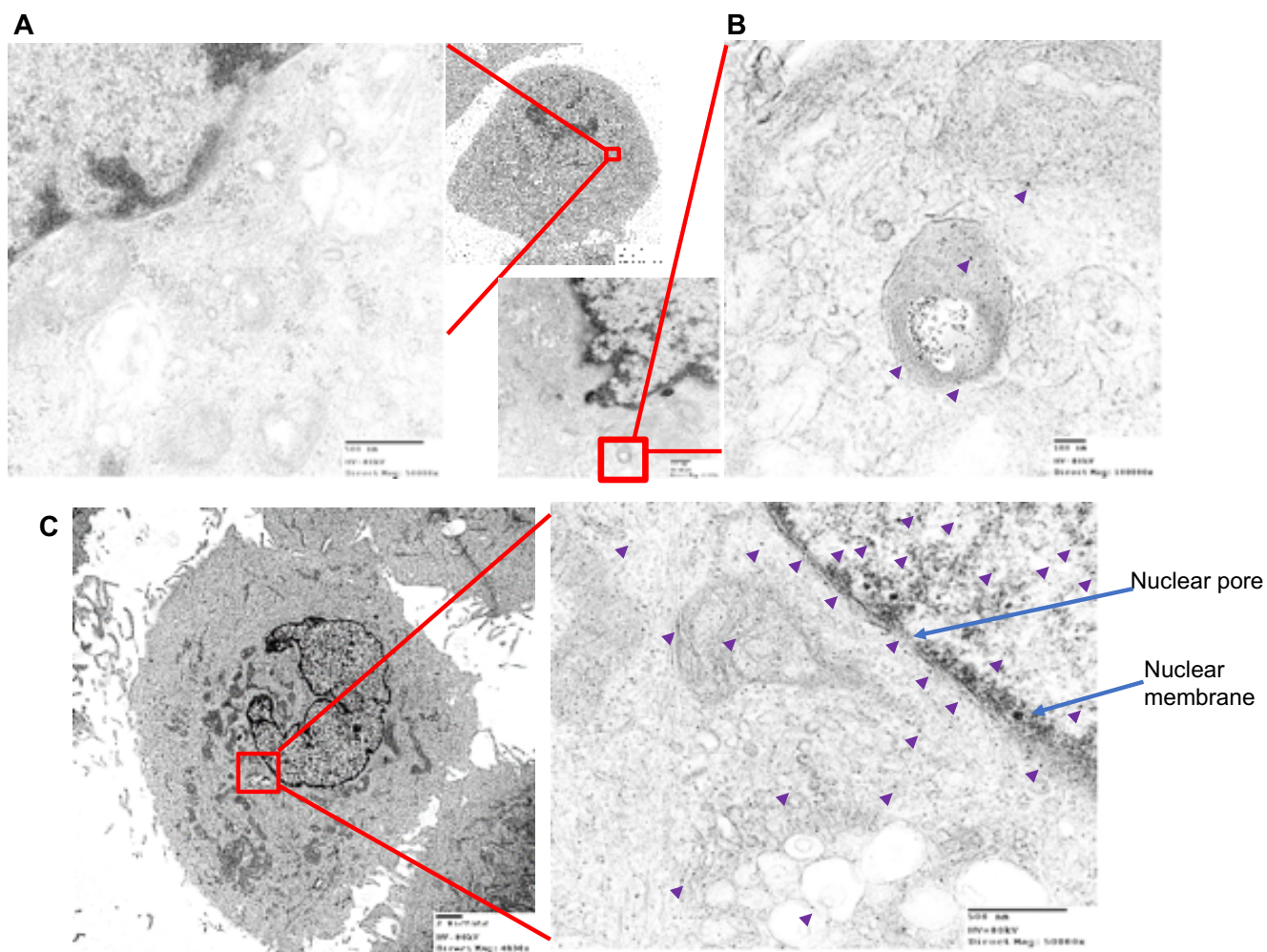


Figure 2.10: Subcellular localization of AuNSs in Panc-1 cells. (A) TEM images of control cells with no particle treatment with a higher magnification close-up image as well. (B) Representative image of non-targeted pAuNSs in cells at low and high magnifications. Purple arrowheads point to AuNSs. (C) TEM images of nAuNS-treated cells with high magnification images of AuNSs near the nuclear membrane. Scale bars noted in each figure.





For cancer, nuclear-targeting is ideal for various therapeutics including chemotherapy because the mechanism of action is through direct interaction with DNA or through inhibition of replication enzymes such as topoisomerase prevent cell proliferation.[104, 105] However, this requires drug transport into the tumor microenvironment, through the cell plasma membrane, and finally the nuclear membrane consisting of pores on the order of nanometers.[106] We demonstrate here that conjugation of a TAT-derived NLS molecule to AuNSs successfully localizes them to the nucleus of pancreatic cancer cells, even to a greater extent than normal HPDE cells. These results support the notion of differential uptake of AuNSs in normal vs cancer cells at the whole cell and subcellular level in terms of the nucleus. Furthermore, this sets the groundwork to test our hypothesis of enhanced radiosensitivity with nuclear-localized AuNSs vs. AuNSs sequestered in the cytoplasm or tumor microenvironment.



## 2.4 Conclusion

Clinical application, drug penetration, intra-tumoral accumulation and systemic toxicity are a few of the various obstacles that plague effective adaptation of nanoparticles for cancer therapy. These factors are heavily influenced by the design of the nanoparticles which determine their fate, behavior and effects in living organisms. The stability of nanoparticles is fundamental for maintenance of physicochemical factors *in vitro* as well as *in vivo*. Optimization of parameters such as size, surface charge, and targeting ligand density is required to achieve effective delivery and subsequent biological response. The main objective of this chapter is to establish the stability, biocompatibility and localization of the conjugate AuNSs for further testing in the following chapters.

Similar to bulk gold, AuNPs normally exhibit low *in vitro* toxicity regardless of size or geometry.[97] Cells internalized concentrations up to 100 nM with no measurable toxicity of AuNPs with negative or neutral capping agents such as citrate, biotin, cysteine or glucose. At concentrations as low as 10 nM, however, AuNPs capped with cetyltrimethylammonium bromide (CTAB) were found toxic to the same cells.[107] CTAB is quaternary ammonium surfactant commonly used to stabilize AuNPs resulting in a cationic surface charge. Although cationic AuNPs induce toxicity to a greater extent than their anionic counterparts, this observation is dependent on the cell line under study.[108, 109] The charge of AuNS particles designed in this aim remained stable following synthesis with a surface charge near neutral, as supported by the zeta potential measurements.

Most bare nanoparticles remain stable in deionized water due to charge repulsion, as is the case for the fabricated bare AuNSs here. Addition of salts and proteins can lead to charge screening and adsorption, shielding surface charge which results in aggregation. This is observed for the bare AuNS once added to cell culture media containing proteins. Poly (ethylene glycol) (PEG) is widely utilized for modification of several compounds for biomedical applications.[110-112] Grafting with PEG renders adjacent nanoparticles less susceptible to aggregation induced by the presence of salts and serum because it forms extended layers that

maintain separation between the particles. Engraftment of PEG to AuNPs is a popular approach to bestow steric stability to AuNPs and the increased circulation *in vivo* through evasion of macrophage recognition as foreign entities. Additionally, *in vivo* applications of AuNPs require dilution in solutions such as phosphate buffered saline (PBS) in which PEGylation prevents salt-induced aggregation. Besides the bare AuNSs in these studies, the resultant particles remain consistent in size, shape and with near neutral charge across various synthesis batches and over weeks at time. This speaks to the robustness of our design protocol and the stability of the final constructs.

Further underscoring stability, the AuNSs remain evenly distributed in phosphate buffered saline (PBS) and cell culture media solutions containing proteins for over 48 hours at room temperature, 4 C and 37 C with no visible signs of aggregation. Cell treatment consists of diluting AuNS solutions with cell culture media to a given concentration (optical density units – OD) prior to the addition to the cells. Consequently, AuNS interaction with cells is based on Brownian motion of the particles in the media over the treatment time period and the surface ligands. Untargeted nanoparticles are mainly internalized via receptor-mediated endocytosis (RME) – also known as clathrin-mediated endocytosis, and very rarely through passive diffusion for slightly cationic particles.[97, 100] This observation is supported by similar uptake levels for sAuNS and nAuNS conjugates compared to pAuNS.

All in all, active targeting dictates that particle size for optimal nuclear delivery of AuNPs should not exceed ~30 – 50 nm. Now that particle stability, biocompatibility and nuclear targeting is established, the next step is to evaluate the radiosensitization potential of the gold nanosphere (AuNS) conjugates *in vitro*. In Chapter III, we explore the ability of the AuNSs localized to the nucleus of tumour cells to enhance the effects of radiation to a great extent than AuNSs in the cellular cytoplasm. Based on the data presented here and previous studies, dose enhancement in the area surrounding the AuNS is the inevitable consequence of irradiating any medium containing the nanoparticles.

## 2.5 Supporting information

Additional characterization performed with the help of collaborators further confirmed synthesis and purification of AuNSs. First, mass spectrometry imaging was performed with the help of Dodge Baluya at the core. This is to corroborate the characterization studies that the peptide is indeed attached to the AuNS and not suspended in solution. Figure 2.12 displays the spectra of several solutions. Although the spectrum for the NLS peptide shows a peak at 1559 (A), this peak is shifted to 1603 when after conjugation to an AuNS. This is consistent with conjugation to both 5 nm (synthesized in-house) and 20 nm (purchased from NanoHybrids).

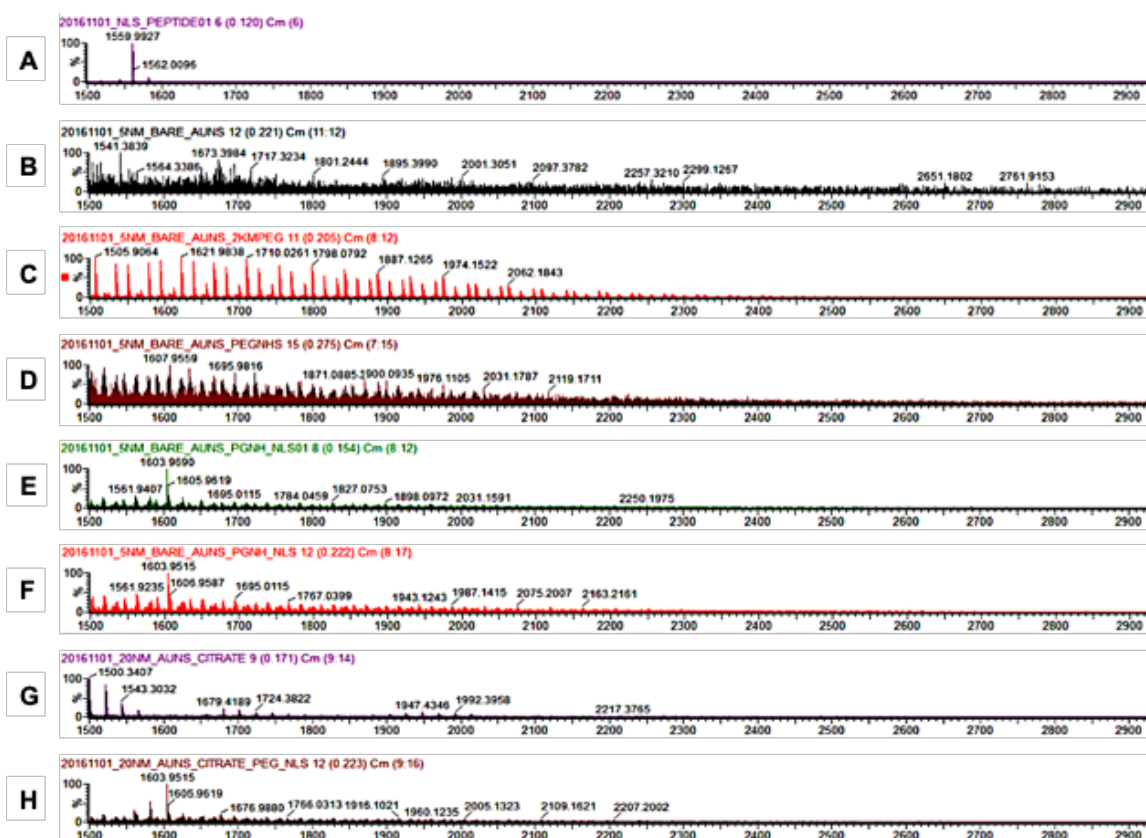


Figure 2.12. AuNS mass spectrometry imaging. Spectra of NLS and AuNS solutions to confirm conjugation as follows: (A) NLS, (B) Bare 5 nm AuNS), (C) PEGylated 5 nm AuNS, (D) 5 nm AuNS conjugated with bifunctional PEG prior to peptide addition, (E – F) 5 nm AuNS from separate synthesis batches, (G) Bare 20 nm AuNS, and (H) 20 nm AuNS with peak at 1603, similar to E and F.

Energy-dispersive X-ray spectroscopy (EDX) was performed by Onur Sahin at Rice University to confirm purification of conjugation AuNS formulations from the bare AuNS solution. Displayed in Figure 2.13 below are EDX sample and spectrum images of the synthesized bare AuNS (top) and filtered nAuNS (bottom). The S component detected if from sulfur that is present in the wafer on which the samples are placed. The Cl and Na detected are from the reagents of AuNS synthesis which are notably absent in the nAuNS sample below.

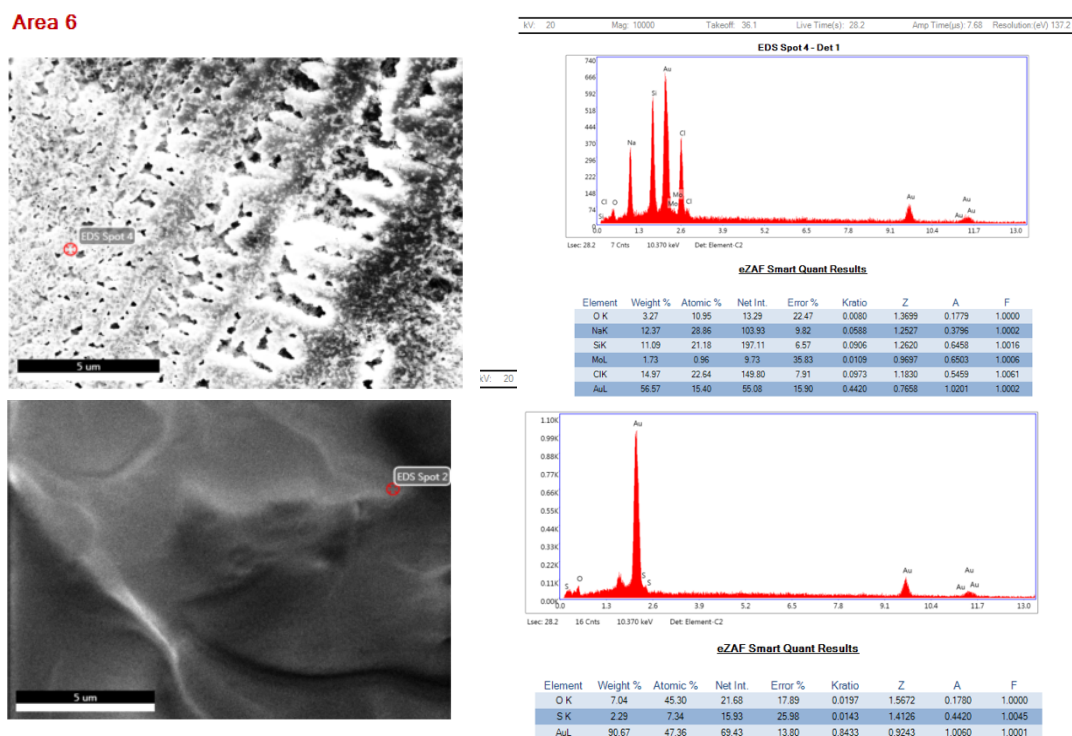


Figure 2.13. EDX analysis of unconjugated and conjugated AuNS. Top – Bare AuNS sample image and associated spectrum showing presence of synthesis reagents. Bottom – nAuNS sample image and associated spectrum with highest detection of Au and no reagent elements detected.

## 2.6 Materials and methods

General protocols such as cell culture or imaging, as well as additional details are outlined in the appendix.

### AuNS synthesis, conjugation and characterization

Gold nanospheres (AuNSs) were synthesized using a bottom-up approach through reduction of hydrogen tetrachloroauric acid ( $\text{HAuCl}_4$ ) with sodium borohydride ( $\text{NaBH}_4$ ) through a modified protocol used by Martin et al.[113] Briefly, equal molar amounts of  $\text{NaBH}_4$  and  $\text{HAuCl}_4$  dissolved in Milli-Q water were combined while stirring with a magnetic stirrer. Volumes were scaled up depending on the needs of the experiment. Methoxy-polyethylene glycol 2000 thiol (mPEG-2K-SH) and bifunctional thiol polyethylene glycol amine ( $\text{NH}_2$ -PEG-2K-SH) purchased from NanoCS were added to AuNS solutions at  $4^\circ\text{C}$  and the reactions allowed to occur for 24-48 hrs to PEGylate the particles. Two peptides, a nuclear localization sequence (GRKKRRQRRRPQ) and another peptide with similar molecular weight (Pyr-LYENKPRRPYIL), were further conjugated to the particles with the bifunctional PEG. Ultraviolet-visible (UV-vis) spectroscopy, dynamic light scattering (DLS) and zeta potential measurements were used to characterize AuNS during and after synthesis.

### AuNS toxicity and uptake studies

All experiments were performed by first plating cells at a density of 50,000 cells/mL followed by a 24 hr incubation period to allow for cell attachment. Cells were then treated according to assigned groups (control, pAuNS, sAuNS and nAuNS) for 24 hrs, and rinsed 3 times with phosphate buffered serum (PBS). Uptake studies were performed in T75 flasks with cells trypsinized following 3 PBS rinses and pelleted for digestion with *aqua regia* for ICP-MS analysis.

Nanoparticle cytotoxicity was assessed using the 3-(4,5-dimethylthiazol-2-yl)-2,5-diphenyltetrazolium bromide (MTT) kit (Roche, Sigma-Aldrich). Studies were carried out by

plating cells in 96-well plates, followed by treatment, rinsing and allowing the cells to grow for 120 hrs. Following this incubation period, MTT reagent (5 mg/mL) was added to cells, incubated at 37°C for 4 hrs in the dark and formazan crystals were dissolved using DMSO. The absorbance was measured on a plate reader (Cytation™ 5 Cell Imaging Multi-Mode Reader, BioTek Instruments) at an excitation wavelength of 590 nm and normalized to respective control cells. Each experimental treatment group was tested in triplicate for each concentration, and with 2 separate AuNS synthesis batches.

### **Subcellular localization**

Cellular fractionation was performed using the subcellular protein fractionation kit for cultured cells from ThermoFisher (Cat #78840). Western blot analysis was performed courtesy of the Welsch lab at UT MD Anderson cancer center. Briefly, protein content in the cytoplasmic and nuclear lysates were quantified using the Bradford assay. Samples were then aliquoted for Western blot analysis and quantification of gold content by inductively coupled plasma mass spectrometry (ICP-MS).

## Chapter III: *in vitro* radiosensitization

### 3.1 Abstract

A fundamental tenet of cancer nanomedicine is to effectively deliver therapeutics to cancer cells to improve anti-tumor activity and reduce the collateral effects in normal tissues. Here, we report combination therapy using nuclear targeted gold nanoparticles coupled with radiation therapy for pancreatic cancer treatment. The nanoparticles accumulate in the tumor microenvironment via the enhanced permeability and retention effect, while a nuclear localization sequence conjugated to the gold nanoparticle drives uptake into the nucleus of the tumor cells as presented in Chapter II. Here, we demonstrate that nuclear localization of gold nanoparticles boosts the effect of radiation therapy when compared to treatment with radiation therapy alone, or in combination with nanoparticles sequestered in the cell cytoplasm. This sensitization results from the production of secondary electrons (Figure 3.1) following the interaction between gold and radiation and is mediated, in part, by increased production of reactive oxygen species and DNA double strand breaks. Furthermore, we establish the effects of combined therapy on cell metabolism, mitochondrial membrane potential and the cell cycle to further elucidate the mechanism of gold nanoparticle-mediated radiosensitization.

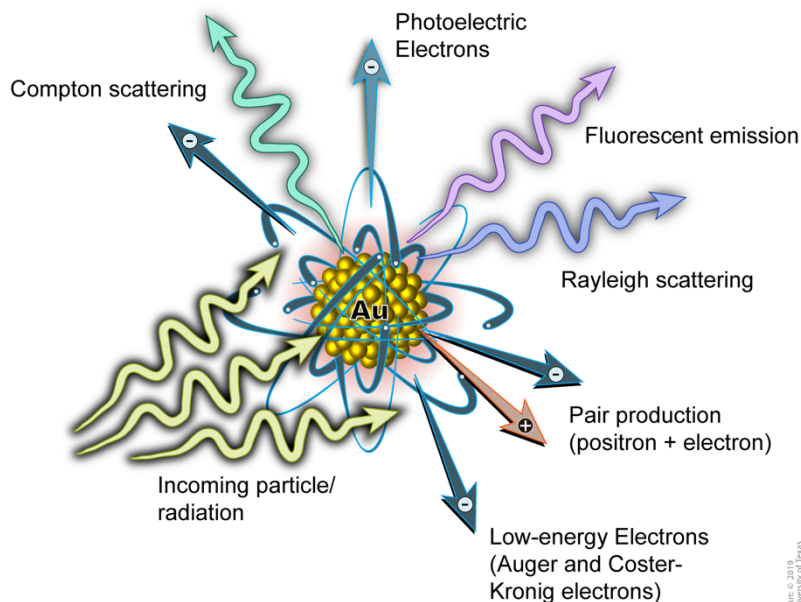


Figure 3.1. Chapter III graphical representation. Gold nanoparticle-mediated radiosensitization postulated to occur via secondary electron production. Adapted from illustration by Briggs S, and Hattar, K. *Evolution of Gold Nanoparticles in Radiation Environment* [114]

### 3.2 Introduction

Irradiation of tumours laden with high atomic number ( $Z$ ) materials such as gold results in radiation dose enhancement via increased secondary electron production from nanoparticle-radiation interactions.[75, 115, 116] The augmented density of ionization localized near or at the surface of the AuNPs leads to enhanced probability of lethal damage to cells containing the materials by transiently increasing the radiation-interaction cross section in the target tissue. A study 40 years ago demonstrated the radiosensitization potential of iodine in cultured cells.[117] This was later validated *in vivo* when injection of iodine into tumors followed by radiation resulted in roughly 80% suppression of tumor growth in mouse models.[118] Gold has been pursued as a radiosensitizer given its higher  $Z$  than iodine (Au,  $Z = 70$  vs. I,  $Z = 53$ ) and biocompatibility.[75] Studies investigating the concentrations of high  $Z$  materials with radiation found that in order to achieve radiosensitization, higher concentrations of iodine and gold ( $\sim 5\text{mg/g}$ ) were required.[75, 119]



When the gold nanoparticles (AuNPs) were internalized *in vitro*, however, radiosensitization effects were observed at concentrations as low as  $10^{-6}$  mg/g.[115] These results are consistent with previously published work demonstrating *in vitro* sensitization with AuNP concentrations of  $\sim 10^{-3}$  mg/g at both kilovoltage (kV) and megavoltage (MV) energies of radiation.[120] Based on these observations, it is possible to achieve radiosensitization effects at considerably lower concentrations, given intra-cellular or sub-cellular accumulation of AuNPs. Although the mechanism of radiosensitization at such low concentrations is not well understood, it is generally accepted that the efficacy *in vivo* reported is attributable to an increase in photoelectric absorption interactions due to the high Z of gold. The high Z increases the scattering cross section and production of resulting in greater physical damage to tumour cells, as well as endothelial cell lining the blood vessels. The damage observed via production of photoelectrons and Auger/Coster-Kronig electrons, however, was observed with large quantities of gold on the order of g gold/kg body weight. With this amount of gold, the mouse turned blackish blue following injection, reinforcing that the tumor gold content is generally an index of tumor vascularity with the AuNPs serving as contrast agents.

The amount of gold injected, content in tumor, timing of radiation (2min following injection) and radiation used (26 Gy using 250 kVp X-rays) make this approach clinically impractical. Nevertheless, this report laid the foundation for more in-depth evaluation of AuNP-based radiation dose enhancement, and with it, active targeting strategies of AuNPs. We examine the passive cell uptake and active nuclear targeting in the previous chapter. Here, we investigate the radiosensitization potential of nuclear localization as well as the mechanisms by which radiation dose enhancement occurs. Additionally, we explore the biologic effects of the quality of RT through linear energy transfer (LET) and radiobiological effectiveness with the addition of AuNSs to the treatment regimen.

### 3.3 Results and discussion

Optimizing design of AuNPs for radiosensitization requires knowledge of the physiochemical interactions of nanoparticles with cells in culture and tissues, as well as the changes in radiation treatment instigated by the presence of the particles in the treatment field. Additionally, the physical mechanisms of dose enhancement are contingent on the radiation modality. In this chapter, we explore the radiosensitization potential of the nAuNSs with different types of radiation, as well as the various processes by which dose enhancement occurs.

#### Clonogenic assays

The clonogenic assay is the classic *in vitro* cell survival assay that evaluates cell death based on a single cell's ability to produce a colony, defined as at least 50 cells. Simply, single-cell suspensions of the tumor cells are prepared from each treatment group (control, pAuNS, sAuNS or nAuNS at each RT exposure), and plated under identical conditions. We plate a larger number of cells with increasing RT dose in anticipation of greater cell kill with the higher RT dose. After the incubation period, we determine the plating efficiencies in each treatment group and calculate the surviving fractions. This is outlined in the supporting information.

We assess the radiosensitization potential using an orthovoltage RT beam (320 kVp XRAD320). Clonogenic survival analysis noted that neither pAuNSs nor sAuNSs sensitized either cell line to radiation. However, nAuNSs sensitized both cell lines to radiation with dose enhancement factors (DEFs) calculated at the 10% surviving fraction of  $1.17 \pm 0.01$  and  $1.31 \pm 0.04$  for Panc-1 and MiaPaCa-2 cells, respectively. (Table 3.1) Representative survival curves are shown in Fig. xa and xc, with representative colony images in Figure 3.2. Based on the linear-quadratic (LQ) model, the cell survival assessment results in a linear curve with a  $\beta=0$  for the nAuNS combine with RT treatment groups in both cells. The linear curves are reminiscent of the response of mammalian cells typically observed with irradiation using higher linear energy transfer (LET) radiation ( $\text{LET} \geq 10 \text{keV}/\mu\text{m}$ ), or inhibition of DNA damage repair processes. These results demonstrate modulation of the response to low LET radiation.

Table 3.1: Dose enhancement factors and radiobiological effectiveness of combined AuNS plus RT therapy. All data presented as mean  $\pm$  standard deviation.

Cell Line	Treatment Group	DEF @ 10% Survival	RBE Relative to $^{60}\text{Co}$
MiaPaCa-2	Control	-	1.15 $\pm$ 0.05
	pAuNS	1.05 $\pm$ 0.01	1.21 $\pm$ 0.05
	sAuNS	1.08 $\pm$ 0.02	1.24 $\pm$ 0.03
	nAuNS	1.17 $\pm$ 0.01	1.35 $\pm$ 0.04
Panc-1	Control	-	1.28 $\pm$ 0.10
	pAuNS	1.05 $\pm$ 0.03	1.34 $\pm$ 0.07
	sAuNS	1.09 $\pm$ 0.06	1.38 $\pm$ 0.05
	nAuNS	1.31 $\pm$ 0.04	1.66 $\pm$ 0.12

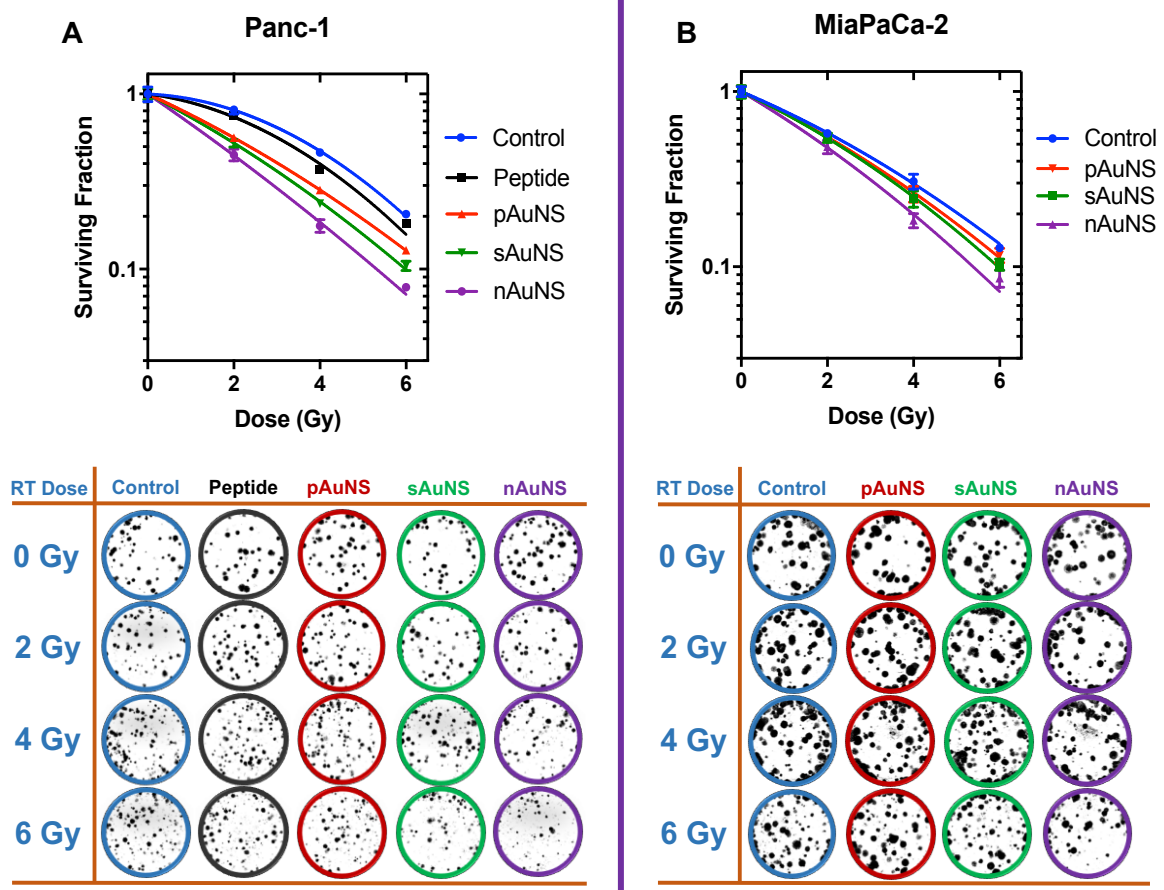


Figure 3.2: Clonogenic survival analysis. Clonogenic survival curves of Panc-1 (A) and MiaPaCa-2 (B) cells with representative images of stained colonies for each cell line. Results confirm radiosensitization with pAuNS, sAuNS and nAuNS with the greatest radiosensitization being with nAuNS.

## **Radiosensitization potential with various RT sources**

Observable effects of AuNP-mediated radiosensitization were originally postulated to occur with high gold concentration and kilovoltage photon treatments. This physical phase is a result of interactions between charged particles and atoms in the medium. The photoelectric cross section of gold for kV photons is larger than that in soft tissue, given the L- and K-shell electron excitation energies for gold. Additionally, the emissions of the inner shell electrons produce a cascade of low energy Auger and Coster-Kronig electrons that deposit the energy in close proximity to the AuNP. However, in order to prove the potential for clinical translation, the radiosensitization potential is also shown in a megavoltage photon beam, which is the most commonly utilized RT modality for cancer therapy, and protons.

Consequently, we evaluate the effect of AuNS treatment combined with a variety of radiation modalities. Clonogenic cell survival assays are performed to evaluate the radiosensitization effect after irradiation with 320-kVp X-rays,  $^{137}\text{Cs}$ -137,  $^{60}\text{Co}$ , 6 MV and 100 MeV protons (LET 2.5 and 7.8 keV/ $\mu\text{m}$ ). These studies reveal significantly higher radiation DEFs at 10% survival fraction for nAuNS compared to pAuNS for all beams assessed. Protons with higher LETs resulted in greater clonogenic cell death in comparison to low LET protons, and nAuNS further increased radiosensitization whereas pAuNS do not. This further supports that, across a spectrum of radiation energies and LETs, nuclear-targeted gold nanoparticles enhance radiosensitization beyond that achievable with strictly intracytoplasmic gold nanoparticles. These data are represented in Table 3.2. We seek to understand the underlying mechanisms of radiosensitization in the following sections at the chemical and biological phases.

Table 3.2: Radiation enhancement factors as a function of LET.

Source	LET (keV/μm)	REF for pAuNS	REF for nAuNS
Cs-137	0.5-0.8	1.03	1.10
Co-60	0.2	1.14	1.38
250 kVp	2	1.07	1.35
6 MV	0.35	1.07	1.22
Proton	2.58	1.04	1.21
Proton	7.8	1.08	1.16

### Reactive oxygen species

Damaging effects of radiation principally result from the ability to ionize or eject electrons from molecules within cells. A majority of the biological damage, however, is produced by the ejected electrons which cause further ionizations during their collision with other molecules. This ionization and excitation disrupt chemical bonds and form fragmented molecules known as free radicals.[121] These free radicals are highly reactive and instigate a cascade of reactions that eventually restore the overall electronic charge equilibrium. This chemical phase is underscored by the competition between scavenging reactions with molecules that inactivate the free radicals and the cascade of interactions to yield stable chemical changes to the molecules. Oxygen is relatively susceptible to radical formation such as hydroxyl ions, hydroxyl radicals, peroxide, hydrogen peroxide (H<sub>2</sub>O<sub>2</sub>) or superoxide ions.

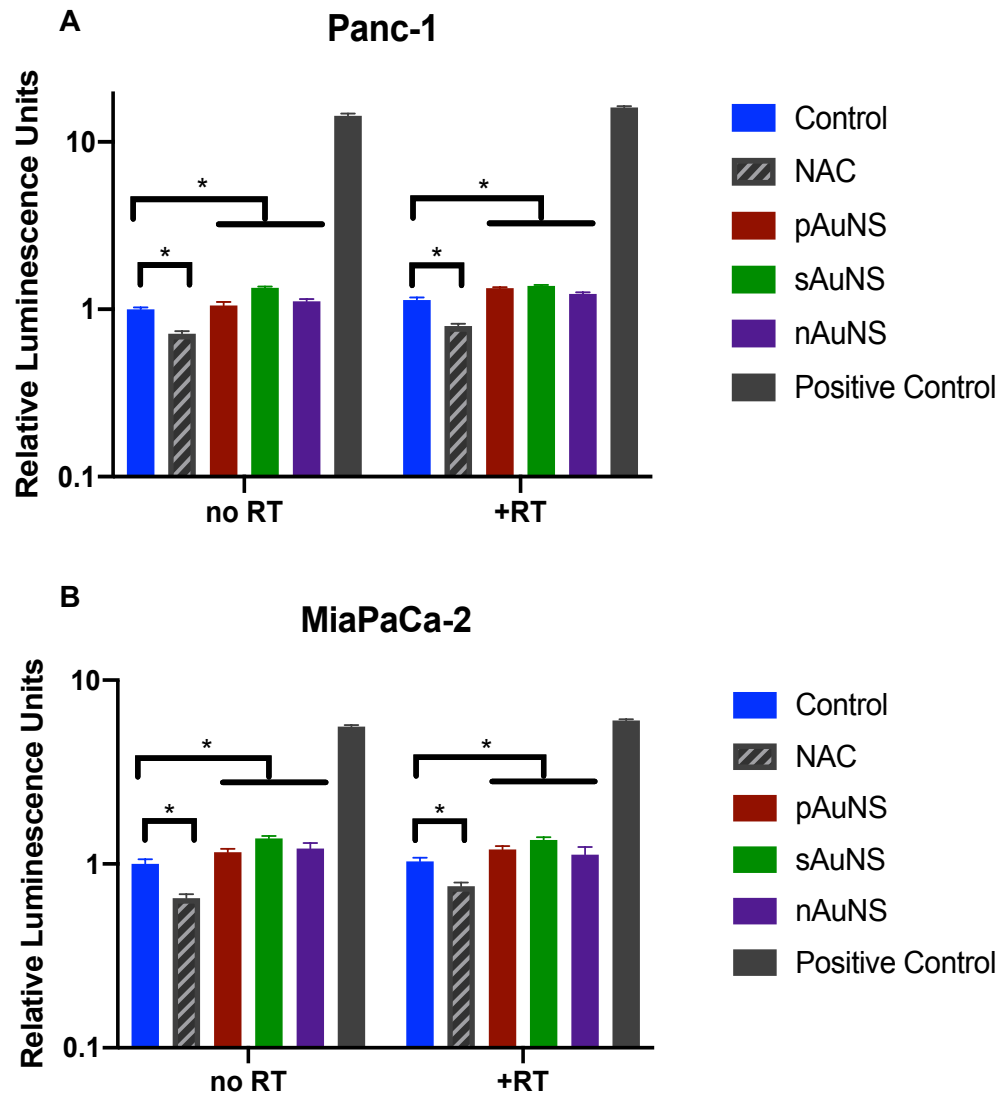


Figure 3.3: Reactive oxygen species production. ROS production in Panc-1 (A) and MiaPaCa-2 (B) cells treated with AuNSs with or without RT. No difference in ROS production observed in groups treated with pAuNS, sAuNS or nAuNS.

Free radical reactions transpire within a few milliseconds of radiation exposure. As such, we employ several design aspects to measure the effects of AuNS presence in the cells. The kit chosen measures  $\text{H}_2\text{O}_2$  levels because various ROS are converted to as a final product, and it has the longest half-life to maximize detection. Although we found a statistically significant difference in ROS production between the control and AuNS-treated groups ( $p < 0.01$ ), there was no difference between the nAuNS and non-nuclear targeted AuNS groups (pAuNS and sAuNS). Treatment with N-acetylcysteine, a glutathion precursor, results in a statistically significant decrease in  $\text{H}_2\text{O}_2$  detection for both control and RT-treated experimental groups. Based on these results, we expect that any downstream ROS-mediated damage is independent of the type of conjugate in the AuNS-treated groups.

### **DNA strand break assessment**

All subsequent processes progressions following the physical and chemical phases make up the biological phase, which generally begins with enzymatic reactions to the damage produced in the physical and chemical phases. This includes repairing lesions created in several cell components, especially DNA. Due to importance of DNA and complexity of replication for cell proliferation, several mechanisms of repair exist to maintain DNA integrity. For damage caused by ionizing radiation, amino acid bases are repaired via base excision repair (BER), single strand damage by single strand break repair (SSBR), and double strand breaks (DSBs) through either homologous recombination (HR) or non-homologous end-joining (NHER). Studies have shown that other repair processes, such as mismatch repair (MMR) and nucleotide excision repair (NER), play a minor role for RT.[122] This DNA damage response (DDR) is initiated by recruitment of several proteins to the site of damage.



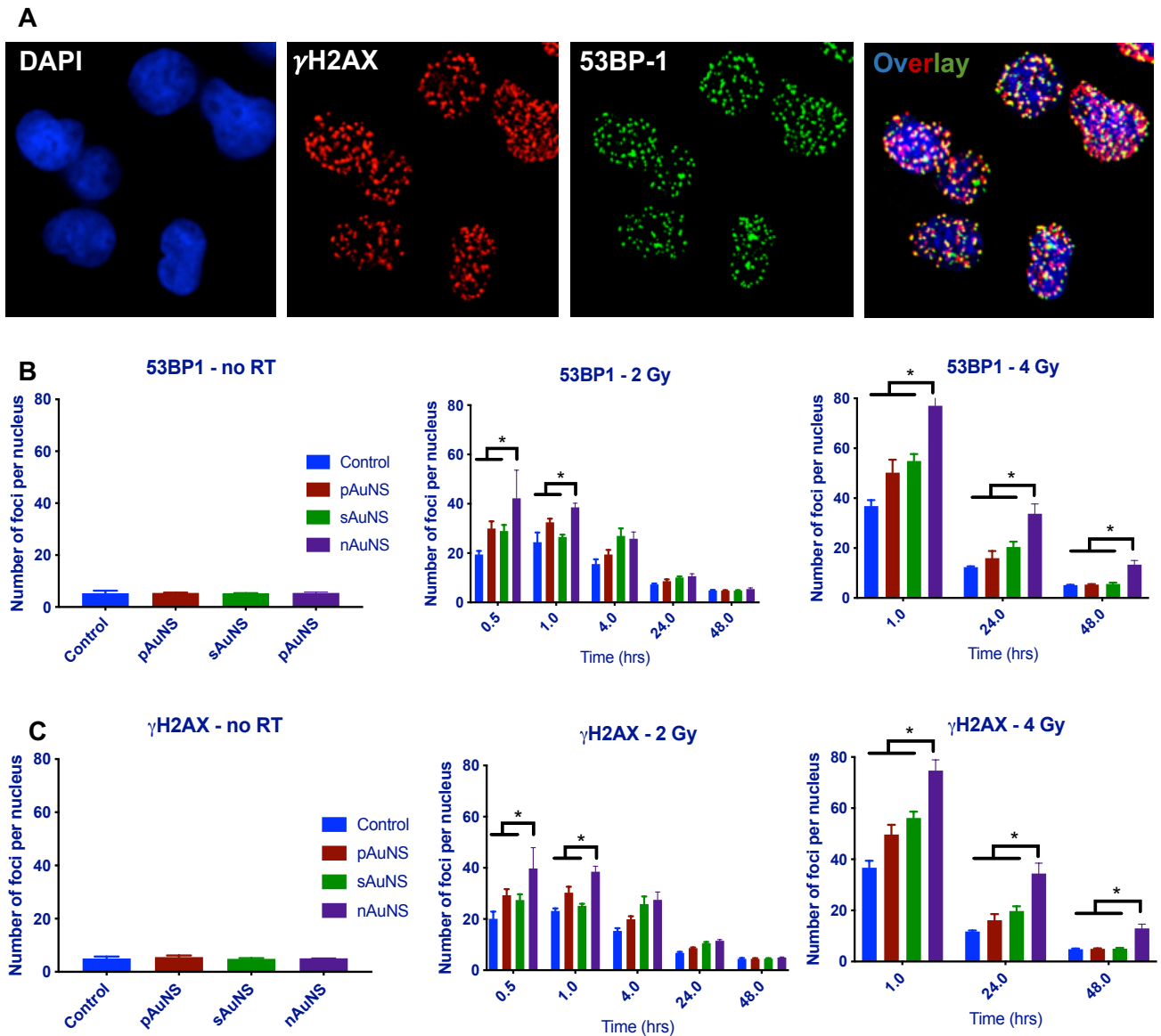


Figure 3.4: DNA DSB evaluation. (A) DNA double strand break formation assessment using 53BP-1 and  $\gamma$ H2AX immunofluorescence staining. Quantitative analysis of the number of 53BP-1 (B) and  $\gamma$ H2AX (C) foci per nucleus at different time points following no RT, 2 Gy and 4 Gy. ns = not significant; \* = p < 0.001.

One of the first events in this cascade of events is phosphorylation of the H2AX protein into  $\gamma$ H2AX. As such, we measure the expression and disappearance of this protein, along with 53BP-1, as surrogates in order to assess the effects of the AuNSs on the kinetics of DNA DSBs. We evaluate DNA DSBs through immunofluorescence analysis of  $\gamma$ H2AX and 53BP-1 foci generated in the nuclei (Figure 3.4a), and found no difference in expression for control and AuNS-treated groups in the absence of RT. However, 2 Gy RT resulted in increased levels of 53BP-1 foci at early timepoints (Figure 3.4b) with a gradual decline to normal by 24 - 48 hrs post-RT ( $p < 0.001$ ). This was more pronounced with nAuNS than the other AuNSs. Greater numbers and longer persistence of foci were noted after 4 Gy RT, with preservation of foci for up to 48 hrs post-RT in the nAuNS treatment group ( $p < 0.001$ ). Similar results were observed for  $\gamma$ H2AX foci (Figure 3.4c). Additionally, we utilize the comet assay to determine the extent of DNA damage beyond DSBs identified via foci staining.

Single cell gel electrophoresis, also known as the comet assay, permits evaluation of DNA damage at the single cell level. We perform the assay under alkaline conditions in order to detect the cumulative DNA damage from single-strand breaks, cross-linking and incomplete repair sites in addition to double strand breaks. Furthermore, we distinguish the effects of AuNS treatment with or without RT on producing this DNA damage. We report these effects in measurements of both tail length and tail moment (Figure 3.5). Overall, combined AuNS treatment with RT resulted in significantly longer tail length and higher tail moment measurements, with nuclear targeting exerting the greatest effect with RT. Statistical analysis reveals significant differences in treatment groups, as indicated on the graphs, with p values as follows: no RT vs RT only ( $p < 0.02$ ), sAuNS vs. nAuNS ( $p = 0.0004$ ) and  $p < 0.0001$  between all other groups. These observations affirm the hypothesis that nuclear targeting of AuNSs results in higher DNA damage.

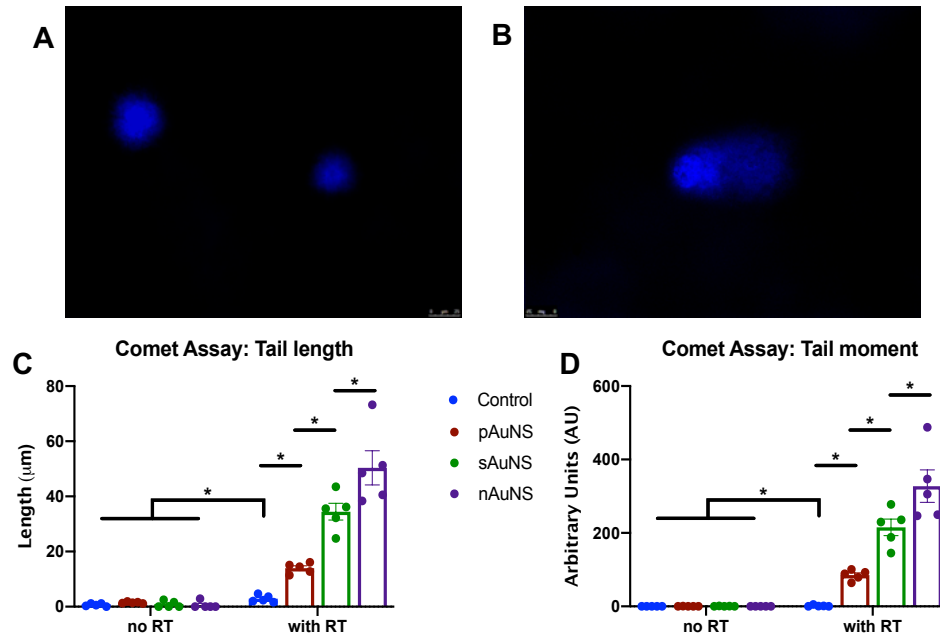


Figure 3.5: Comet assay analysis. Results of alkaline single cell gel electrophoresis. (A) Representative DAPI stained cells from no RT treatment group and (B) representative image from RT-treated group. Analysis of (C) tail length and (D) tail moment measurements from minimum  $n = 50$  from each experimental group.

## **DNA repair analysis**

The increased number in DSB foci present, increased DNA damage measurements from the comet assay, and the loss of the shoulder in the cell survival curve suggest that inhibition of the DNA repair process might be at play. In order to rule out the possibility that the enhanced cell kill might be a result of DNA repair inhibition by the AuNSs, we perform a split-dose assay as shown in Figure 3.5. We fractionate a single 4 Gy RT dose into 2 x 2 Gy doses separated by 24 hours. This provides ample time for DNA DSB repair to occur prior to the second dose. The surviving colonies and recovery ratios are represented in Table x. Given the higher survival with the fractionated RT regimen relative to the single higher dose, we conclude that the presence of these AuNSs, even in the nucleus, do not significantly hamper DNA repair. This is further validated by the calculated recovery ratios that indicate no decrease relative to the in the AuNS-treated groups relative to the RT only group (Table 3.3). Recovery ratios are obtained by dividing the surviving fraction for the single dose by split dose.

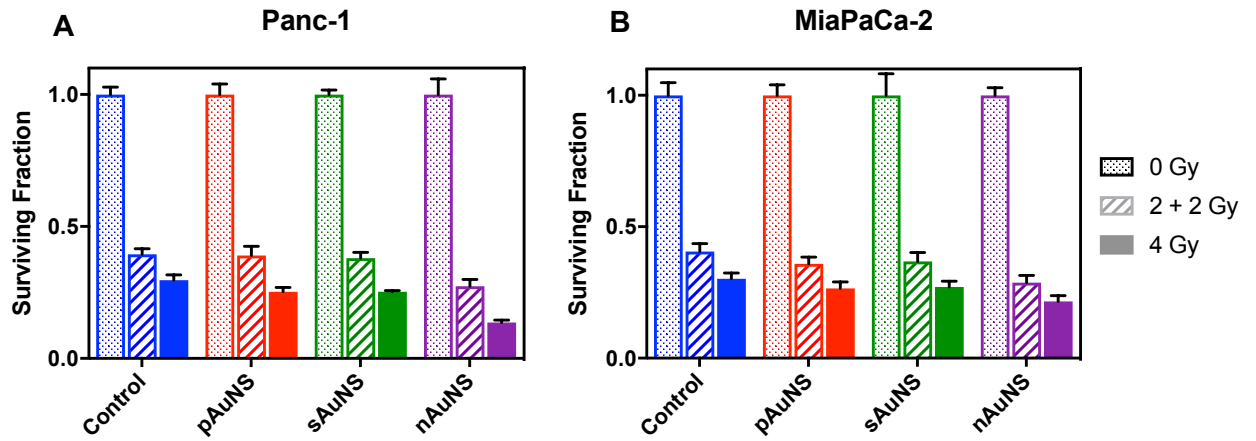


Figure 3.6: Split dose clonogenic assay. Split dose clonogenic survival assay in Panc-1 (A) and MiaPaCa-2 (B) cells radiated to 4 Gy compared to 2 fractions of 2 Gy each.  $p < 0.001$  between RT doses in each treatment group, as well as AuNS treatment groups

Table 3.3: Recovery ratios for split dose assay.

Cell type	Treatment	Single dose SF	Split dose SF	Recovery Ratio
Panc-1	Control	0.2969	0.3943	1.328
	pAuNS	0.2529	0.3904	1.544
	sAuNS	0.2528	0.3797	1.472
	nAuNS	0.1365	0.2739	2.001
MiaPaCa-2	Control	0.3020	0.4053	1.342
	pAuNS	0.2656	0.3587	1.351
	sAuNS	0.2707	0.3684	1.361
	nAuNS	0.2160	0.2908	1.346

## Cell cycle evaluation

The second crucial effector pathway, following H2AX phosphorylation, is cell-cycle checkpoint activation. RT exposure results in delays in progression through the G1, S and G2 phases of the cell cycle.[123] Many tumour cells contain genetic mutations such as p53 or BRCA1 that render several of the checkpoints disabled. The late G2 checkpoint, however, has been shown to affect radiosensitivity because it is predominantly ATR dependent. As such, we carry out cell cycle analysis at several time points following a single 4 Gy dose of RT. Generally, cell cycle analysis also shows minimal effects of AuNS treatment (nuclear targeted and non-targeted) alone across all three cell lines (Figures 3.7 – 3.10). Of all phases of the cell cycle, the S-phase appears least affected by RT exposure across all three cell lines. The percentage of cells in sub-G1 is independent of RT exposure, and relatively low for HPDE and Panc-1 cell lines (< 6%) but slightly higher for MiaPaCa-2 (~15% at select time points). The effects on cells in the S-phase suggest less importance in HPDE and Panc-1 cells, whereas MiaPaCa-2 show an initial increase in the percentage of cells followed by a decline. This is in line with our observation of faster doubling time with these cells (20 – 24 hrs) compared to the Panc-1 (30 – 48 hrs) and HPDE cells (48 – 72 hrs).

RT treatment results in an increase in the percentage of cells in the G2M phase appreciable in all cell lines but especially notable for HPDE and MiaPaCa-2. Interestingly, this increase is prominent at earlier time points (12 hr and 24 hr) for both cancer cell lines yet persistent up to 120 hours post-RT for the HPDE cell line. This suggests a more efficient and sensitive mechanism for DNA damage detection and DDR is in effect for the normal cell line compared to the cancer cell lines. The changes in the percentage of cells in G2M is inversely correlated with those in G0-G1. For HPDE, this is particularly noteworthy as the decrease in the percentage of cells in G0-G1 drastically decreases and remains low up to the 120 hrs tested here meanwhile, the percentage of cells in G2M increases and remains elevated. This change is observed for MiaPaCa-2 cells as well, however, obvious at earlier timepoints with general return to baseline levels at 48 hours onward. These differences are a bit more nuanced in the Panc-1

cells. Although there is a general change (G2M increase vs G0-G1 decrease) with RT exposure, there is no temporal correlation with or without RT. This also follows our observation that Panc-1 cells are less radiosensitive given the wider distribution of cells in the cell cycle phases. We follow-up up these studies with evaluation of the effects of AuNS treatment and RT exposure on cell metabolism.

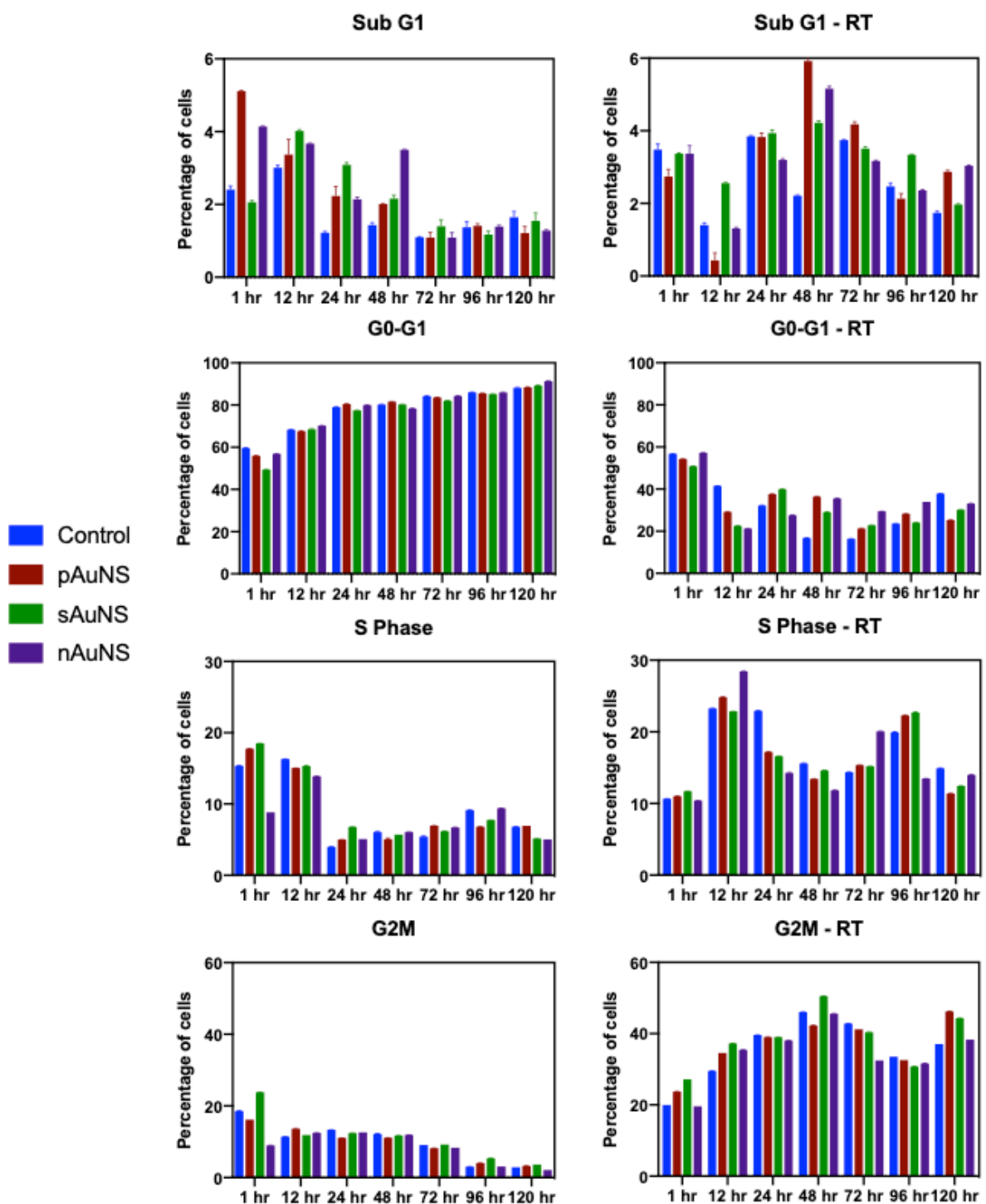


Figure 3.7: Cell cycle evaluation – HPDE. Cell cycle distribution for AuNS treatment groups at several time points with no RT exposure and following 4 Gy RT exposure. Trypsinized cells are stained with propidium iodide and flow cytometry used to measure DNA content.



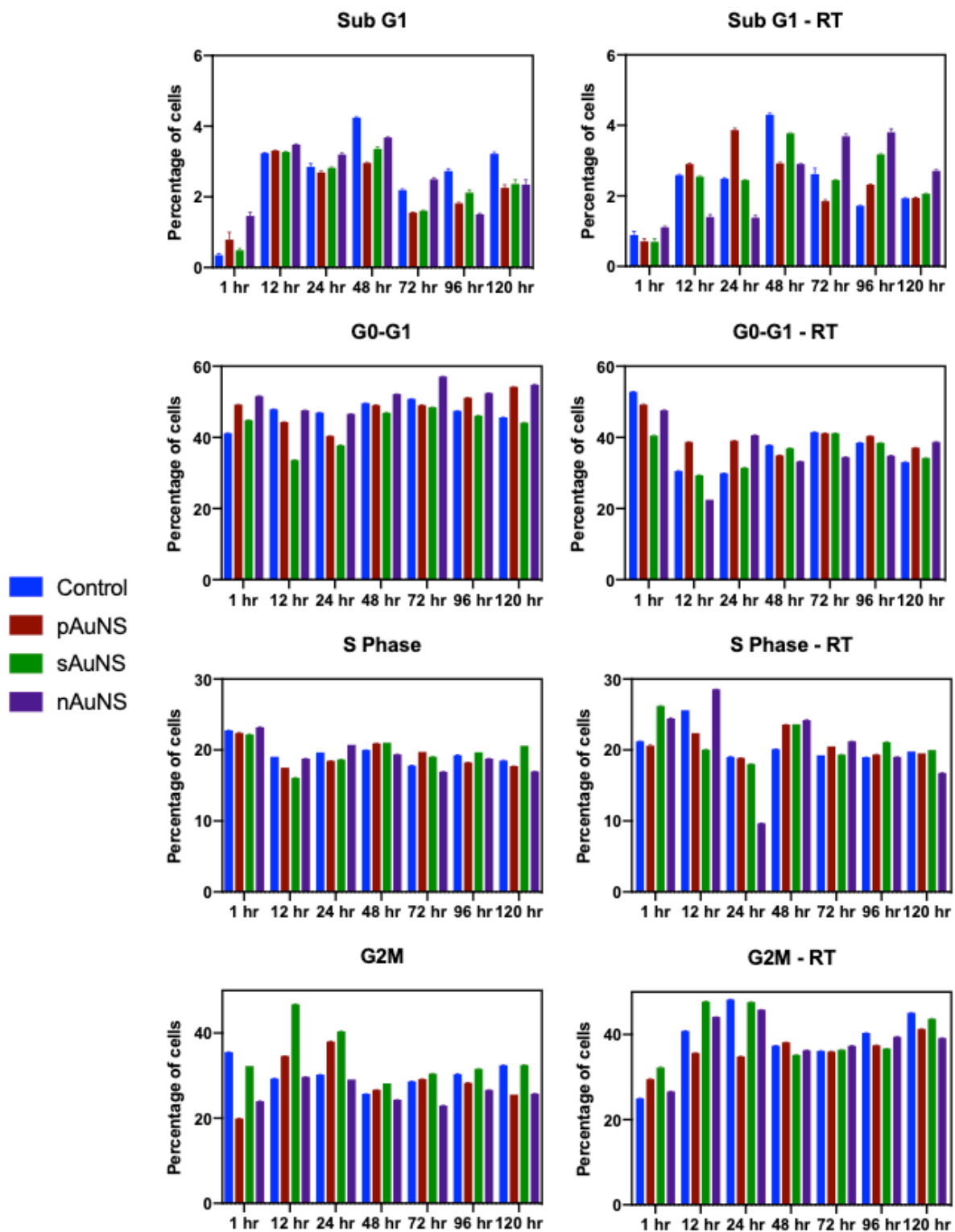


Figure 3.8: Cell cycle evaluation – Panc-1. Cell cycle distribution for AuNS treatment groups at several time points with no RT exposure and following 4 Gy RT exposure. Trypsinized cells are stained with propidium iodide and flow cytometry used to measure DNA content.

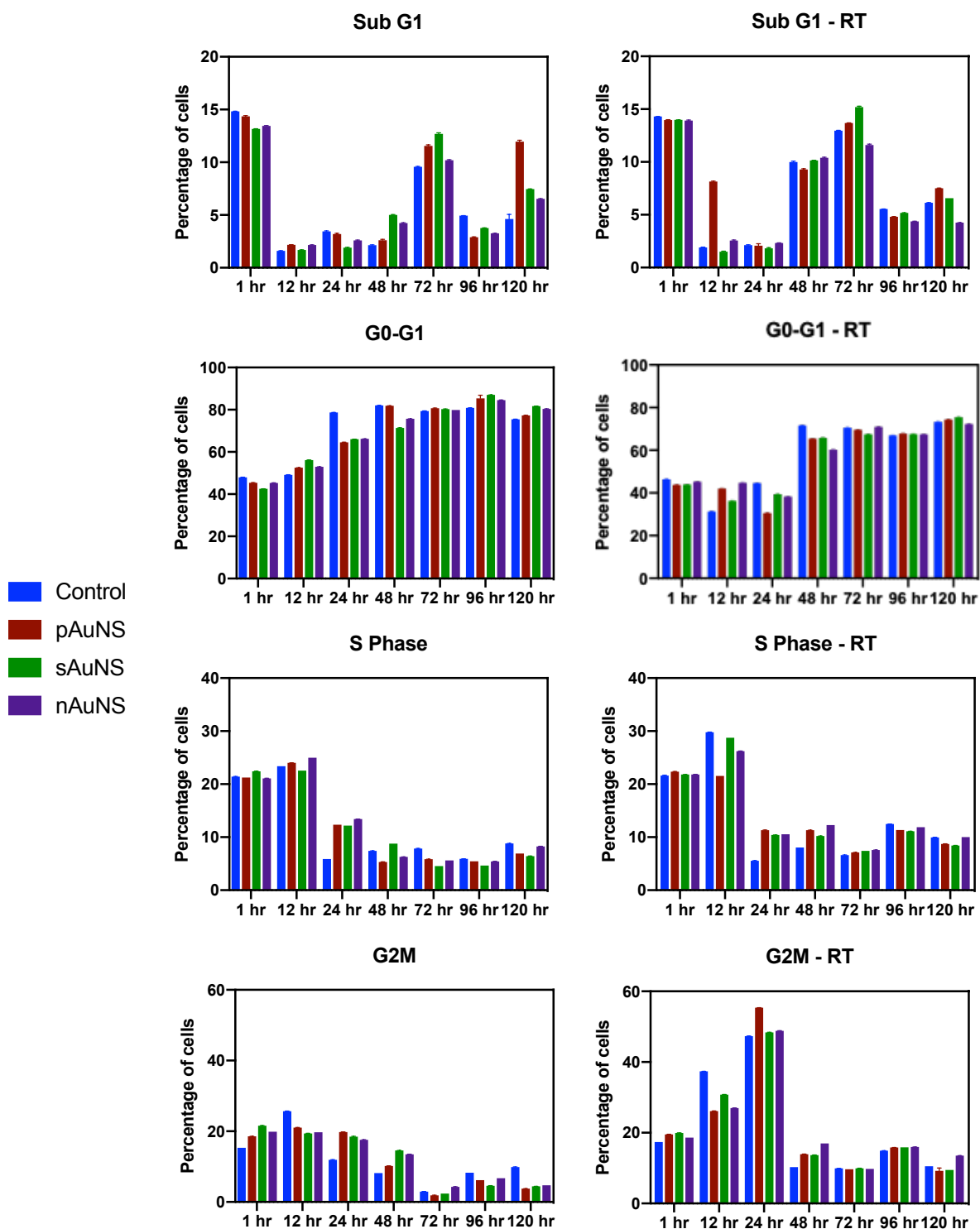


Figure 3.9: Cell cycle evaluation – MiaPaCa-2. Cell cycle distribution for AuNS treatment groups at several time points with no RT exposure and following 4 Gy RT exposure. Trypsinized cells are stained with propidium iodide and flow cytometry used to measure DNA content.

## **Effect of AuNS treatment on cell metabolism and mitochondrial membrane potential**

The Warbug effect was coined decades ago based on the observation that cancer cells produce excess lactic acid in the presence of oxygen.[124] The switch from maximal ATP production through oxidative phosphorylation to balancing energetic needs with substrate availability for rapid reproduction is termed bioenergetic reprogramming. This is dictated by mitochondria along with several fundamental parameters such as energy production, ROS generation, synthesis of biosynthetic precursor and initiation of apoptosis.[125, 126] Therefore, mitochondria are vital in various aspects of tumour progression. We study mitochondrial function was using the Seahorse assay to measure the oxygen consumption rate (OCR) and the extracellular acidification rate (ECAR), a surrogate measure of glycolysis.

Seahorse assay results reveal that the OCR of pancreatic cancer cells differs from that of the normal HPDE cell line, as well as the fact that ECAR is decreased in AuNS-treated groups relative to the normal cells. Data demonstrate decreased OCR and ECAR for AuNS treated cells before RT exposure relative to the untreated controls (Figure 3.10) This decline is further emphasized with RT. These effects, however, did not vary significantly between nuclear targeted and non-targeted GNP treatment groups. This is consistent for both cancer cell lines, as well as the normal HPDE cells. As well, AuNS treatment reduces the reserve capacity of normal and pancreatic cancer cells with or without RT. This is especially true for the normal pancreatic cancer cell line displaying the highest reserve capacity of the three cell lines. ECAR levels, though closer in range for all three cell lines, decrease with nAuNS treatment. Of note, baseline OCR but not ECAR levels are lower for the HPDE cells than the cancer cells as expected.

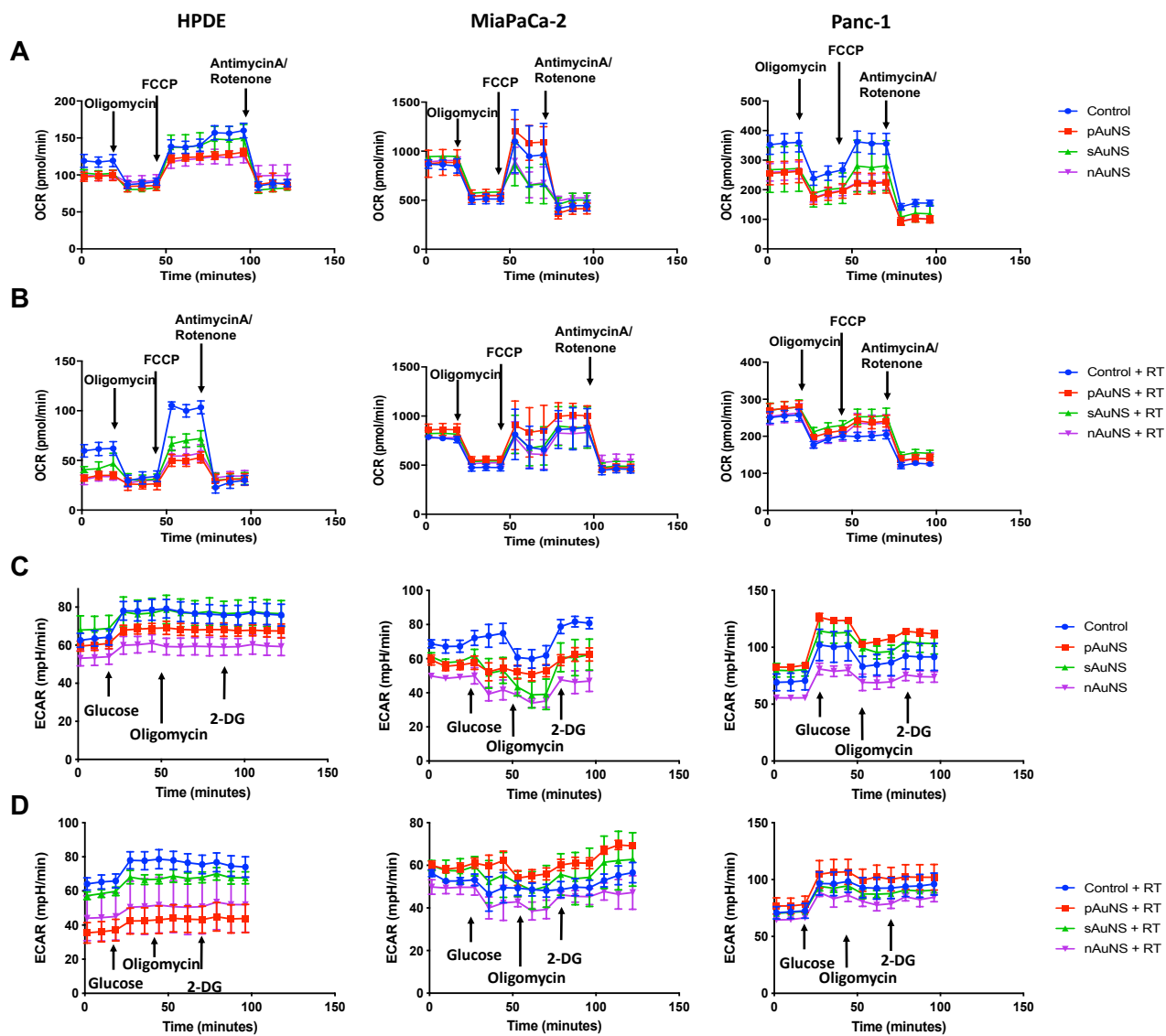


Figure 3.10: Seahorse assay for cellular metabolism. Effects of AuNS treatment on OCR without RT (A) and 1 following RT exposure (B). Similar results on ECAR with (C) and without (D) RT exposure. Arrows indicate points at which reagent is added during the assay.

This observation is further validated by the study into the effects of the AuNSs on the mitochondrial potential. Mitochondrial activity measured by the membrane potential following 24 hours of AuNS treatment without RT shows no statistically significant difference between control vs AuNS-treated groups. After RT exposure, there is decreased activity in the groups treated with AuNS when compared with singular treatment with RT or AuNS conjugates (Figure 3.11). Slow increase of the fluorescent intensity is observed overtime. These membrane potential studies and metabolic seahorse results are congruent with findings from the ROS assays showing no difference in subcellular localization of AuNSs. This further supports the notion that physical dose enhancement, as evidenced by the effects of nAuNS in close proximity to the nucleus, from local secondary electron showers is the major mechanism for radiosensitization.

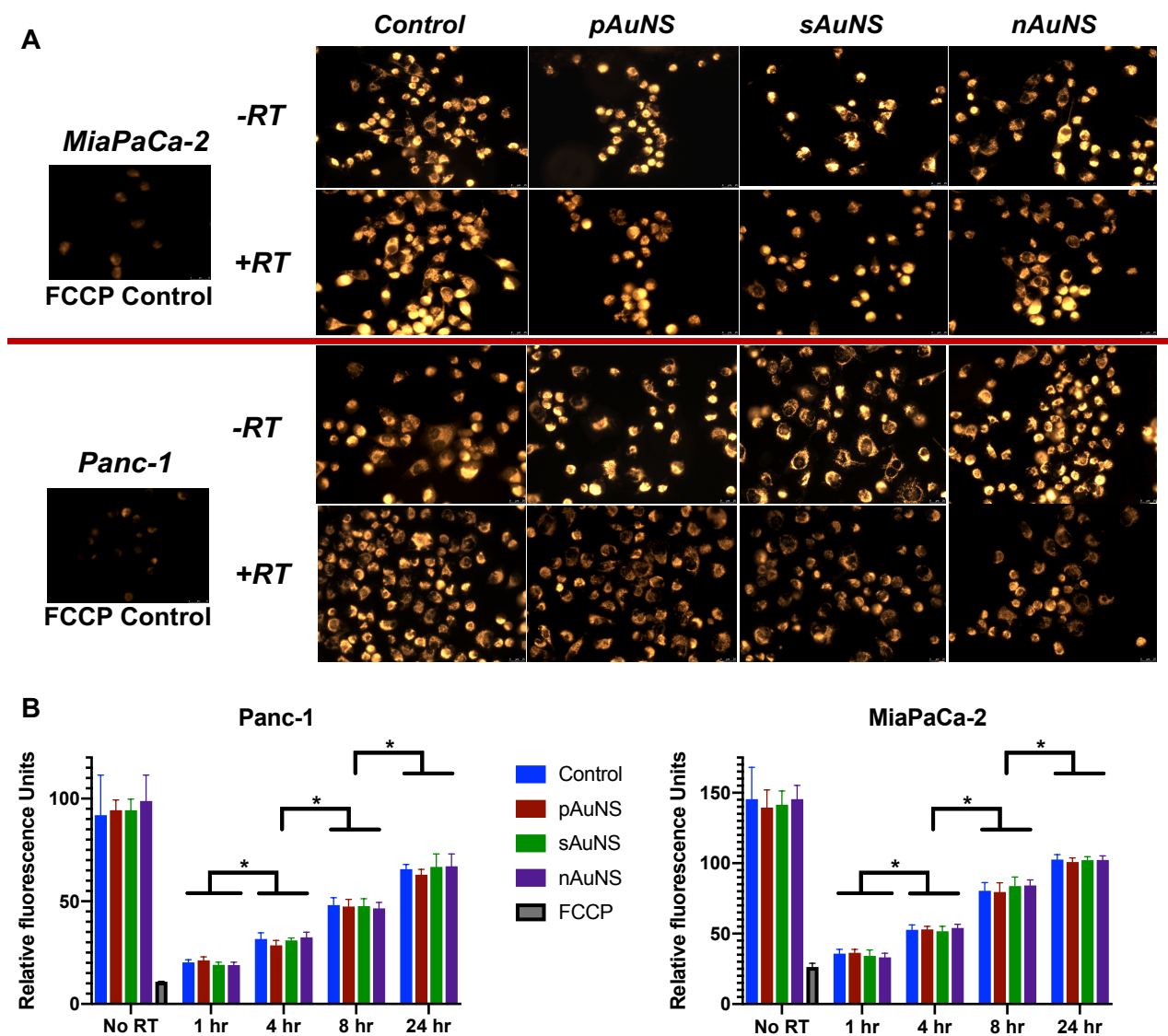


Figure 3.11: TMRE assay. Effects of AuNS treatment on mitochondria membrane evaluated at several time points in MiaPaCa-2 and Panc-1 cells, compared to the negative control treatment will FCCP. (A) Imaging at 24 hours post RT treatment and respective control groups. (B) Quantitative analysis of fluorescence intensity,  $p < 0.001$ .

### 3.4 Conclusion

Efficacious treatment of cancer cells with radiation results from the death of individual tumour cells following RT exposure. The benefits of RT as a treatment strategy, however, must be weighed with the effects on normal tissues. The dose response curves for tumour control and normal tissue complications make up the therapeutic index – the tumour response given a set level of normal tissue toxicity.[122] The therapeutic index equates the two responses and allows for a cost-benefit analysis of the new treatment relative to the standard. Radioprotectors and radiosensitizers are compounds that can widen the therapeutic window and allow for better tumour control, lower normal tissue complications, or both. On one hand, the ideal radioprotector shifts the normal tissue complication response curve to widen the therapeutic window because it permits tolerance of higher RT doses in the normal tissue. On the other hand, the ideal radiosensitizer moves the tumour response curve such that either a lower RT inflicts a similar level of control than a set RT dose, or more control is achieved with the comparative dose.

The efficiency of AuNP cellular internalization is determined by factors such size, shape, hydrophobicity/hydrophilicity, elasticity, surface charge and modification.[127] Clonogenic survival studies *in vitro* demonstrated potent radiosensitization with 50nm particles following irradiation with a 220 orthovoltage beam, congruent with studies suggesting 50 nm as the optimum diameter for AuNP internalization.[97, 120] Nanoparticle size dependence of radiosensitization could be a result of the secondary electrons yield with the larger number of gold atoms increasing the photoelectric interaction cross-section. Conversely, more gold atoms on the surface of the particle also attenuate the secondary electrons produced in the core of the particle through self-absorption.[128] The data presented here distinguish the radiosensitivity resulting from subcellular localization vs from quantity of AuNS uptake, particularly between the sAuNS and nAuNS treatment groups in which particle uptake is similar. Although clonogenic assay data is not available for the normal HPDE cells, we hypothesize that the AuNS, particularly the nAuNS treatment, has differential effect on tumor cells given the selective internalization in HPDE cells compared to the Panc-1 and MiaPaca-2 cells as previously described in Chapter II.

RT damage to cells is orchestrated by the secondary charged particles and free radicals produced, with DNA as the primary target. Among the cellular mechanisms we explore are increased production of oxygen free radicals and generation of DNA DSBs. Irradiation of cells laden with nAuNSs does not increase ROS production compared to accumulation with pAuNSs or sAuNSs since oxidative stress is quantified at a whole-cell level rather than within individual cellular compartments where these AuNSs differentially accumulated. However, nuclear localization of AuNSs in irradiated cells resulted in increased DNA damage that correlated with enhanced cell kill in clonogenic survival assays compared to the non-nuclear targeted AuNS groups. Furthermore, these results also suggest that sublethal damage is actively repaired following AuNS enhancement of radiation-induced DNA damage because a single dose of 4 Gy causes more clonogenic cell kill than two fractions of 2 Gy each per the split dose assay. The fact that measured ROS levels and mitochondrial function does not correlate with subcellular localization of AuNSs highlights that the higher DNA DSB production by the nAuNSs and subsequent cell kill reflect an underlying physical phenomenon incited by the proximity of the nAuNSs to DNA.

In fact, this is further highlighted by the loss of the shoulder region in the clonogenic assay curves for the nAuNS-treated group. This characteristic bending of the curve models the effect of DNA repair between RT fractions at lower doses and disappears at higher doses, or with higher quality (LET) RT. Given the results of the split-dose assay, the AuNSs here do not significantly impair DNA repair. Therefore, proximity of AuNSs to the nucleus enhance the response to a classically low LET radiation with an orthovoltage beam to mimic that of a higher LET radiation source. High-LET radiations inflict greater biological effects per Gy than lo-LET radiations. This is evident through an increase in RBE as LET increases up to roughly 100 keV/m. All things considered, we demonstrate that AuNS-mediated radiosensitization is evident across multiple types of RT, hence increasing the feasibility of clinical implementation with photons or charged particle sources.



### 3.5 Supporting information

1. Calculations for several factors discussed in this chapter are as follows:

- Survival fraction for clonogenic assays

$$SF = \frac{Dose_{10\%} \text{ for RT only}}{Dose_{10\%} \text{ for Experimental Group}}$$

- Dose or radiation enhancement factor (DEF or REF)

$$DEF_{10\%} = \frac{Dose_{10\%} \text{ for RT only}}{Dose_{10\%} \text{ for Experimental Group}}$$

- Recovery ratio

$$RR_{treatment\ group} = \frac{SF_{single\ dose}}{SF_{fractionated\ dose}}$$

2. DNA double strand break and intensity measurements from only identified cells requires identification of total cell number prior to measurements.

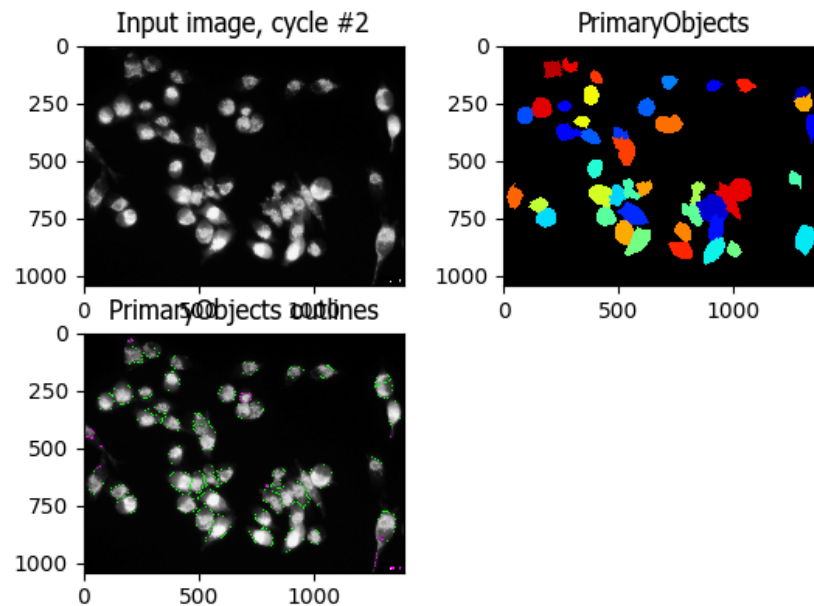


Figure 3.12: Identification of primary objects for foci and intensity measurements. Representative output for code in CellProfiler to identify and isolate cells for measurements.

### 3. Representative cell cycle analysis images from flow cytometry.

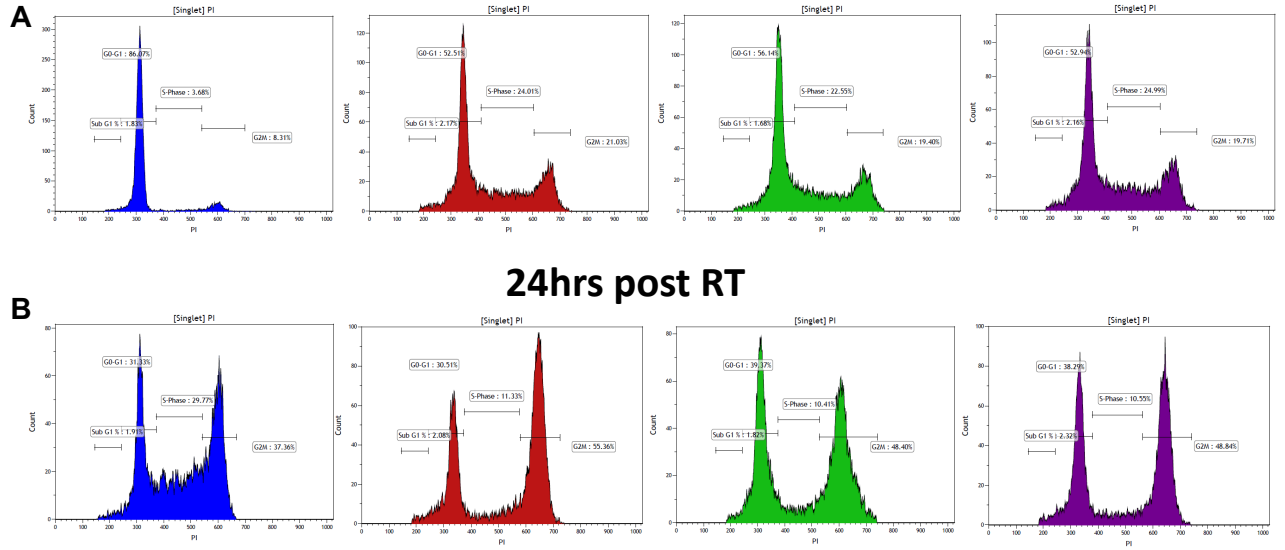


Figure 3.13: Representative cell cycle histograms for MiaPaCa-2 cell line. (A) No RT and (B) 24 hours post-RT exposure. AuNS treatment groups are: blue (control – no AuNS), red (pAuNS), gree (sAuNS) and purple (nAuNS).

### **3.6 Materials and methods**

#### **Clonogenic assays**

*In vitro* radiosensitization was evaluated for both Panc-1 and MiaPaCa-2 cell lines using the classic clonogenic assay. Briefly, cells are plated and treated with AuNSs for 24 hrs prior to RT (0, 2, 4 and 6 Gy) using XRAD 320 or the specified RT modality. The cells are harvested and a known number of cells are re-plated in sextuplicate and allowed to grow in culture for 9-14 days to allow for colony formation. The colonies are fixed and stained with 1% crystal violet in absolute alcohol, washed extensively to remove excess dye, and imaged using a colony counter (GelCount, Oxford Optronix). The numbers of surviving colonies with >50 cells/colony are counted, survival curves plotted after normalizing for the cytotoxicity induced by AuNS alone, and data are fitted to a linear-quadratic model. DEF was calculated as the ratio of the dose resulting in 10% survival with radiation alone to that resulting in 10% survival with radiation plus AuNS (normalized for AuNS cytotoxicity).

#### **Mechanistic studies**

Similar to uptake studies, cells are treated for 24 hrs according to assigned treatment group prior to RT. ROS production was evaluated using the ROS-Glo kit (G8820, Promega). DSB was evaluated by fixing cells and exposing them to anti- $\gamma$ -H2AX (Abcam ab11174) or anti-53BP1 (Abcam ab172580) primary antibodies after blocking with 5% BSA overnight at 4°C. They are then stained with secondary antibodies conjugated to Alexa Fluor 647 (Texas Red – ThermoFisher Scientific A32723) or Alexa Fluor 488 (FITC – ThermoFisher Scientific A31852) for 2 hours at room temperature, and lastly stained with DAPI (blue). Images are captured using a fluorescence microscope (Leica DMI6000B, Leica Microsystems, Wetzlar, Germany) and foci of immunofluorescence within the nuclei analyzed using SPOT software (Sterling Heights, MI, USA). At least 50 nuclei were counted per experimental condition. Comet assay is performed using the Trevigen CometAssay® reagent kit for single cell gel electrophoresis assay (Cat #

4250-050-0), and analyzed with the published OpenComet protocol and software.[129] Seahorse assay is carried out using the Agilent Seahorse XF Analysis set-up courtesy of the Taniguchi Lab at UT MD Anderson Cancer Center. Mitochondrial membrane potential is assessed using the TMRE Mitochondrial Membrane Potential Assay Kit from Abcam (ab113852).

## Chapter IV: *in vivo* biodistribution and therapeutic efficacy

### 4.1 Abstract

Tumor localization of targeted radiosensitizers provide a mechanism for safer and more effective cancer therapies. Moreover, the effects of their physiochemical properties on the *in vivo* fate of these particles can result in better targeted therapies. Here, we evaluate the *in vivo* distribution of the nanoparticles as a function of their surface chemistry. Mice bearing subcutaneous human pancreatic tumors receive intravenous (tail vein) injections of the nanoparticle formulations discussed in previous chapters (Figure 3.1). All particle formulations are sterically stable in physiological concentrations of salt. Histological evaluation of tissues with the highest uptake (liver and spleen), along with normal pancreas tissue show no appreciable changes relative to normal, untreated tissue. In line with the *in vitro* data, tumor growth delay studies reveal greatest radiosensitization effect with nuclear-targeted gold nanoparticles. Furthermore, we test the efficacy of gold nanoparticle delivery using thermosensitive liposomes to further enhance gold nanoparticle accumulation at the tumor. Combined liposomal delivery with hyperthermia treatment results in greater nanoparticle uptake at the core of the tumor, as well as improved tumor growth delay. These results suggest that targeted nanoparticles can provide greater intracellular delivery of therapeutic agents to the cancer cells within solid tumors than their non-targeted counterparts, and that enhanced tumor uptake can be achieved through liposomal delivery.

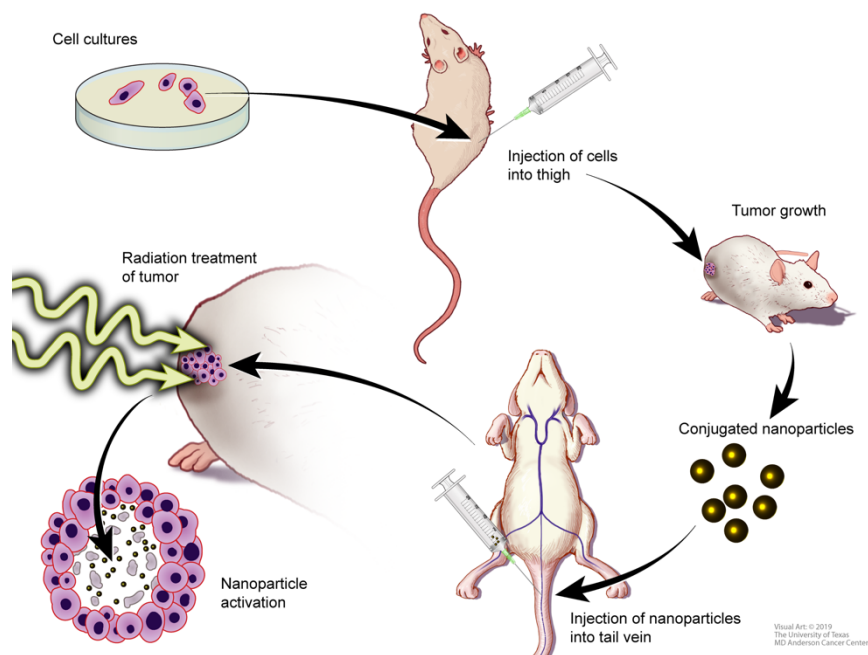


Figure 4.1: Graphical representation of chapter IV studies. Xenograft tumor models are established to study AuNS biodistribution with and without liposomes, and therapeutic efficacy.

## 4.2 Introduction

Medical applications of NPs depend on their ability to accumulate at a desired anatomical site regardless of administration route. Several biological barriers limit site-specific NP bioavailability, thereby hindering the ability to achieve therapeutic levels. These barriers include, but are not limited to, opsonization followed by mononuclear phagocyte sequestration, nonspecific biodistribution, blood flow limitations, pressure gradients, efflux pumps, clearance or storage in reticuloendothelial system (RES) organs, and escape from endosomal or lysosomal compartments.[1] Both passive accumulation via the enhanced permeability and retention (EPR) effect, and active targeting rely on surface functionality of nanoparticles to determine the biological distributions. The EPR effect established the increased accumulation of macromolecules via extravasation through fenestrations in blood vessels present in tumors.[2] However, the limitations of the EPR effect, such as unpredictable drug retention and heterogeneous vascular permeability, emphasize the need for active targeting through innovative design of decorated particles.[3]

The discovery of the enhanced permeability and retention (EPR) effect fundamentally transformed understanding of how therapeutic and contrast agents accumulated within the tumor microenvironment. This prompted the development of nanoparticle-based therapeutics in cancer treatment. While larger molecules diffuse randomly, nanomaterials can extravasate into tumors via leaky vasculature. However, the immature and leaky tumor vessels leads to heterogeneous vascular perfusion within tumors. The invasive periphery of the tumor typically contains the highest microvascular density while the tumor core is underperfused and thus, underexposed to intravenously delivered agents. In addition to the physiological barriers already imposed by the interstitial matrix (glycosaminoglycans, collagen, proteoglycans), the dense stromal component (desmoplasia) of pancreatic cancer further hinders the delivery of nutrients, oxygen and drugs. The consequent hostile microenvironment (low pH, low pO<sub>2</sub>) of the tumor core harbors the most aggressive tumor cells with the greatest potential to regenerate if they survive cytotoxic treatment.

We examine the passive cellular uptake and active nuclear targeting in Chapter II, and the *in vitro* effects of combined RT and AuNS treatment in Chapter III. Here, we investigate the *in vivo* radiosensitization potential of AuNSs in pancreatic cancer models, as well as the effect of active nuclear targeting combined with RT. Additionally, we develop an innovatively designed delivery system to penetrate the physio-chemical barriers of pancreatic cancer using thermosensitive liposomes (TSLs). TSLs accumulate passively in the tumor via the EPR effect, and upon an external trigger (hyperthermia), TSLs release their payload.



## 4.3 Results and discussion

### Biodistribution and *in vivo* toxicity studies

We perform *in vivo* biodistribution studies in immunodeficient nude mice harboring xenografts of Panc-1 and MiaPaCa-2 cells. 24 hours following intravenous administration of pAuNS, sAuNS or nAuNS, normal organs (brain, lung, heart, liver, spleen, kidney, intestine and muscle), tumors and blood were collected for quantitative analysis of gold content using ICP-MS (Figure 3.2). As expected, the liver and spleen contain the highest amounts of gold. AuNS accumulation in the tumor is relatively similar across the three conjugate groups, and slightly higher quantities of gold are present with the AuNS conjugate group than the non-targeted groups. Blood levels demonstrate that AuNSs remain in circulation, albeit at very low concentrations. Normal pancreas tissue contains minimal gold content. Of note, no appreciable changes in the behavior, body weight, appearance or food/water intake of mice was noted following AuNS administration.

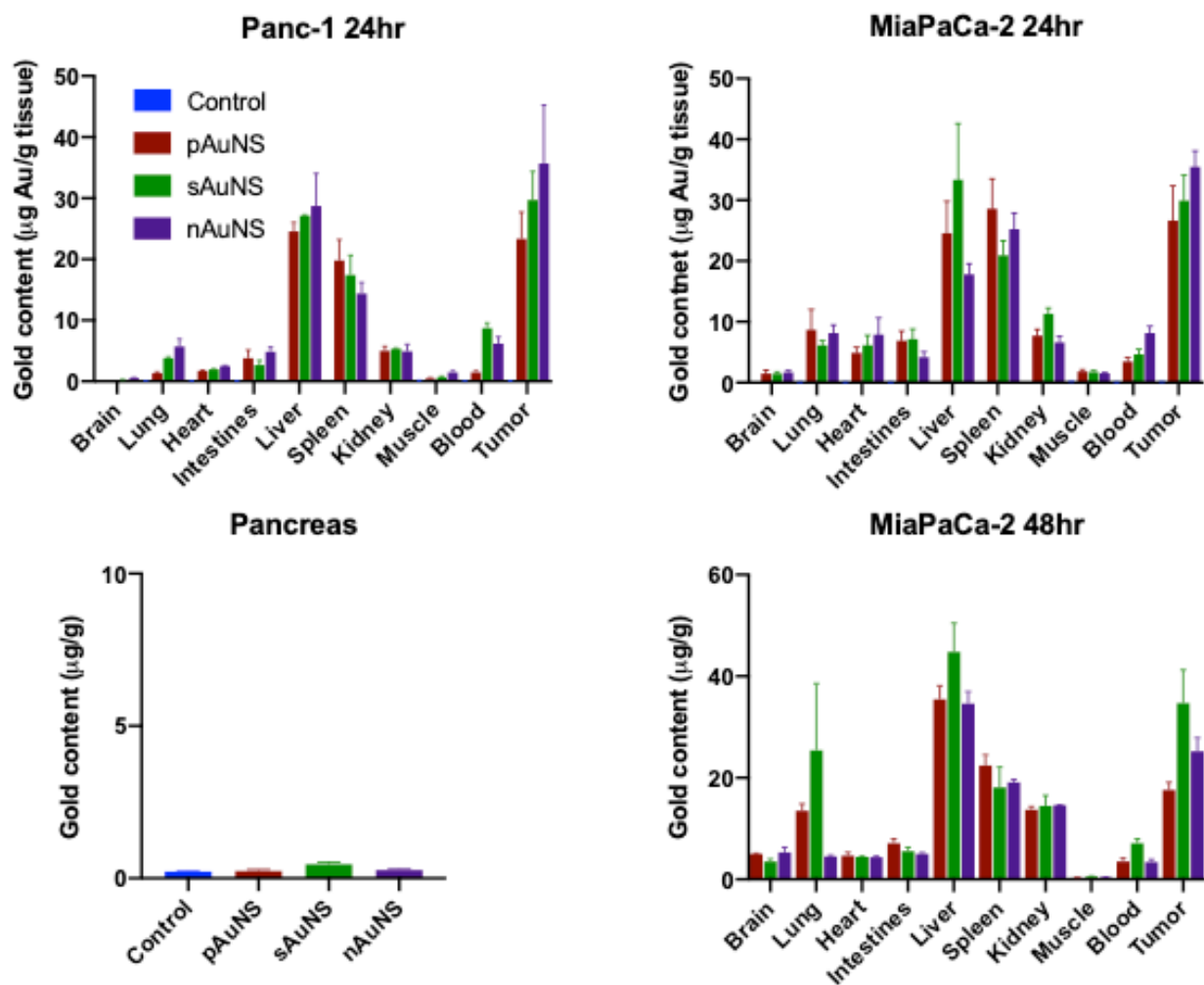


Figure 4.2: AuNS biodistribution studies. *In vivo* AuNS biodistribution 24 hours post particle administration in (A) Panc-1 cells and (B) MiaPaCa-2 tumor models. (C) Normal pancreas tissue uptake of AuNS. (D) AuNS biodistribution at 48 hours post particle administration.

Although mice with Panc-1 tumors received twice the concentration of AuNSs, the tumor gold content is similar for both tumors. This may reflect the heterogeneity in vascular and tumor microenvironment present between the two tumor types. Looking forward to liposomal studies, we evaluate the *in vivo* biodistribution of AuNSs in harboring MiaPaCa-2 tumors 48 hours following AuNS treatment. Similar to the earlier time point, the liver accumulation is high relative to other tissues. In fact, tumor uptake is slightly decreased from the 24 hour time point. However, this decrease did not affect the radiosensitization effect as we discuss in the next section. Interestingly, the quantity of gold decreases in the spleen at 48 hours while the kidney content increases. This perhaps reflects renal clearance of the AuNSs overtime. In addition to obtain tissues for qualitative assessment of toxicity.

RES organs (liver and spleen) demonstrate considerable AuNS uptake and clearance in spite of the small size, or particle surface functionalization by PEGylation or peptide conjugation. Analysis of hematoxylin and eosin stain of normal pancreas, tumor and tissues with the highest AuNS uptake (liver and spleen) qualitatively show no effect of AuNS treatment in mice. (Figure 3.3) Taking this a step further, we assess the effect AuNS exposure has on immune activation and coagulation in donor human blood samples. Complement activation assays reveal no difference in activation of the classical pathway, however, there is a differential effect with sAuNS treatment activating the mannose-lecithin pathway and nAuNS treatment activating the alternative pathway to a greater extent than other treatment groups ( $p < 0.01$ ). (Figure 3.3) Evaluation of clotting factors in human donor samples also demonstrate no effect of AuNS treatment on prothrombin time (PT), international normalized ratio (INR), partial thromboplastin time (PTT) and thrombin time (TT). Taken together, this results reinforce the biocompatibility of the AuNSs designed.

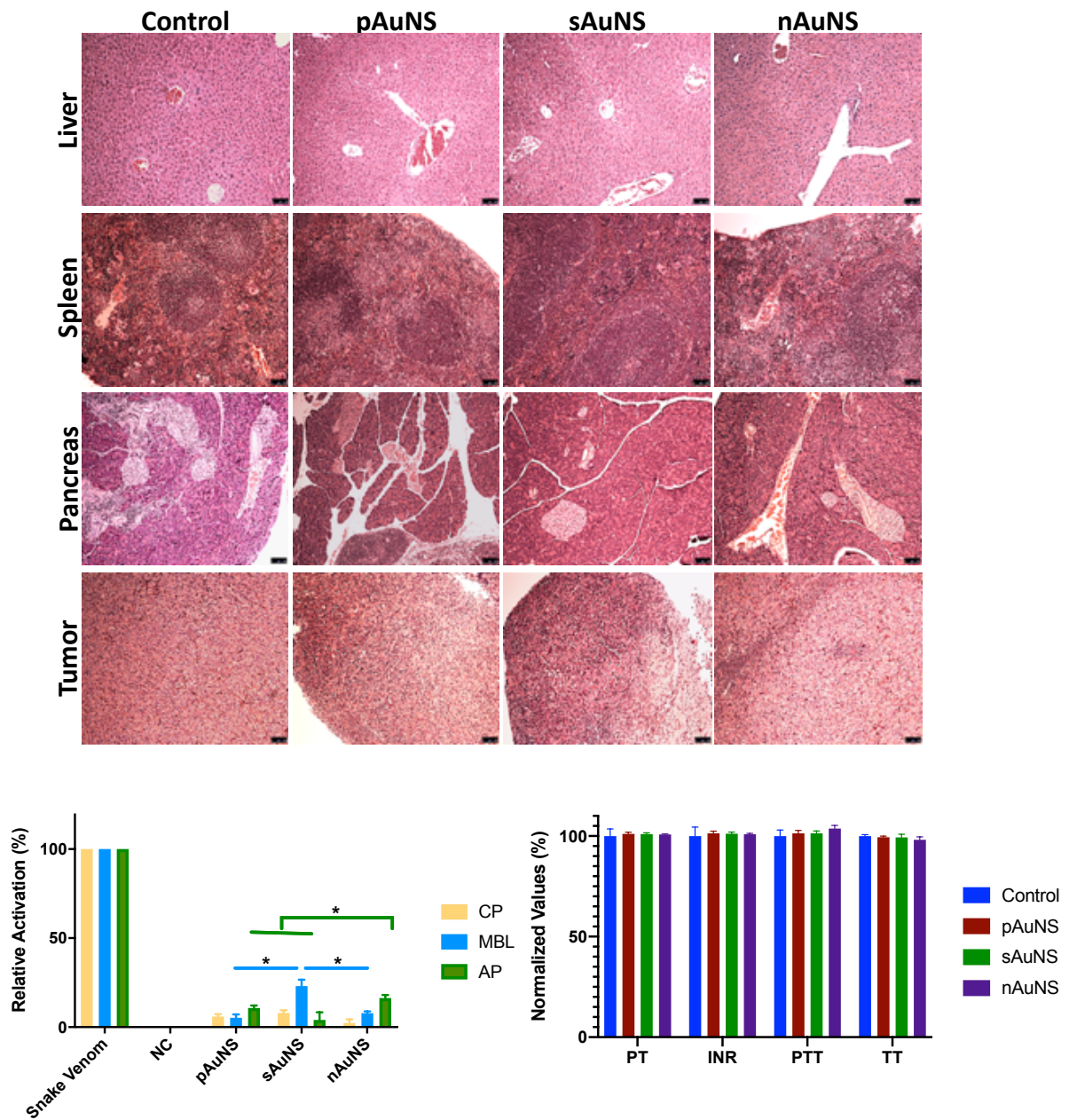


Figure 4.3: *In vivo* AuNS toxicity, (A) H&E stain of the liver, spleen, normal pancreas and tumor qualitatively indicate no difference in control and AuNS-treated groups. (B) Complement activation assays with donor human serum reveal non-statistically significant relative activation levels for the classical pathway, and a differential activation of the mannose-lecithin binding pathway for sAuNS and the alternative pathway for nAuNS. ((C) Measurements of PT, INR, PTT and TT in human blood donor samples reveal no effects of AuNS treatment.

## **Radiosensitization with AuNS**

We assess the therapeutic potential of AuNSs treatment in combination with RT using tumor growth delay (TGD) assays. Preliminary studies informed our decisions on the number of mice per group. For the Panc-1 xenograft models, we treat with a single dose of 6 Gy using 250 kVp orthovoltage x-rays 24 hrs after AuNS treatment (5  $\mu$ g/g) – Figure 3.4. We observe delayed tumor regrowth in the non-targeted pAuNS + RT group; this delay is even more pronounced for the nAuNS + RT group. It is noteworthy that half the mice in the nAuNS + RT group had complete tumor regression. This suggests a dose depended mechanism as determined by the split dose assau in chapter III. Moving forward, a single RT dose of 8 Gy is used for subsequent studies. Based on the biodistribution studies, we also included additional groups with a 48 hr delay between AuNS administration and RT in the MiaPaCa-2 tumor model.

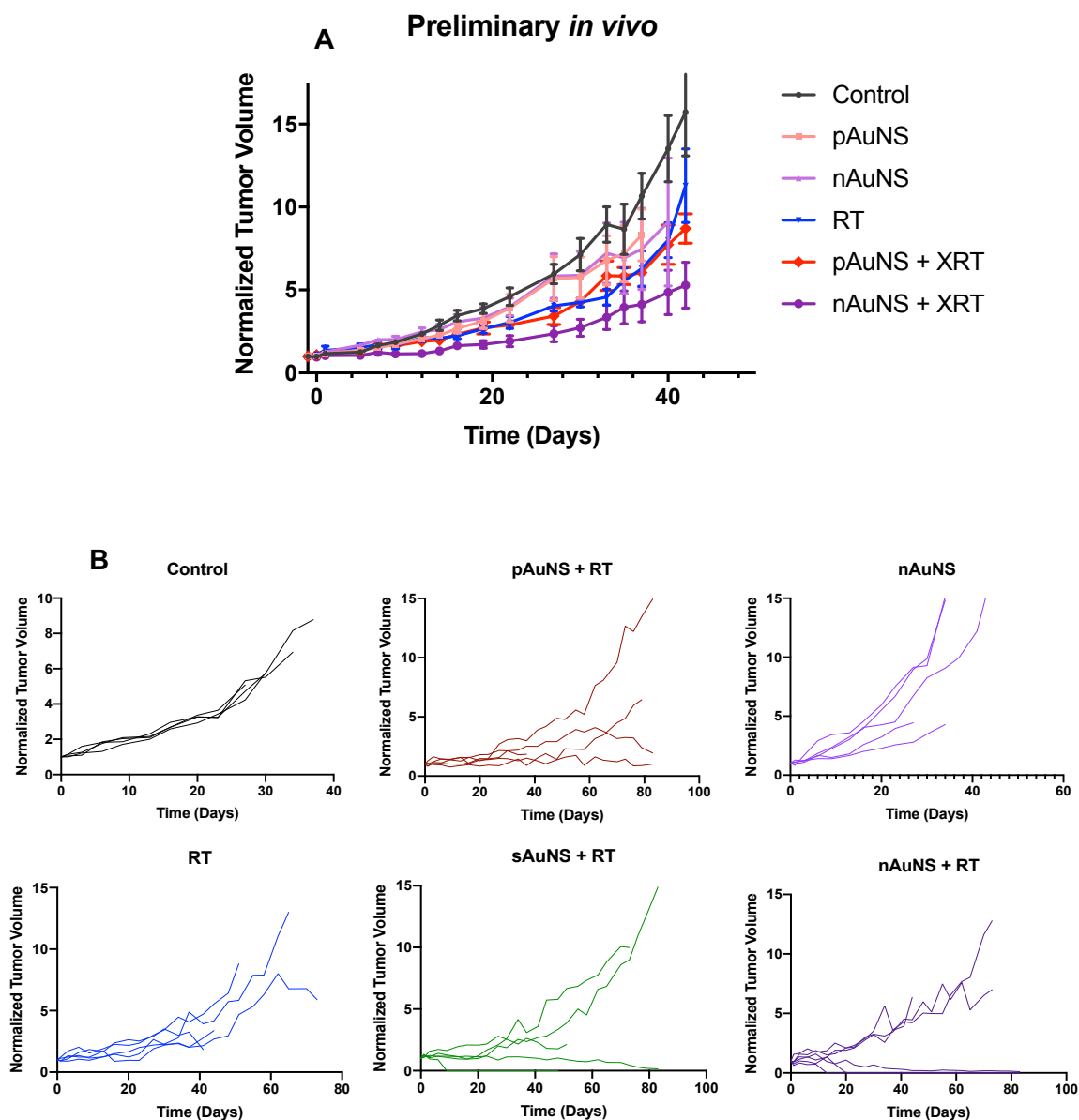


Figure 4.4: Panc-1 TDG studies. (A) Preliminary tumor growth delay to determine sample size for future experiments. (B) Individual tumor growth delay curves for each treatment group with statistically significant differences relative to the control group:  $p < 0.01$  for both pAuNS + RT and sAuNS + RT groups, and  $p < 0.0001$  for nAuNS + RT groups relative to RT only, and nAuNS only treatment group. Also,  $p < 0.0001$  for nAuNS + RT compared to pAuNS + RT and sAuNS + RT.

In the MiaPaCa-2 xenograft models, we use half the AuNS concentration based on *in vitro* studies and observe complete tumor regression in all mice for the nAuNS + RT treatment group when the sequencing interval is 24 hr, and all but one mouse when the sequencing interval is 48 hr. The tumor regrowth delay is significantly longer than that of the control, RT only, pAuNS + RT and sAuNS + RT groups ( $p < 0.0001$ ) (Figure 3.5). Survival curves demonstrate improved survival in the AuNS + RT treatment groups when compared to control or RT only treatment groups with  $p = 0.002$  and  $p < 0.0001$  by log-rank (Mantel-Cox) test, respectively.

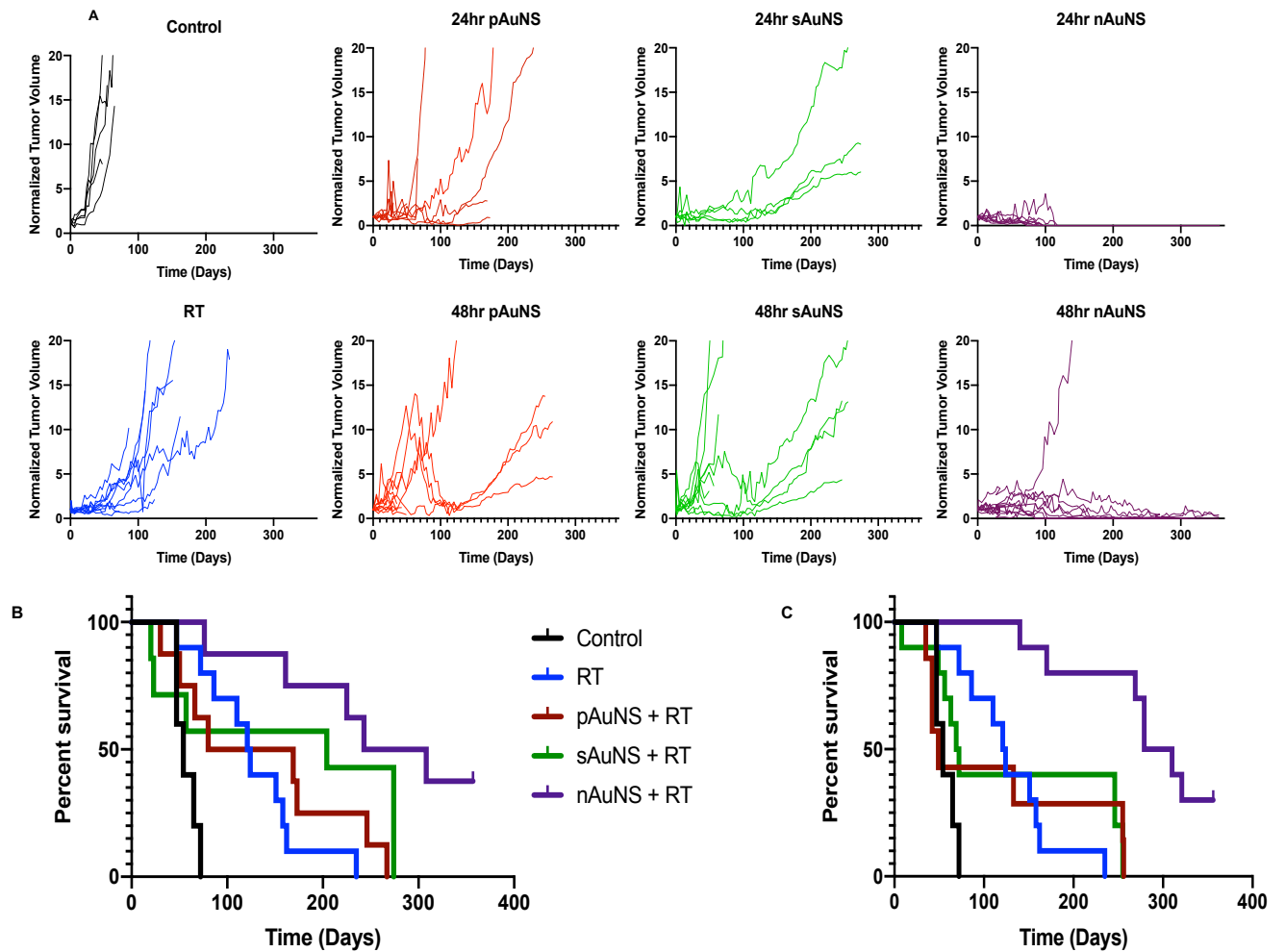


Figure 4.5: *In vivo* MiaPaCa-2 tumor growth delay and survival studies. (A) Individual normalized tumor volumes for each treatment group with statistically significant differences relative to the RT only group:  $p < 0.01$  for both pAuNS + RT and sAuNS + RT groups, and  $p < 0.0001$  for nAuNS + RT groups relative to RT only. Also,  $p < 0.0001$  for nAuNS + RT compared to pAuNS + RT and sAuNS + RT. Kaplan-Meier survival curves of mice when RT was given 24 hrs (B) and 48 hrs (C) after AuNS administration. In both figures, AuNS + RT treatment resulted in statistically significantly better survival than control or RT only groups with  $p = 0.002$  and  $p < 0.0001$  by log-rank (Mantel-Cox) test, respectively.



## **Liposomal design and kinetics**

Untargeted particle use for radiosensitization generally requires large intratumoural accumulation of gold to achieve the desired effect. We are able to achieve local tumor control with nuclear-targeted AuNPs as demonstrated in the previous section. To further maximize the uptake of AuNSs in the tumour, especially at the under-perfused tumour core, we encapsulate the AuNSs in liposomes. Liposomes are an archetypal nanoparticle system that are a cornerstone for modern drug delivery initially discovered in the 1960's.[130] Liposomes are spherical structures made up a phospholipid bilayer membrane capable of encapsulating hydrophobic or hydrophobic agents. Liposomes are desirable vesicles for delivery because they are inert and weakly immunogenic. We utilize a design strategy to encapsulate the AuNSs in liposomes that are triggered by hyperthermia (HT) to release the AuNSs once in the tumor microenvironment. The liposomes are characterized similarly to the AuNSs in Chapter II (Figure 3.6). The liposome design process is illustrated in the supporting information, and characterization described here.

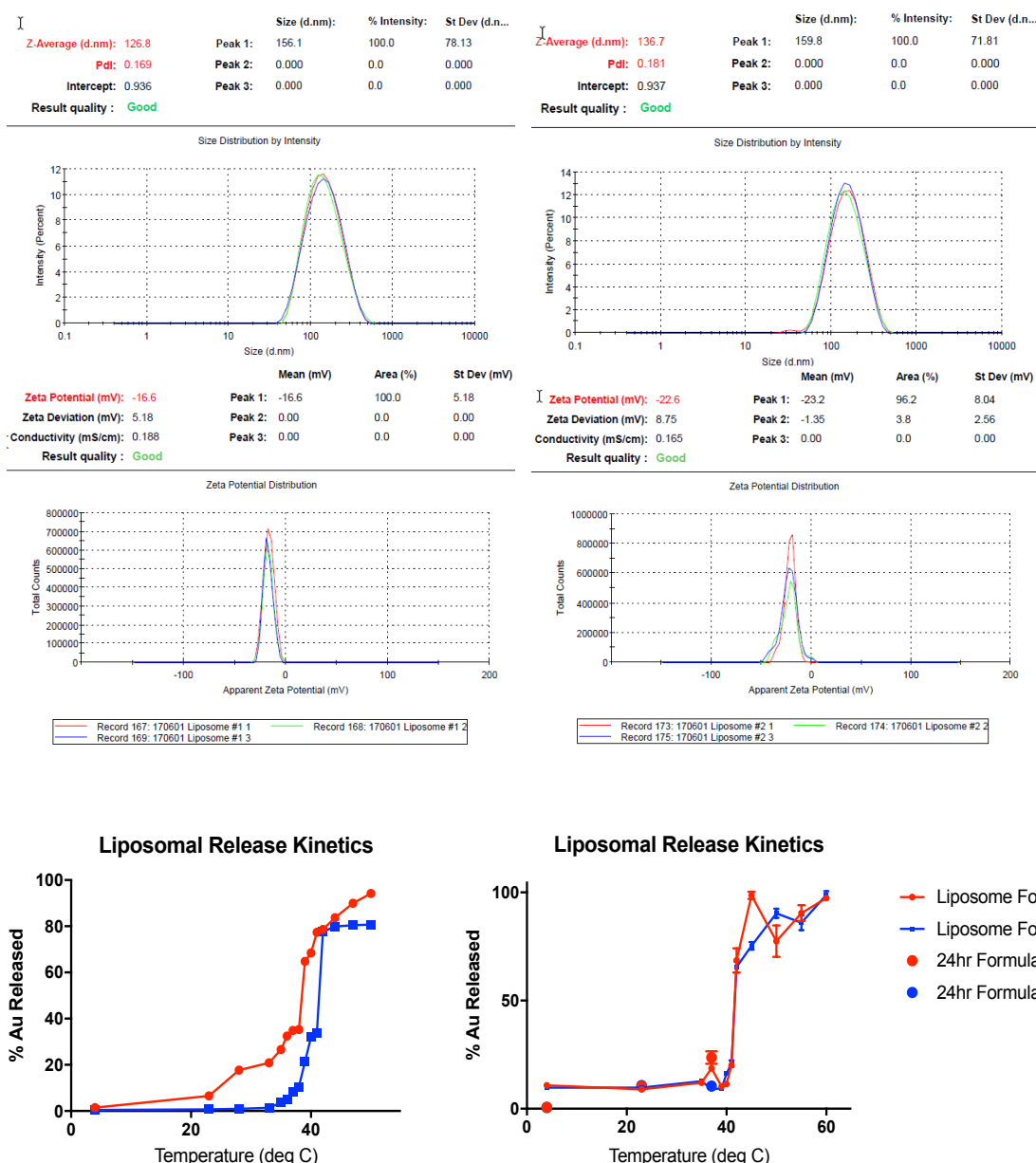


Figure 4.6: TSL characterization and release kinetics. (A) DLS and (B) zeta potential measurements for the 2 liposomal formulations, revealing similar sizes and negative surface charge as expected. (C) Release kinetics highlighting release of AuNSs from TSLs following exposure to a specific temperature range (40 – 42°C). For each time point, samples are tested in triplicate.

## **Biodistribution with liposomes**

The bigger size of liposomes relative to the AuNSs allows for encapsulation of a large number of nanospheres within the bilayer or the cavity, and PEGylation ensures stability and longer circulation times. A 2010 study found higher levels of gold internalization when smaller AuNPs, 1.4 nm in diameter, were delivered via liposomes.[131] We hypothesize that externally triggered release of the AuNSs from the liposomes using hyperthermia (HT) results in deep tumor penetration by the AuNSs. We assess the gold content using biodistribution studies in xenografts established with both Panc-1 (at 4 hours post treatment) and MiaPaCa-2 (at 24 hours post treatment) cells (Figure 4.7). These studies reveal much higher uptake of liposomes by the liver, consistent with the observation that larger nanoparticles are hepatically cleared. Additionally, tumors appear hyperemic following HT treatment for 5 min. Tumors are sectioned to obtain tissues from the core and periphery. Gold content reveals similar levels of gold in the periphery sections, while HT treatment increases gold quantified in the tumor core. This difference is not statistically significantly different between the nAuNS + HT vs nLipo + HT groups.

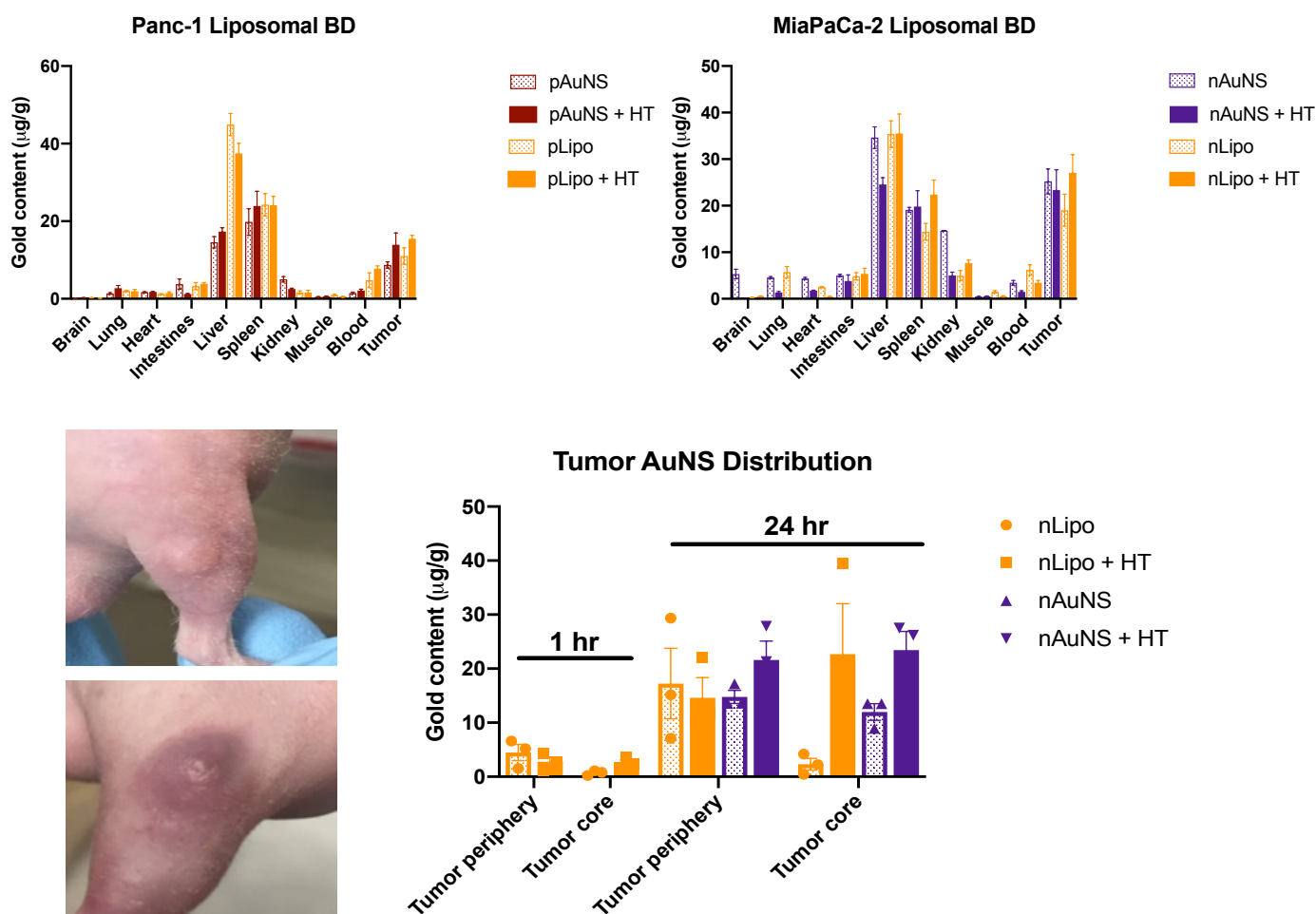


Figure 4.7: TSL biodistribution. Biodistribution assessing gold content in (A) PANC-1 and (B) MiaPaCa-2 xenograft tumor models. (C) Comparison of subcutaneous tumor with and without HT treatment at 42°C for 5min. (D) Tumor distribution of gold content at 1 hr and 24 hrs after nanoparticle infusion.

## **Radiosensitization with liposomes**

Several studies and clinical trials demonstrate the utility of HT in cancer treatment. (5, 8) As such we expect improved tumor growth delay and survival in the group treated with combination HT + RT + AuNSs relative to those treated with a singular or double agent treatment. As expected, combination of nAuNS and RT results in complete tumor regression in a majority of the mice in the nAuNS + RT and nAuNS + HT + RT groups. This observation is independent of HT treatment. Furthermore, nLipo + HT + RT treatment also results in complete tumor regression. Notably, nLipo + HT + RT results in an improved therapeutic effect compared to HT alone or HT + RT. This implies that the presence of AuNSs, even when encapsulated in liposomes, still results in radiosensitization and improved local tumor control. This effect is more pronounced when AuNS is released from the liposomes, but present, nonetheless.

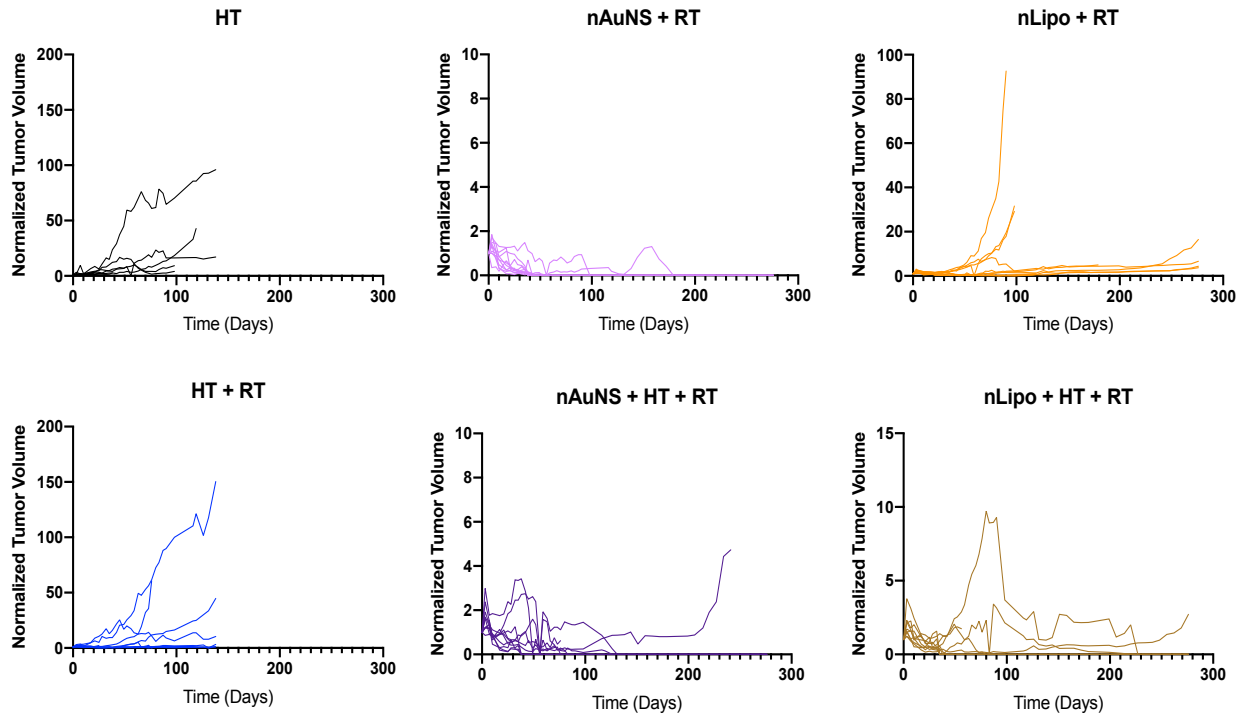


Figure 4.8: *In vivo* tumor growth delay with TSLs. Individual normalized tumor volumes for each treatment group with statistically significant differences relative to the HT only group:  $p < 0.0001$  for both nAuNS + RT and nAuNS + HT + RT groups, and  $p < 0.0001$  for nAuNS + RT groups relative to HT + RT only. Also,  $p < 0.001$  for nAuNS + RT compared to nLipo + HT + RT. There is no statistically significant difference among nAuNS + RT, nAuNS + HT + RT and nLipo + HT + RT groups.

## 4.4 Conclusion

In order to successfully amass in the desired biological target, NPs must remain in circulation in concentrations high enough to localize in the tumours. We demonstrate that the AuNSs designed here accumulate in the tumour without cell-specific receptor targeting. Moreover, toxicity studies reveal no measurable adverse effects of AuNS in the tissues examined. These results affirm the potential use of the AuNSs to enhance RT effects in the tumour while simultaneously minimizing the toxicity to normal tissues. Similar to the split dose assay in Chapter III, non-curative doses of radiation combined with nAuNS *in vivo* resulted in complete tumor regression in >90% tumors. Comparable *in vivo* radiosensitization effects in two independent tumor xenograft models suggests that passive targeting may be sufficient for tumor uptake. Indeed, active targeting has not shown demonstrably larger accumulation of nanoparticles in tumors.[132] However, passive targeting relies on the enhanced permeability and retention effect that tends to be heterogeneous, especially for larger tumors and tumors exhibiting differing levels of vascularity.[133, 134]

Despite the proven clinical utility of the EPR effect, there are several limitations due to the difficulty to control the tumour uptake which can ultimately contribute to multiple drug resistance. (107) Liposomes loaded with drug cargo were first reported in 1973, however, the *in vivo* delivery efficiency was hampered by interactions by macrophages and serum complement compounds which caused premature drug release in the blood.[135, 136] This incited the design of liposomes with longer circulation times and reduced toxicity.[137, 138] Consequently, several liposome-encapsulated drugs received FDA approval, such as doxorubicin (Doxil) in 1995 for treatment of Kaposi's sarcoma and albumin-bound paclitaxel (Abraxane) in 2005 for metastatic breast cancer.[139, 140] These formulations have since received approval for treatment of several ailments, and continue to be investigated along with other drugs for additional clinical applications.[141] Effective liposomal-based therapy requires encapsulation of the relevant drug, avoidance of the mononuclear phagocyte system, accumulation at the desired target and

important, effective release of high enough levels of the payload to cause a therapeutic effect.[142]

Once liposomes accumulate in the tumour, drug is released passively over long-periods of time or following natural degradation of the lipid bilayer. This passive release, however, can result in sub-optimal release kinetics causing diminished therapeutic gains.[143-146] Therefore, studies explored development of liposomal delivery systems capable of releasing the payload in following a specific stimulus. This triggered release mechanism optimizes time, location and drug concentration kinetics at the target site. Several groups looked into stimuli-responsive liposomal formulations such as temperature, pH, ultrasound or photo-sensitivity triggers for release.[141, 147-150] Temperature, or thermos-, sensitive liposomes are closest to clinical application with several clinical trials.[150, 151] We employ TSLs combined with HT to enhance AuNS uptake at the tumour core, thus improved radiosensitization. Mild HT triggers the release of the AuNSs locally in the tumour microenvironment, enabling the small AuNSs to escape clearance in the blood stream. Once in the TME, tumour cells can internalize the AuNSs and allow for nuclear uptake for the targeted particles.

Besides, HT has been used therapeutically for many years, even with radiation and chemotherapy in cancer treatment.[152] HT treatment results in increased vascular permeability and blood flow to the tumour, features desirable in drug delivery. Additionally, HT can improve drug accumulation to hypoxic regions of tumour which are normally resistant to therapy due to the low perfusion by increasing blood flow and drug plus oxygen delivery. Regional HT is particularly important here for the liposomes and combined RT treatment because it results in increased AuNS accumulation and release in the target tumour periphery and core, thereby enhancing the therapeutic index. This enables greater local tumor control while reducing the potential off-target effects, the overall aim of this thesis.



## 4.5 Supporting information

- Tumor volume calculations based upon caliper measurements of long and short axis tumor dimensions

$$Tumor\ volume = \frac{width^2 * length}{2}$$

- Liposome synthesis employing a thin film hydration method. AuNSs in PBS are added to the lipids to form multilamellar liposomes. The particles are then extruded multiple times through variety of filters to obtain the desired size.

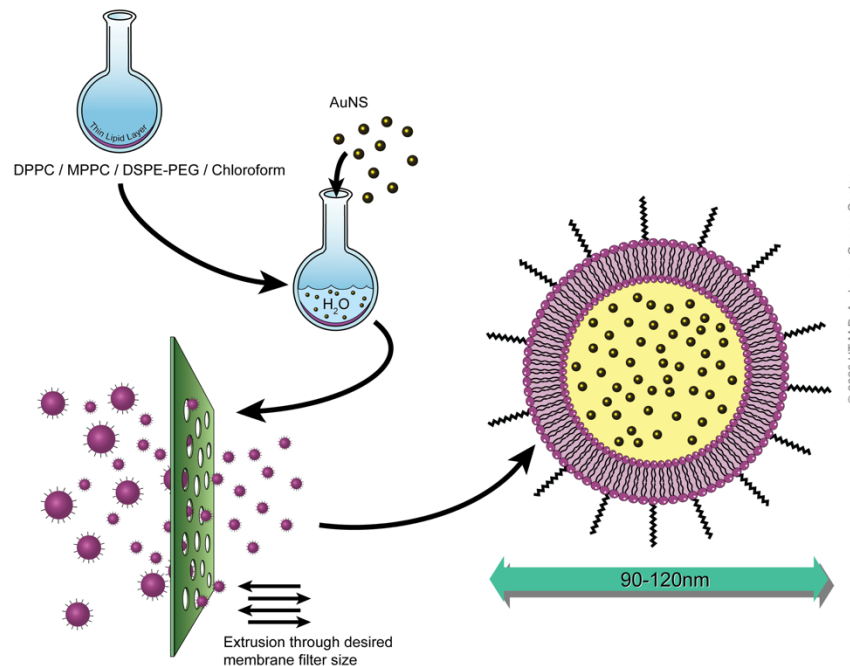


Figure 4.9: TSL synthesis schematic. Aqueous AuNS solution is added to thin film of lipids and heated to create an emulsion to allow multilamellar liposome formation. This emulsion is then allowed to cool down and extruded to obtain desired size of liposomes.

## **4.6 Materials and methods**

### **Biodistribution**

Male athymic Swiss nu/nu mice 6-8 weeks old are purchased, maintained, and handled using protocols approved by Institutional Animal Care and Use Committee (IACUC) at M.D. Anderson Cancer Center. Subcutaneous xenografts are generated by injection of  $1-2 \times 10^6$  Panc-1 or MiaPaCa-2 cells into the right thighs of mice. When tumors grow to ~7mm in diameter, they are administered intravenous AuNS (5  $\mu\text{g/g}$ ) while anesthetized using isoflurane. Twenty-four hrs later, mice are euthanized and the blood, tumor, and normal organs are harvested, stored in pre-weighed glass vials and frozen at  $-80^\circ\text{C}$  until further processing. Frozen samples are lyophilized for 2-7 days to ensure complete dehydration of tissues before dry weights are measured. Afterwards, 1 mL of aqua regia is added to each vial for digestion of tissues with slight heating for denser tissues like liver. 1% nitric acid solution is added to digested samples to bring the final volume to 10 mL for each sample. This solution is filtered through a  $0.25 \mu\text{m}$  microfilter prior to ICP-MS analysis with standards measured in parallel. The amount of gold per unit dry weight of tissues was calculated.

### **Tumor growth delay**

Subcutaneous pancreatic cancer xenografts of both cell lines (as noted above) are used to assess tumor growth delay. Mice are randomly assigned to treatment groups of RT alone, AuNS alone, RT + AuNS or no treatment. Animals treated with combination therapy receive intravenous administration of 100  $\mu\text{L}$  of 10 OD (optical density) of AuNS 24 hrs prior to RT. Control mice and those receiving RT alone receive 100  $\mu\text{L}$  of PBS. RT is administered using an orthovoltage unit (Philips RT-250, 250 kVp beam with a Cu-filter) equipped with a cone applicator to focus radiation toward the tumor target while the mice are anesthetized with an intraperitoneal injection of 100  $\mu\text{L}$  of 5% ketamine and 10% xylazine in PBS. Tumors are measured 2-3 times a week using digital calipers and tumor volumes were calculated as  $\frac{1}{2} \times (\text{long axis diameter}) \times (\text{short axis diameter})^2$ . Tumor volumes are normalized to the initial tumor volume for each mouse,

averaged across groups and plotted over time. Animals are euthanized when tumor diameter in one dimension exceeded 2 cm, or animals lost greater than 20% body weight, were unable to feed by themselves, or survived past 365 days.

### **TSL design and synthesis**

The thermosensitive liposomes are formulated by a lipid mixture of dipalmitoyl phosphatidylcholine (DPPC), 1-myristoyl-2-palmitoyl phosphatidylcholine (MPPC), and distearoyl phosphatidyl-ethanolamine-polyethylene glycol 2000 (DSPE-PEG-2000) in a molar ratio of 90:10:4 employing a thin film hydration method [27]. 1ml PBS containing 5-nm AuNSs is used to hydrate the thin film of lipids at a transition temperature of 65°C for 1 hr to allow the transfer of AuNSs to the core aqueous region of the liposome. The suspended TSLs are extruded through 400 nm, 200 nm then 100 nm pore filter membranes. Free AuNSs are removed using 1000 kDa molecular weight cut-off vivaspin tubes.

## Chapter V: Summary and conclusion

### 5.1 Significance

Rapid developments in the field of cancer nanotechnology have facilitated the creation of numerous types of nanoparticles with varying sizes, shapes and targeting properties. This has fueled the pursuit of meaningful clinical applications for cancer therapy while simultaneously minimizing toxicities to normal tissues. These studies report the enhancement of the therapeutic effects of RT in pancreatic tumor cells when used in conjunction with sub-cellularly targeted AuNPs. The combination of nanoparticle localization and the targeted delivery of radiation both augment the radiation effects on the tumor, and reduce the side effects to normal cells. Although these studies are performed in the context of pancreatic cancer, these particles can be used in other solid tumors as they are not purposely targeted to a cell-specific receptor.

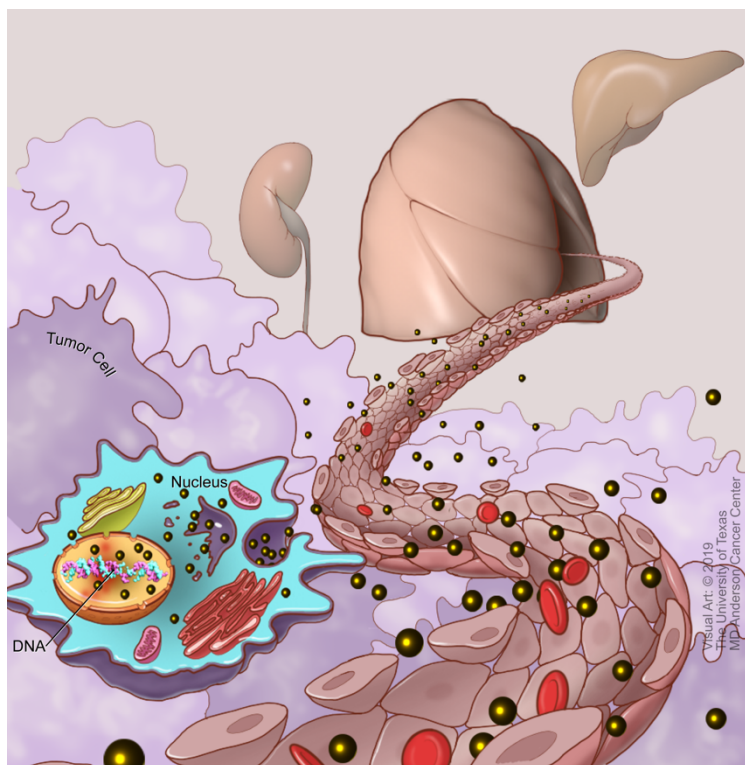


Figure 5: Chapter V graphical summary. Nuclear-targeted gold nanoparticles presented here achieve their therapeutic potential primarily due to their proximity to cancer cell DNA.

## 5.2 Summary

Cancer is the second leading of mortality in the US. Pancreatic cancer (PC), specifically, is the third leading cause of cancer deaths and predicted to become the second by 2025.[1, 153] Also referred to as pancreatic ductal adenocarcinoma (PDAC), PC is one the most aggressive malignancies with 5-year survival rates of less than 10%. Poor prognosis is attributed to the complicated and multifactorial nature of the disease with limited treatment options. Surgical resection presents the only real chance for a cure, unfortunately, roughly 15 – 20% of individuals present with resectable disease and long-term survival still low in these cases.[154, 155] An autopsy series highlighted the need for localized therapy by noting 30% of all pancreatic patients die from locally destructive disease regardless of clinical stage at presentation, treatment history or histopathological features.[33] Radiation (RT) offers one of the few truly localized clinical treatments, but curative doses are not clinically achievable due to the toxicities to healthy surrounding tissues. Therefore, innovative RT strategies become promising options in combination with targeted nanotechnology to combat pancreatic cancer in a directed manner.

The ***overarching goal*** of this thesis is to radiosensitize pancreatic cancers by designing nuclear-targeted gold nanoparticles packed into thermally activated liposomes that release their payload upon external stimulation. Radioresistance is a major mechanism of tumor progression that has previously hindered progress in the treatment of aggressive cancers. [1-9] Delivering higher doses of radiation to the gross tumor to overcome radiation resistance has historically been challenging due to the limited radiation tolerance of the surrounding organs. Sequestering gold nanoparticles (AuNPs) within tumors to amplify radiation-induced secondary electron showers has been investigated as a means to escalate radiation dose in the vicinity of the nanoparticle at micron/nanometer ranges, thus confining the higher dose to the tumor and sparing surrounding tissues.[10-39] Maximizing this radiosensitization requires (i) deep penetration of these nanoparticles inside tumors at the tissue level, and (ii) accumulation near or

within the nucleus at the cellular level – both of which still remain major challenges. This work surmounts these challenges by enhancing accumulation of gold deep within the radioresistant core using thermosensitive liposomes to deliver nuclear-targeted gold nanoparticles.

A fundamental objective for drug delivery is targeted release of a drug at a desired rate and concentration. Nanoparticles are of particular interest because they can selectively accumulate at a desired site, either through the EPR effect or active targeting. Factors that play a role in the clearance and accumulation of NPs include size, shape, charge and functionalization status. Several groups have investigated the effects of NP size on biodistribution and found that size determines clearance of NPs from the blood stream with NPs > 5 nm excreted via renal clearance while particles > 100 nm are cleared through spleen and liver sequestration.[156-158] NPs with sizes falling in the range of 5 – 100 nm showed increased circulation times, and therefore, systemic clearance and tissue accumulation for these particles is dependent on additional factors such as shape and surface chemistry.[159, 160] NP shape determines *in vivo* fate by affecting the circulation, margination ability and binding affinity in favor of non-spherical NPs.[161, 162] Active targeting through functionalization of NPs with targeting moieties further underscores the versatility of NPs in their potential applications. NPs decorated with peptides or antibodies are readily taken up by cells via receptor-mediated endocytosis, accumulating within endosomal vesicles. Targeted NPs can also be functionalized for sub-cellular targeting to enable more specific compartmentalization.[163, 164]

Irradiation of tumours laden with high atomic number (Z) materials such as gold results in radiation dose enhancement via increased secondary electron production from nanoparticle-radiation interactions.[75, 115, 116] The augmented density of ionization localized near or at the surface of the AuNPs leads to enhanced probability of lethal damage to cells containing the materials by transiently increasing the radiation-interaction cross section in the target tissue. A seminal study 40 years ago demonstrated the radiosensitization potential of iodine in cultured

cells.[117] This was later validated *in vivo* when injection of iodine into tumors followed by radiation resulted in roughly 80% suppression of tumor growth in mouse models.[118] Gold has been pursued as a radiosensitizer given its higher Z than iodine (Au, Z = 70 vs. I, Z = 53) and biocompatibility.[75]

Studies investigating the concentrations of high Z materials with radiation found that in order to achieve radiosensitization, higher concentrations of iodine and gold (~5mg/g) were required.[75, 119] When the gold nanoparticles (AuNPs) were internalized *in vitro*, however, radiosensitization effects were observed at concentrations as low as  $10^{-6}$  mg/g.[115] These results are consistent with previously published work demonstrating *in vitro* sensitization with AuNP concentrations of  $\sim 10^{-3}$  mg/g at both kilovoltage (kV) and megavoltage (MV) energies of radiation.[120] Based on these observations, it is possible to achieve radiosensitization effects at considerably lower concentrations, given intra-cellular or sub-cellular accumulation of AuNPs.

In this thesis, nuclear localization of gold nanoparticles via surface decoration with NLS peptides potently increases radiosensitization in pancreatic cancer models *in vitro* via an increase in oxidative stress and DNA damage. Importantly, these findings were reproduced *in vivo* when nAuNSs were systemically administered at concentrations (5 mg/Kg) that are readily achievable in a clinical setting. To date, efficient drug delivery via active targeting of AuNSs to cancer cells has usually terminated with cellular internalization rather than with nuclear localization, despite the nucleus housing DNA, the critical driver of radiation damage to cells. Furthermore, given the very short latency and limited spatial diffusion capability of in-situ radiation-triggered ROS, localizing AuNSs in close proximity to DNA is a desirable attribute of such drug delivery strategies. Nonetheless, to our knowledge, most prior work with NLS decoration has been performed *in vitro* and not *in vivo* making the therapeutic efficacy seen in our study especially noteworthy.[165] We surmise that this is partly because, unlike gene therapy that requires nuclear access of the delivered construct, complete nuclear uptake of AuNSs is not

required for radiosensitization; even cytoplasmic accumulation increases radiosensitization while nuclear uptake enhanced this even further. This transmembrane transport of our AuNSs is aided significantly, however, by their small size (~5 nm) that allows faster diffusion through the nuclear pore complex comprised of dynamically fluctuating phenylalanine-glycine nucleoporins and their decoration with NLS that binds the importin  $\alpha$  subunit of the importin  $\alpha$ - $\beta$  heterodimer that shuttles cargo through the nuclear pore complex.[166, 167] It is noteworthy that TAT-peptide derived NLS also serves as an aid to cell membrane penetration.[168] It is likely that greater endosomal escape (possibly via the proton sponge effect of custom peptides) or use of other cell penetrating peptides may further increase nuclear accumulation for even greater radiosensitization.

Nonetheless, the complete eradication of tumors in the nAuNS + RT group, further confirmed in the liposomal HT groups, in a majority of mice over a very long follow-up period speak to the robustness of this approach, and the potential for advancement of this strategy to the clinic where other gold nanoparticle formulations have so far been unsuccessful. These results extend the large body of literature confirming that loading tumors with high atomic number (Z) materials such as gold results in radiation dose enhancement via increased secondary electron production.[75, 115, 116] A higher density of ionization localized near or at the surface of the high-Z element accounts for the large interaction cross-section and sequestering the high-Z element in the nucleus can spatially confine the ionization closer to DNA, the predominant target of radiation injury.

The successful application of nanoparticles in biomedical applications depends upon selective accumulation at the site of interest and the ability to overcome biological barriers. Ongoing research is required to elucidate the correlation between nanoparticle physiochemical features and the pharmacological/biological kinetics. Specific to this thesis, additional studies with orthotopic tumor models, clinically adaptation of AuNS treatment, and hyperthermia delivery. For example, we intended to utilize high intensity focused ultrasound (HIFU) to deliver HT



treatment since future clinical application would greatly benefit from localized treatment at the tumor. The superficial xenograft tumor models here are amenable to the method used, but deep-seated tumors would require a non-invasive and targeted form of delivery such as HIFU or MRI-guided FUS. Perhaps in this case, we can better demonstrate the additive or synergistic effect of combining HT-triggered release of radiosensitizing AuNSs with radiation. Ultimately, optimal clinical utility of HT in the setting of nanoparticle-mediated radiosensitization will require definition of different techniques that successful in different clinical scenarios in order to integrate HT into clinical practice.

In summary, radiation combined with nuclear-targeted gold nanoparticles radiation delivered with or without liposomes are proven to improve the effects of radiotherapy in a single dose setting for pancreatic xenograft models. Given that these nanoparticles are not targeted to a specific tumor type, this system could be envisaged as a turn-class key technique for local enhancement of effects of radiation therapy. Furthermore, these AuNSs or liposomes could be dually targeted with a tumor specific marker or delivered as a therapeutic in a targeted manner. Moreover, there is a differential uptake in normal tissues because uptake is dependent on abnormalities in the tumor microvasculature. These combined treatments could be utilized to deliver a higher dose to enhance tumor control. In the case of adequate tumor control, this method can serve to decrease the total dose of radiation delivered, which could alleviate normal tissue toxicity that usually limit treatment. Lastly, given that the effects are dose dependent, this mechanism would perhaps benefit from the high-precision stereotactic radiation treatments increasingly implemented in clinic for the treatment of patients. The multidisciplinary nature of this concept requiring collaboration in scientific disciplines such as chemistry, nanotechnology, pharmacology, bioengineering, imaging and radiation physics, and tumor and radiation biology underscores the potential to advance radiation therapy.

## **Appendix: Common methods**

### **Nanoparticle synthesis and conjugation**

#### **AuNS synthesis**

Gold nanospheres (AuNSs) were synthesized using a bottom-up approach through reduction of hydrogen tetrachloroauric acid ( $\text{HAuCl}_4$  – MW 339.785 g/mol) with sodium borohydride ( $\text{NaBH}_4$  – MW 37.83 g/mol) through a modified protocol used by Martin et al.[113] Upon addition of the  $\text{HAuCl}_4$ , the solution turned a bright orange color as a quick measure of the size of nanoparticles formed. Some of the solution was removed for characterization of newly formed AuNSs prior to conjugation procedures.

#### **AuNS conjugation**

Methoxy-polyethylene glycol 2000 thiol (mPEG-2K-SH) and bifunctional thiol polyethylene glycol 2000-N-hydroxysuccinimide ( $\text{NH}_2$ -PEG-2K-SH) were purchased from NanoCS and stored at  $-20^\circ\text{C}$ . PEG solutions were added to AuNS solutions at  $4^\circ\text{C}$  and the reactions allowed to occur for 24 – 48 hours. Following PEGylation, AuNSs were centrifuged for 30 minutes at 3500xg through 100 kDa filters in order to concentrate the nanoparticles and remove unbound reactants. Non-targeted AuNSs groups consisted of particles with the monofunctional mPEG for the pegylated group (pAuNS), and the bifunctional amine-PEG-thiol which was further conjugated to a peptide of similar molecular weight to the nuclear localization sequence peptide used for targeting (sAuNS). The peptide conjugation was accomplished using carbodiimide crosslinker chemistry with EDC (1-Ethyl-3-[3-dimethylaminopropyl]carbodiimide) and sulfo-NHS (*N*-hydroxysuccinimide) to attached the primary amine on the bifunctional PEG molecule to the carboxylic acid ( $-\text{COOH}$ ) group on the peptides. Each peptide had a singular  $-\text{COOH}$  group, ensuring a directional conjugation. Nuclear-targeting was achieved via conjugation of an HIV-Tat 1 derived peptide (Sigma-Aldrich) for the nAuNS group. Final AuNS construct

solutions were rinsed with PBS and further centrifuged for additional purification and concentration, then characterized as described below and stored at 4°C until use.

### **Peptide quantification**

To further assess successful conjugation of the peptides to the AuNSs, the amount of protein on the surface of the AuNSs was estimated using a colorimetric assay. Briefly, samples of bare AuNSs, pAuNS, sAuNS and nAuNS with equal absorbance at 562 nm in a UV-clear bottom 96-well plate (Corning 3635) were reacted with bicinchoninic acid (ThermoFisher MicroBCA Protein Assay Kit 23235) for 2 hours at 37 then read at 562 nm using a spectrophotometer (BioTek Cytation 5). The differences observed in 562 nm absorbances in the groups, specifically for the sAuNS and nAuNS groups, was assumed to result from the presence of peptides present at the surface of the AuNS.

### **Characterization**

#### **Absorbance**

Surface plasmon resonance creates an extinction spectrum dependent on the size, shape and aggregation status of AuNPs. Several factors such as surface charge (6), inter-particle distance (7, 8), chemical interactions at the particle surface (5), and medium dielectric properties (2-4) affect the position of the plasmon resonance. Therefore, Ultraviolet-visible (UV-vis) spectroscopy provides fast and real-time monitoring of the AuNPs during synthesis because it provides information on nanoparticle size, aggregation and concentration. (Amendola ns Meneghetti, J Phys Chem 2009) In present work, UV-vis spectra were obtained and recorded using a Cary 100 Bio UV-Vis spectrometer to obtain extinction spectra on AuNSs using a 1 cm path length quartz cuvette and AuNP solutions diluted roughly 5-10 times the stock solution in Milli-Q water.

## **Particle size and surface charge**

One of the few methods used for determining the size of nanoparticles in solution is dynamic light scattering (DLS) by measuring the hydrodynamic size. In this technique, a monochromatic laser illuminates the nanoparticle solution, and a photon detector at a fixed or variable angle registers the scattering intensity. Nanoparticle solutions commonly comprise of a distribution of sizes due to the imperfections in synthesis and natural conformational variances in the vast number of atoms involved. The polydispersity index (PI) is the metric equivalent to the relative variance of size distribution. DLS measurements were performed using a Malvern Zetasizer Nano ZS operating at 15 mW of a solid-state laser ( $\lambda = 670$  nm), using a scattering of  $90^\circ$ . For each synthesis, the same dilution used for UV-vis was used for size and charge analysis within an optical density range between 0.3 to 0.5 units.

## ***In vitro* studies**

### **Cell culture**

Deidentified Panc-1 and MiaPaCa-2 pancreatic cancer cell lines purchased from the American Type Culture Collection (Manassas, VA, US) were cultured in complete growth medium (DMEM/F-12 supplemented with 10% FBS, 100 units/mL penicillin and 100 units/mL streptomycin). HPDE (human pancreatic ductal epithelial) cells were cultured in Keratinocyte SFM (serum-free medium) supplemented with 25  $\mu$ g EGF (human recombinant epithelial growth factor) and 25 mg BPE (bovine pituitary extract). Cells were passaged once or twice weekly for maintenance, depending on growth rate and confluence. General passage protocol includes rinsing with phosphate buffered saline (PBS – HyClone SH30256), detachment using 0.05% or .025% trypsin-EDTA (ThermoFisher) with incubation for 5-20 min, neutralization using growth medium plus trypsin inhibitor for HPDE cells, centrifugation and finally resuspension to desired cell concentration. Cell concentrations were determined using the automated BioRad TC10™ cell counter. Cell culture incubators were maintained at 37°C, 5% CO and 90% - 95% humidity.

All tissue culture plates and flasks were labelled with cell line name, passage number, date of passage and initials of experimenter.

### **Cellular gold content**

Following a 24 hour treatment period, cells washed thrice with PBS, trypsinized with 0.05% or 0.25% Trypsin in EDTA solution (Invitrogen), and cell suspensions prepared for inductively coupled plasma mass-spectrometry (ICP-MS). A minimum of 500,000 cells per experimental condition are suspended in 50  $\mu$ L of PBS and 1 mL of Aqua Regia solution (1:3 HNO<sub>3</sub>:HCl) added to digest the samples. These suspensions are kept at room temperature for 2 – 3 days. After complete digestion, the final volume for each sample was brought to 10 mL by adding 1% Aqua Regia solution, and each sample run through an ICP-MS instrument (Perkin-Elmer Inc.) to quantify gold content. A similar procedure is carried out for fractionated samples, and amount of protein used to normalize gold content instead of cell count.

### **Imaging**

Light microscopy, fluorescent and darkfield imaging is executed using the Leica DMI8000B, Leica Microsystems, Wetzlar, Germany. For TEM analysis, samples are fixed with a solution containing 3% glutaraldehyde plus 2% paraformaldehyde in 0.1 M cacodylate buffer, pH 7.3, then washed in 0.1 M sodium cacodylate buffer and treated with 0.1% Millipore-filtered cacodylate buffered tannic acid, postfixed with 1% buffered osmium, and stained en bloc with 1% Millipore-filtered uranyl acetate. The samples are dehydrated in increasing concentrations of ethanol, infiltrated, and embedded in LX-112 medium. The samples are polymerized in a 60 C oven for approximately 3 days. Ultrathin sections are cut in a Leica Ultracut microtome (Leica, Deerfield, IL), stained with uranyl acetate and lead citrate in a Leica EM Stainer, and examined in a JEM 1010 transmission electron microscope (JEOL, USA, Inc., Peabody, MA) at an accelerating voltage of 80 kV. Digital images are obtained using AMT Imaging System

(Advanced Microscopy Techniques Corp, Danvers, MA). This work was possible with the CCSG grant NIH P30CA016672 to the High Resolution Electron Microscopy Facility.

### **Radiosensitization assays**

*In vitro* radiosensitization was evaluated for both Panc-1 and MiaPaCa-2 cell lines using the classic clonogenic assay. Briefly, cells are plated and treated with AuNSs for 24 hrs prior to RT (0, 2, 4 and 6 Gy) using XRAD 320. The cells were harvested and a known number of cells were re-plated in sextuplicate and allowed to grow in culture for 9-14 days to allow for colony formation. The colonies were fixed and stained with 1% crystal violet in absolute alcohol, washed extensively to remove excess dye, and imaged using a colony counter (GelCount, Oxford Optronix). The numbers of surviving colonies with >50 cells/colony were counted, survival curves were plotted after normalizing for the cytotoxicity induced by AuNS alone, and data were fitted to a linear-quadratic model. DEF was calculated as the ratio of the dose resulting in 10% survival with radiation alone to that resulting in 10% survival with radiation plus AuNS (normalized for AuNS cytotoxicity).

### **Mechanistic studies**

All experiments were performed after 24 hr incubation period for cell attachment. ROS studies are performed using glass bottom 96-well plates, experiments for DNA DSB analysis are plated on glass chamber slides for imaging and COMET assay studies are plated normally and transferred to provided slide. Cells are also treated for 24 hrs according to assigned treatment group prior to RT. ROS production was evaluated using the ROS-Glo kit (G8820, Promega). DSB was evaluated by fixing cells and exposing them to anti- $\gamma$ -H2AX (Abcam ab11174) or anti-53BP1 (Abcam ab172580) primary antibodies after blocking with 5% BSA overnight at 4°C. They were then stained with secondary antibodies conjugated to Alexa Fluor 647 (Texas Red – ThermoFisher Scientific A32723) or Alexa Fluor 488 (FITC – ThermoFisher Scientific A31852) for 2 hours at room temperature, and lastly stained with DAPI (blue). Images were captured using

a fluorescence microscope (Leica DMI6000B, Leica Microsystems, Wetzlar, Germany) and foci of immunofluorescence within the nuclei were analyzed using SPOT software (Sterling Heights, MI, USA). At least 50 nuclei were counted per experimental condition. Seahorse analysis was performed per Agilent specifications for the assay (manual part number 103016-400 and kit part number 103015-100). The TMRE transmembrane potential assay was evaluated using the Abcam kit instructions (Ab113852).

### ***In vivo studies***

All animal studies were performed in accordance with IACUC guidelines with the approval of the MD Anderson/UTHealth animal facility committee. Six to eight-week-old male nude mice (Swiss nu/nu) were obtained from our animal facility and housed with a 12-hour light/dark cycle at 22°C, with food and water *ad libitum*. Human pancreatic Panc-1 or Mia-Paca xenografts were grown in the hind upper right leg of mice by injecting  $0.5 - 1 \times 10^6$  cultured cells subcutaneously while mice were under Ketamine and Xylazine anesthesia. Tumors were grown to 6 – 7 mm diameter size prior to any treatment.

### **Biodistribution studies**

For all biodistribution experiments, a delay of 24 hours was carried out between nanoparticle treatment and organ collection. Following tissue collection, samples were stored in pre-weighed glass vials and frozen at -80°C until further processing. Frozen samples were lyophilized for 2 – 7 days to ensure complete dehydration of tissues, then dry weights of tissues acquired. Afterwards, 1 mL of Aqua Regia was added to each vial for digestion of tissues with slight heating for more dense tissues like liver and brain. 1% nitric acid solution was added to digested samples to bring the final volume to 10 mL for each sample, and this solution filtered through a 0.25 µm microfilters prior to inductively coupled mass spectrometry (ICP-MS) analysis. Liver and spleen samples were further diluted based on previous experimental data generated in the lab.

### **Tumor growth delay studies**

Xenograft pancreatic tumors were used to assess tumor growth delay. Mice receiving combined AuNS and radiation (RT) were injected with 100  $\mu$ L of 20 OD of either pAuNS, sAuNS or nAuNS 24 hours prior to RT. Control mice treated using only RT received 100  $\mu$ L PBS. Mice were anesthetized with 100 – 200  $\mu$ L of 5% Ketamine and 10% Xylazine in PBS by intraperitoneal injection ~20 minutes prior to irradiation. RT was delivered using a Philips RT-250 orthovoltage unit equipped with a cone applicator to focus radiation toward the tumor target. The settings for RT delivery included a 250 kVp beam with a Cu-filter, and an experimentally measured cone application factor to properly correct the dose rate determined under standard conditions.

Tumors were measured in millimeters using calipers along the long (L) and short (S) axes one day prior to and the day of RT, then 2 – 3 times weekly post-RT treatment. Tumor volumes are calculated using the equation below. Tumor volumes were normalized to the starting tumor volume for each mouse.

### **Liposomal and hyperthermia studies**

Hyperthermia treatments were delivered using a water bath with a temperature set to 44°C in order to maintain a temperature of 42°C at the surface. Mice were anesthetized with 100 – 200  $\mu$ L of 5% Ketamine and 10% Xylazine in PBS by intraperitoneal injection, and suspended in Styrofoam floaters with a cut-out to allow extension of the hind limb bearing the implanted tumors into the water bath. Tumors were exposed for 5 min, and mice transferred to a warming blanket to sleep off the anesthesia. For the biodistribution and tumor growth delay with hyperthermia experiments, a delay of 24 hours was completed between liposome treatment, then again after liposome treatment prior to organ harvest or RT for a total of 48 hours from nanoparticle-liposome injection.



### **Measurement of complement activation *in vitro***

Nanoparticles were incubated with undiluted normal human serum collected and isolated from 5 healthy individuals at 37 C for 30min. Activation of the classical, metabolic and lechitin complement pathways was determined by using a kit (WIESLAB® Complement system Screen). In a typical experiment, 10uL of nanoparticle formulation was mixed with 50 uL serum in Eppendorf tubes then incubated for 30min at 37 C. The serum was then diluted with reagents for blank samples, positive and negative controls, and reagents for the respective pathways for 60 – 70 min at 37 C per the protocol. Subsequently, the samples were washed 3 times, incubated with substrate solution provided for another 30 min prior to measurement of the absorbance with a microplate reader at 405 nm.

### **Measurement of coagulation assays *in vitro***

Similar to the complement activation assay, GNPs were incubated with normal human plasma isolated from 4 healthy donors at 37 C for 30min. All samples were run in triplicate. The samples were then immediately submitted to the Division of Laboratory Medicine core at MD Anderson Cancer Center for evaluation of prothrombin time (PT), the International Normalized Ratio (INR), activated partial thromboplastin time (aPTT) and thrombin time (TT).

### **Statistical analysis**

Statistical analysis: Quantitative data are presented as mean + standard deviation, or mean + standard error of the mean. The differences between groups were compared using a student's t-test or one-way analysis of variance (ANOVA) with repeated measures, then followed by Tukey's HSD test. Tumor volumes were compared using a Kruskal-Wallis test then a Mann-Whitney test. Aggregate survival in various groups were compared using Kaplan-Meier curves and the Log-rank test. Two-sided p-values less than 0.01 were considered statistically significant.

## Bibliography

1. Siegel, R.L., K.D. Miller, and A. Jemal, *Cancer statistics, 2020*. CA Cancer J Clin, 2020. **70**(1): p. 7-30.
2. Rahib, L., B.D. Smith, R. Aizenberg, A.B. Rosenzweig, J.M. Fleshman, and L.M. Matrisian, *Projecting cancer incidence and deaths to 2030: the unexpected burden of thyroid, liver, and pancreas cancers in the United States*. Cancer Res, 2014. **74**(11): p. 2913-21.
3. GB., M., *De sedibus, et causis morborum per anatomen indagatis libri quinque*. 1761: Venetiis: Typog Remondiniana;.
4. Da Costa, J., *On the morbid anatomy and symptoms of cancer of the pancreas*. 1858, Philadelphia: J. B. Lippincott & Co.
5. WS, H., *Contributions to the surgery of the bile passages, especially of the common bile duct*. Boston Med Surg J, 1899(141): p. 645–654.
6. Whipple, A.O., W.B. Parsons, and C.R. Mullins, *Treatment of Carcinoma of the Ampulla of Vater*. Ann Surg, 1935. **102**(4): p. 763-79.
7. Brunschwig, A., *Resection of head of pancreas and duodenum for carcinoma--pancreatoduodenectomy*. CA Cancer J Clin, 1974. **24**(6): p. 363-7.
8. Whipple, A.O., *Observations on radical surgery for lesions of the pancreas*. Surg Gynecol Obstet, 1946. **82**: p. 623-31.
9. Whipple, A.O., *A reminiscence: pancreaticoduodenectomy*. Rev Surg, 1963. **20**: p. 221-5.
10. Cameron, J.L., T.S. Riall, J. Coleman, and K.A. Belcher, *One thousand consecutive pancreaticoduodenectomies*. Ann Surg, 2006. **244**(1): p. 10-5.
11. Poruk, K.E., M.A. Firpo, D.G. Adler, and S.J. Mulvihill, *Screening for pancreatic cancer: why, how, and who?* Ann Surg, 2013. **257**(1): p. 17-26.

12. Aho, U., X. Zhao, M. Lohr, and R. Andersson, *Molecular mechanisms of pancreatic cancer and potential targets of treatment*. Scand J Gastroenterol, 2007. **42**(3): p. 279-96.
13. Noe, M. and L.A. Brosens, *Pathology of Pancreatic Cancer Precursor Lesions*. Surg Pathol Clin, 2016. **9**(4): p. 561-580.
14. McGuigan, A., P. Kelly, R.C. Turkington, C. Jones, H.G. Coleman, and R.S. McCain, *Pancreatic cancer: A review of clinical diagnosis, epidemiology, treatment and outcomes*. World J Gastroenterol, 2018. **24**(43): p. 4846-4861.
15. Goonetilleke, K.S. and A.K. Siriwardena, *Systematic review of carbohydrate antigen (CA 19-9) as a biochemical marker in the diagnosis of pancreatic cancer*. Eur J Surg Oncol, 2007. **33**(3): p. 266-70.
16. Yeh, R., J. Steinman, L. Luk, M.D. Kluger, and E.M. Hecht, *Imaging of pancreatic cancer: what the surgeon wants to know*. Clin Imaging, 2017. **42**: p. 203-217.
17. Edge, S.B. and C.C. Compton, *The American Joint Committee on Cancer: the 7th edition of the AJCC cancer staging manual and the future of TNM*. Ann Surg Oncol, 2010. **17**(6): p. 1471-4.
18. Amin, M.B., F.L. Greene, S.B. Edge, C.C. Compton, J.E. Gershenwald, R.K. Brookland, L. Meyer, D.M. Gress, D.R. Byrd, and D.P. Winchester, *The Eighth Edition AJCC Cancer Staging Manual: Continuing to build a bridge from a population-based to a more "personalized" approach to cancer staging*. CA Cancer J Clin, 2017. **67**(2): p. 93-99.
19. Board., P.A.T.E., *Pancreatic Cancer Treatment (Adult) (PDQ®): Health Professional Version*. 2020, PDQ Cancer Information Summaries [Internet]: National Cancer Institute (US).
20. Karmazanovsky, G., V. Fedorov, V. Kubyshkin, and A. Kotchatkov, *Pancreatic head cancer: accuracy of CT in determination of resectability*. Abdom Imaging, 2005. **30**(4): p. 488-500.

21. Tempero, M.A., M.P. Malafa, E.G. Chiorean, B. Czito, C. Scaife, A.K. Narang, C. Fountzilas, B.M. Wolpin, M. Al-Hawary, H. Asbun, S.W. Behrman, A.B. Benson, E. Binder, D.B. Cardin, C. Cha, V. Chung, M. Dillhoff, E. Dotan, C.R. Ferrone, G. Fisher, J. Hardacre, W.G. Hawkins, A.H. Ko, N. LoConte, A.M. Lowy, C. Moravek, E.K. Nakakura, E.M. O'Reilly, J. Obando, S. Reddy, S. Thayer, R.A. Wolff, J.L. Burns, and G. Zuccarino-Catania, *Pancreatic Adenocarcinoma, Version 1.2019*. J Natl Compr Canc Netw, 2019. **17**(3): p. 202-210.
22. Ansari, D., I. Keussen, and R. Andersson, *Positron emission tomography in malignancies of the liver, pancreas and biliary tract - indications and potential pitfalls*. Scand J Gastroenterol, 2013. **48**(3): p. 259-65.
23. Vincent, A., J. Herman, R. Schulick, R.H. Hruban, and M. Goggins, *Pancreatic cancer*. Lancet, 2011. **378**(9791): p. 607-20.
24. Bachmann, J., C.W. Michalski, M.E. Martignoni, M.W. Buchler, and H. Friess, *Pancreatic resection for pancreatic cancer*. HPB (Oxford), 2006. **8**(5): p. 346-51.
25. Kalser, M.H. and S.S. Ellenberg, *Pancreatic cancer. Adjuvant combined radiation and chemotherapy following curative resection*. Arch Surg, 1985. **120**(8): p. 899-903.
26. Neoptolemos, J.P., D.D. Stocken, H. Friess, C. Bassi, J.A. Dunn, H. Hickey, H. Beger, L. Fernandez-Cruz, C. Dervenis, F. Lacaine, M. Falconi, P. Pederzoli, A. Pap, D. Spooner, D.J. Kerr, M.W. Buchler, and C. European Study Group for Pancreatic, *A randomized trial of chemoradiotherapy and chemotherapy after resection of pancreatic cancer*. N Engl J Med, 2004. **350**(12): p. 1200-10.
27. Oettle, H., P. Neuhaus, A. Hochhaus, J.T. Hartmann, K. Gellert, K. Ridwelski, M. Niedergethmann, C. Zulke, J. Fahlke, M.B. Arning, M. Sinn, A. Hinke, and H. Riess, *Adjuvant chemotherapy with gemcitabine and long-term outcomes among patients with resected pancreatic cancer: the CONKO-001 randomized trial*. JAMA, 2013. **310**(14): p. 1473-81.

28. Neoptolemos, J.P., M.J. Moore, T.F. Cox, J.W. Valle, D.H. Palmer, A.C. McDonald, R. Carter, N.C. Tebbutt, C. Dervenis, D. Smith, B. Glimelius, R.M. Charnley, F. Lacaine, A.G. Scarfe, M.R. Middleton, A. Anthoney, P. Ghaneh, C.M. Halloran, M.M. Lerch, A. Olah, C.L. Rawcliffe, C.S. Verbeke, F. Campbell, M.W. Buchler, and C. European Study Group for Pancreatic, *Effect of adjuvant chemotherapy with fluorouracil plus folinic acid or gemcitabine vs observation on survival in patients with resected periampullary adenocarcinoma: the ESPAC-3 periampullary cancer randomized trial*. JAMA, 2012. **308**(2): p. 147-56.
29. Regine, W.F., K.A. Winter, R. Abrams, H. Safran, J.P. Hoffman, A. Konski, A.B. Benson, J.S. Macdonald, T.A. Rich, and C.G. Willett, *Fluorouracil-based chemoradiation with either gemcitabine or fluorouracil chemotherapy after resection of pancreatic adenocarcinoma: 5-year analysis of the U.S. Intergroup/RTOG 9704 phase III trial*. Ann Surg Oncol, 2011. **18**(5): p. 1319-26.
30. Sener, S.F., A. Fremgen, H.R. Menck, and D.P. Winchester, *Pancreatic cancer: a report of treatment and survival trends for 100,313 patients diagnosed from 1985-1995, using the National Cancer Database*. J Am Coll Surg, 1999. **189**(1): p. 1-7.
31. van Veldhuisen, E., C. van den Oord, L.J. Brada, M.S. Walma, J.A. Vogel, J.W. Wilmink, M. Del Chiaro, K.P. van Lienden, M.R. Meijerink, G. van Tienhoven, T. Hackert, C.L. Wolfgang, H. van Santvoort, B. Groot Koerkamp, O.R. Busch, I.Q. Molenaar, C.H. van Eijck, M.G. Besselink, G. Dutch Pancreatic Cancer, and C. International Collaborative Group on Locally Advanced Pancreatic, *Locally Advanced Pancreatic Cancer: Work-Up, Staging, and Local Intervention Strategies*. Cancers (Basel), 2019. **11**(7).
32. Vidri, R.J., A.O. Vogt, D.C. Macgillivray, I.J. Bristol, and T.L. Fitzgerald, *Better Defining the Role of Total Neoadjuvant Radiation: Changing Paradigms in Locally Advanced Pancreatic Cancer*. Ann Surg Oncol, 2019. **26**(11): p. 3701-3708.

33. Iacobuzio-Donahue, C.A., B. Fu, S. Yachida, M. Luo, H. Abe, C.M. Henderson, F. Vilardell, Z. Wang, J.W. Keller, P. Banerjee, J.M. Herman, J.L. Cameron, C.J. Yeo, M.K. Halushka, J.R. Eshleman, M. Raben, A.P. Klein, R.H. Hruban, M. Hidalgo, and D. Laheru, *DPC4 gene status of the primary carcinoma correlates with patterns of failure in patients with pancreatic cancer*. J Clin Oncol, 2009. **27**(11): p. 1806-13.
34. EB, P., *Radiation oncology physics: a handbook for teachers and students*. 2005: International Atomic Energy Agency.
35. Tonnessen, B.H. and L. Pounds, *Radiation physics*. J Vasc Surg, 2011. **53**(1 Suppl): p. 6S-8S.
36. Gibbons, J., *Khan's The Physics of Radiation Therapy*. 6 ed. 2019: Lippincott Williams & Wilkins (LWW).
37. Joiner MC, V.d.K.A., *Basic Clinical Radiobiology*. 5 ed. Taylor & Francis. 2016.
38. Reisz, J.A., N. Bansal, J. Qian, W. Zhao, and C.M. Furdul, *Effects of ionizing radiation on biological molecules--mechanisms of damage and emerging methods of detection*. Antioxid Redox Signal, 2014. **21**(2): p. 260-92.
39. Lomax, M.E., L.K. Folkes, and P. O'Neill, *Biological consequences of radiation-induced DNA damage: relevance to radiotherapy*. Clin Oncol (R Coll Radiol), 2013. **25**(10): p. 578-85.
40. Jones, B.L., S. Krishnan, and S.H. Cho, *Estimation of microscopic dose enhancement factor around gold nanoparticles by Monte Carlo calculations*. Med Phys, 2010. **37**(7): p. 3809-16.
41. Gunderson L, T.J., *Clinical Radiation Oncology*. 4 ed. 2015: Elsevier.
42. Hubener, K.H., M. Baumann, A. Krull, and R. Schwarz, *Clinically important factors modifying the response of tumors and normal tissue to radiation therapy*. Recent Results Cancer Res, 1993. **130**: p. 41-7.
43. Phillips, T.L. and T.H. Wasserman, *Promise of radiosensitizers and radioprotectors in the treatment of human cancer*. Cancer Treat Rep, 1984. **68**(1): p. 291-302.

44. Spalding, A.C. and T.S. Lawrence, *New and emerging radiosensitizers and radioprotectors*. Cancer Invest, 2006. **24**(4): p. 444-56.
45. RP, F., *There's plenty of room at the bottom*. Eng. Sci., 1960. **23**: p. 22 - 36.
46. Taniguchi N., A.C., Kobayashi T., *On the basic concept of nano-technology*. Proceedings of the International Conference on Production Engineering, 1974.
47. Roduner, E., *Size matters: why nanomaterials are different*. Chem Soc Rev, 2006. **35**(7): p. 583-92.
48. Ramos, A.P., M.A.E. Cruz, C.B. Tovani, and P. Ciancaglini, *Biomedical applications of nanotechnology*. Biophys Rev, 2017. **9**(2): p. 79-89.
49. Zahin, N., R. Anwar, D. Tewari, M.T. Kabir, A. Sajid, B. Mathew, M.S. Uddin, L. Aleya, and M.M. Abdel-Daim, *Nanoparticles and its biomedical applications in health and diseases: special focus on drug delivery*. Environ Sci Pollut Res Int, 2020. **27**(16): p. 19151-19168.
50. Chung EJ., L.L., Rinaldi, C., *Nanoparticles for Biomedical Applications*. 2019: Elsevier.
51. Khan HA., S.M., Nayak, A., Kishore, U. Khan, A., *Nanoparticles for biomedical applications: An overview*, in *Nanobiomaterials*. 2018: Elsevier. p. 357-384.
52. Salata, O., *Applications of nanoparticles in biology and medicine*. J Nanobiotechnology, 2004. **2**(1): p. 3.
53. Yohan, D. and B.D. Chithrani, *Applications of nanoparticles in nanomedicine*. J Biomed Nanotechnol, 2014. **10**(9): p. 2371-92.
54. Wang, E.C. and A.Z. Wang, *Nanoparticles and their applications in cell and molecular biology*. Integr Biol (Camb), 2014. **6**(1): p. 9-26.
55. Li, Y., C. Ayala-Orozco, P.R. Rauta, and S. Krishnan, *The application of nanotechnology in enhancing immunotherapy for cancer treatment: current effects and perspective*. Nanoscale, 2019. **11**(37): p. 17157-17178.

56. Jeevanandam, J., A. Barhoum, Y.S. Chan, A. Dufresne, and M.K. Danquah, *Review on nanoparticles and nanostructured materials: history, sources, toxicity and regulations*. Beilstein J Nanotechnol, 2018. **9**: p. 1050-1074.
57. Aryal, S., H. Park, J.F. Leary, and J. Key, *Top-down fabrication-based nano/microparticles for molecular imaging and drug delivery*. Int J Nanomedicine, 2019. **14**: p. 6631-6644.
58. Jeyaraj, M., S. Gurunathan, M. Qasim, M.H. Kang, and J.H. Kim, *A Comprehensive Review on the Synthesis, Characterization, and Biomedical Application of Platinum Nanoparticles*. Nanomaterials (Basel), 2019. **9**(12).
59. Freitas de Freitas, L., G.H.C. Varca, J.G. Dos Santos Batista, and A. Benevolo Lugao, *An Overview of the Synthesis of Gold Nanoparticles Using Radiation Technologies*. Nanomaterials (Basel), 2018. **8**(11).
60. Raliya, R., T. Singh Chadha, K. Haddad, and P. Biswas, *Perspective on Nanoparticle Technology for Biomedical Use*. Curr Pharm Des, 2016. **22**(17): p. 2481-90.
61. Alex, S. and A. Tiwari, *Functionalized Gold Nanoparticles: Synthesis, Properties and Applications--A Review*. J Nanosci Nanotechnol, 2015. **15**(3): p. 1869-94.
62. Barkat, M.A., Harshita, S. Beg, M.J. Naim, F.H. Pottoo, S.P. Singh, and F.J. Ahmad, *Current Progress in Synthesis, Characterization and Applications of Silver Nanoparticles: Precepts and Prospects*. Recent Pat Antiinfect Drug Discov, 2018. **13**(1): p. 53-69.
63. Wagner, V., A. Dullaart, A.K. Bock, and A. Zweck, *The emerging nanomedicine landscape*. Nat Biotechnol, 2006. **24**(10): p. 1211-7.
64. Allen, T.M. and P.R. Cullis, *Drug delivery systems: entering the mainstream*. Science, 2004. **303**(5665): p. 1818-22.
65. Burgess, P., P.B. Hutt, O.C. Farokhzad, R. Langer, S. Minick, and S. Zale, *On firm ground: IP protection of therapeutic nanoparticles*. Nat Biotechnol, 2010. **28**(12): p. 1267-70.



66. Hett, A., *Nanotechnology: Small Matter, Many Unknowns*. 2004: Zurich.
67. Langer, R. and J. Folkman, *Polymers for the sustained release of proteins and other macromolecules*. *Nature*, 1976. **263**(5580): p. 797-800.
68. Schmaljohann, D., *Thermo- and pH-responsive polymers in drug delivery*. *Adv Drug Deliv Rev*, 2006. **58**(15): p. 1655-70.
69. Verma, R.K., B. Mishra, and S. Garg, *Osmotically controlled oral drug delivery*. *Drug Dev Ind Pharm*, 2000. **26**(7): p. 695-708.
70. Colombo, P., R. Bettini, P. Santi, and N.A. Peppas, *Swellable matrices for controlled drug delivery: gel-layer behaviour, mechanisms and optimal performance*. *Pharm Sci Technolo Today*, 2000. **3**(6): p. 198-204.
71. Quader MA., S.C., Sumpio BE., *Radio Contrast Agents: History and Evolution.*, in *Text Angiology*. 2000, Springer: New york, NY. p. 775-783.
72. Mody, V.V., R. Siwale, A. Singh, and H.R. Mody, *Introduction to metallic nanoparticles*. *J Pharm Bioallied Sci*, 2010. **2**(4): p. 282-9.
73. Sharma, V., Park, K., Srinivasarao, M., *Colloidal dispersion of gold nanorods: Historical background, optical properties, seed-mediated synthesis, shape separation and self-assembly*, in *Materials Science and Engineering: R: Reports*. 2009. p. 1-38.
74. Faraday, M., *The Bakerian lecture: Experimental relations of gold (and other metals) to light*. *Philosophical Transactions Royal Soc. London*, 1857. **147**.
75. Hainfeld, J.F., D.N. Slatkin, and H.M. Smilowitz, *The use of gold nanoparticles to enhance radiotherapy in mice*. *Phys Med Biol*, 2004. **49**(18): p. N309-15.
76. Schuemann, J., R. Berbeco, D.B. Chithrani, S.H. Cho, R. Kumar, S.J. McMahon, S. Sridhar, and S. Krishnan, *Roadmap to Clinical Use of Gold Nanoparticles for Radiation Sensitization*. *Int J Radiat Oncol Biol Phys*, 2016. **94**(1): p. 189-205.
77. Yeh, Y.C., B. Creran, and V.M. Rotello, *Gold nanoparticles: preparation, properties, and applications in bionanotechnology*. *Nanoscale*, 2012. **4**(6): p. 1871-80.

78. Huang, X., I.H. El-Sayed, W. Qian, and M.A. El-Sayed, *Cancer cell imaging and photothermal therapy in the near-infrared region by using gold nanorods*. J Am Chem Soc, 2006. **128**(6): p. 2115-20.
79. Huff, T.B., L. Tong, Y. Zhao, M.N. Hansen, J.X. Cheng, and A. Wei, *Hyperthermic effects of gold nanorods on tumor cells*. Nanomedicine (Lond), 2007. **2**(1): p. 125-32.
80. Siddiqi, K.S. and A. Husen, *Recent advances in plant-mediated engineered gold nanoparticles and their application in biological system*. J Trace Elem Med Biol, 2017. **40**: p. 10-23.
81. Toma, H.E., V.M. Zamarion, S.H. Toma, and K. Araki, *The Coordination Chemistry at Gold Nanoparticles*. Journal of the Brazilian Chemical Society, 2010. **21**(7): p. 1158-1176.
82. Choi, H.S., W. Liu, F. Liu, K. Nasr, P. Misra, M.G. Bawendi, and J.V. Frangioni, *Design considerations for tumour-targeted nanoparticles*. Nat Nanotechnol, 2010. **5**(1): p. 42-7.
83. Kreyling, W.G., A.M. Abdelmonem, Z. Ali, F. Alves, M. Geiser, N. Haberl, R. Hartmann, S. Hirn, D.J. de Aberasturi, K. Kantner, G. Khadem-Saba, J.M. Montenegro, J. Rejman, T. Rojo, I.R. de Larramendi, R. Ufartes, A. Wenk, and W.J. Parak, *In vivo integrity of polymer-coated gold nanoparticles*. Nat Nanotechnol, 2015. **10**(7): p. 619-23.
84. Kerker, M., *The scattering of light, and other electromagnetic radiation*. Physical chemistry, a series of monographs, 16. 1969, New York,: Academic Press. xv, 666 p.
85. Bohren, C.F. and D.R. Huffman, *Absorption and scattering of light by small particles*. A Wiley-interscience publication. 1983, New York, N.Y., etc.: Wiley. xiv, 530 p.
86. Huang, X.H. and M.A. El-Sayed, *Gold nanoparticles: Optical properties and implementations in cancer diagnosis and photothermal therapy*. Journal of Advanced Research, 2010. **1**(1): p. 13-28.
87. Mie, G. and Royal Aircraft Establishment., *Contributions to the optics of turbid media, particularly of colloidal metal solutions : Beiträge zur optik trüber medien, speziell*

- kolloidalen metallösungen*. Library translation / Royal Aircraft Establishment. 1976, Farnborough: RAE.
88. Jin, R., Y. Cao, C.A. Mirkin, K.L. Kelly, G.C. Schatz, and J.G. Zheng, *Photoinduced conversion of silver nanospheres to nanoprisms*. Science, 2001. **294**(5548): p. 1901-3.
  89. West, J.L. and N.J. Halas, *Applications of nanotechnology to biotechnology commentary*. Curr Opin Biotechnol, 2000. **11**(2): p. 215-7.
  90. El-Sayed, I.H., X. Huang, and M.A. El-Sayed, *Surface plasmon resonance scattering and absorption of anti-EGFR antibody conjugated gold nanoparticles in cancer diagnostics: applications in oral cancer*. Nano Lett, 2005. **5**(5): p. 829-34.
  91. Amendola, V., R. Pilot, M. Frasconi, O.M. Marago, and M.A. Iati, *Surface plasmon resonance in gold nanoparticles: a review*. J Phys Condens Matter, 2017. **29**(20): p. 203002.
  92. Edidin, M., *Lipids on the frontier: a century of cell-membrane bilayers*. Nat Rev Mol Cell Biol, 2003. **4**(5): p. 414-8.
  93. Shi, Y., M. Cai, L. Zhou, and H. Wang, *The structure and function of cell membranes studied by atomic force microscopy*. Semin Cell Dev Biol, 2018. **73**: p. 31-44.
  94. Zhao, F., Y. Zhao, Y. Liu, X. Chang, C. Chen, and Y. Zhao, *Cellular uptake, intracellular trafficking, and cytotoxicity of nanomaterials*. Small, 2011. **7**(10): p. 1322-37.
  95. Arnida, A. Malugin, and H. Ghandehari, *Cellular uptake and toxicity of gold nanoparticles in prostate cancer cells: a comparative study of rods and spheres*. J Appl Toxicol, 2010. **30**(3): p. 212-7.
  96. Kah, J.C., K.Y. Wong, K.G. Neoh, J.H. Song, J.W. Fu, S. Mhaisalkar, M. Olivo, and C.J. Sheppard, *Critical parameters in the pegylation of gold nanoshells for biomedical applications: an in vitro macrophage study*. J Drug Target, 2009. **17**(3): p. 181-93.
  97. Chithrani, B.D., A.A. Ghazani, and W.C. Chan, *Determining the size and shape dependence of gold nanoparticle uptake into mammalian cells*. Nano Lett, 2006. **6**(4): p. 662-8.

98. Kam, N.W., Z. Liu, and H. Dai, *Carbon nanotubes as intracellular transporters for proteins and DNA: an investigation of the uptake mechanism and pathway*. Angew Chem Int Ed Engl, 2006. **45**(4): p. 577-81.
99. Chithrani, B.D. and W.C. Chan, *Elucidating the mechanism of cellular uptake and removal of protein-coated gold nanoparticles of different sizes and shapes*. Nano Lett, 2007. **7**(6): p. 1542-50.
100. Silverstein, S.C., R.M. Steinman, and Z.A. Cohn, *Endocytosis*. Annu Rev Biochem, 1977. **46**: p. 669-722.
101. Wenthe, S.R. and M.P. Rout, *The nuclear pore complex and nuclear transport*. Cold Spring Harb Perspect Biol, 2010. **2**(10): p. a000562.
102. Gorlich, D., *Nuclear protein import*. Curr Opin Cell Biol, 1997. **9**(3): p. 412-9.
103. Pemberton, L.F. and B.M. Paschal, *Mechanisms of receptor-mediated nuclear import and nuclear export*. Traffic, 2005. **6**(3): p. 187-98.
104. Li, X., X. Wu, H. Yang, L. Li, Z. Ye, and Y. Rao, *A nuclear targeted Dox-apramer loaded liposome delivery platform for the circumvention of drug resistance in breast cancer*. Biomed Pharmacother, 2019. **117**: p. 109072.
105. Cai, Y., H. Shen, J. Zhan, M. Lin, L. Dai, C. Ren, Y. Shi, J. Liu, J. Gao, and Z. Yang, *Supramolecular "Trojan Horse" for Nuclear Delivery of Dual Anticancer Drugs*. J Am Chem Soc, 2017. **139**(8): p. 2876-2879.
106. Sakhrani, N.M. and H. Padh, *Organelle targeting: third level of drug targeting*. Drug Des Devel Ther, 2013. **7**: p. 585-99.
107. Connor, E.E., J. Mwamuka, A. Gole, C.J. Murphy, and M.D. Wyatt, *Gold nanoparticles are taken up by human cells but do not cause acute cytotoxicity*. Small, 2005. **1**(3): p. 325-7.
108. Goodman, C.M., C.D. McCusker, T. Yilmaz, and V.M. Rotello, *Toxicity of gold nanoparticles functionalized with cationic and anionic side chains*. Bioconjug Chem, 2004. **15**(4): p. 897-900.

109. Murphy, C.J., A.M. Gole, J.W. Stone, P.N. Sisco, A.M. Alkilany, E.C. Goldsmith, and S.C. Baxter, *Gold nanoparticles in biology: beyond toxicity to cellular imaging*. *Acc Chem Res*, 2008. **41**(12): p. 1721-30.
110. Abuchowski, A., J.R. McCoy, N.C. Palczuk, T. van Es, and F.F. Davis, *Effect of covalent attachment of polyethylene glycol on immunogenicity and circulating life of bovine liver catalase*. *J Biol Chem*, 1977. **252**(11): p. 3582-6.
111. Takahashi, K., H. Nishimura, T. Yoshimoto, Y. Saito, and Y. Inada, *A chemical modification to make horseradish peroxidase soluble and active in benzene*. *Biochem Biophys Res Commun*, 1984. **121**(1): p. 261-5.
112. Yang, K., A. Basu, M. Wang, R. Chintala, M.C. Hsieh, S. Liu, J. Hua, Z. Zhang, J. Zhou, M. Li, H. Phyu, G. Petti, M. Mendez, H. Janjua, P. Peng, C. Longley, V. Borowski, M. Mehlig, and D. Filpula, *Tailoring structure-function and pharmacokinetic properties of single-chain Fv proteins by site-specific PEGylation*. *Protein Eng*, 2003. **16**(10): p. 761-70.
113. Tkachenko, A., H. Xie, S. Franzen, and D.L. Feldheim, *Assembly and characterization of biomolecule-gold nanoparticle conjugates and their use in intracellular imaging*. *Methods Mol Biol*, 2005. **303**: p. 85-99.
114. Briggs, S., Hattar, K. *Evolution of Gold Nanoparticles in Radiation Environment*. 2018.
115. Zhang, X., J.Z. Xing, J. Chen, L. Ko, J. Amanie, S. Gulavita, N. Pervez, D. Yee, R. Moore, and W. Roa, *Enhanced radiation sensitivity in prostate cancer by gold-nanoparticles*. *Clin Invest Med*, 2008. **31**(3): p. E160-7.
116. Chang, M.Y., A.L. Shiau, Y.H. Chen, C.J. Chang, H.H. Chen, and C.L. Wu, *Increased apoptotic potential and dose-enhancing effect of gold nanoparticles in combination with single-dose clinical electron beams on tumor-bearing mice*. *Cancer Sci*, 2008. **99**(7): p. 1479-84.
117. Matsudaira, H., A.M. Ueno, and I. Furuno, *Iodine contrast medium sensitizes cultured mammalian cells to X rays but not to gamma rays*. *Radiat Res*, 1980. **84**(1): p. 144-8.

118. Santos Mello, R., H. Callisen, J. Winter, A.R. Kagan, and A. Norman, *Radiation dose enhancement in tumors with iodine*. Med Phys, 1983. **10**(1): p. 75-8.
119. Rose, J.H., A. Norman, M. Ingram, C. Aoki, T. Solberg, and A. Mesa, *First radiotherapy of human metastatic brain tumors delivered by a computerized tomography scanner (CTRx)*. Int J Radiat Oncol Biol Phys, 1999. **45**(5): p. 1127-32.
120. Chithrani, D.B., S. Jelveh, F. Jalali, M. van Prooijen, C. Allen, R.G. Bristow, R.P. Hill, and D.A. Jaffray, *Gold nanoparticles as radiation sensitizers in cancer therapy*. Radiat Res, 2010. **173**(6): p. 719-28.
121. Ray, P.D., B.W. Huang, and Y. Tsuji, *Reactive oxygen species (ROS) homeostasis and redox regulation in cellular signaling*. Cell Signal, 2012. **24**(5): p. 981-90.
122. Joiner MC, V.d.K.A., *Basic Clinical Radiobiology Fourth Edition*. 2009: CRC Press.
123. Kastan, M.B. and J. Bartek, *Cell-cycle checkpoints and cancer*. Nature, 2004. **432**(7015): p. 316-23.
124. Warburg, O., F. Wind, and E. Negelein, *The Metabolism of Tumors in the Body*. J Gen Physiol, 1927. **8**(6): p. 519-30.
125. Wallace, D.C., *Mitochondria and cancer*. Nat Rev Cancer, 2012. **12**(10): p. 685-98.
126. Porporato, P.E., N. Filigheddu, J.M.B. Pedro, G. Kroemer, and L. Galluzzi, *Mitochondrial metabolism and cancer*. Cell Res, 2018. **28**(3): p. 265-280.
127. Foroozandeh, P. and A.A. Aziz, *Insight into Cellular Uptake and Intracellular Trafficking of Nanoparticles*. Nanoscale Res Lett, 2018. **13**(1): p. 339.
128. Leung, M.K., J.C. Chow, B.D. Chithrani, M.J. Lee, B. Oms, and D.A. Jaffray, *Irradiation of gold nanoparticles by x-rays: Monte Carlo simulation of dose enhancements and the spatial properties of the secondary electrons production*. Med Phys, 2011. **38**(2): p. 624-31.
129. Gyori, B.M., G. Venkatachalam, P.S. Thiagarajan, D. Hsu, and M.V. Clement, *OpenComet: an automated tool for comet assay image analysis*. Redox Biol, 2014. **2**: p. 457-65.

130. Bangham, A.D. and R.W. Horne, *Negative Staining of Phospholipids and Their Structural Modification by Surface-Active Agents as Observed in the Electron Microscope*. J Mol Biol, 1964. **8**: p. 660-8.
131. Chithrani, D.B., M. Dunne, J. Stewart, C. Allen, and D.A. Jaffray, *Cellular uptake and transport of gold nanoparticles incorporated in a liposomal carrier*. Nanomedicine, 2010. **6**(1): p. 161-9.
132. Wilhelm, S., Tavares, A., Dai, Q. et al., *Analysis of nanoparticle delivery to tumours*. Nat Rev Mater, 2016. **1**.
133. Blanco, E., H. Shen, and M. Ferrari, *Principles of nanoparticle design for overcoming biological barriers to drug delivery*. Nat Biotechnol, 2015. **33**(9): p. 941-51.
134. Thomas, O.S. and W. Weber, *Overcoming Physiological Barriers to Nanoparticle Delivery-Are We There Yet?* Front Bioeng Biotechnol, 2019. **7**: p. 415.
135. Gregoriadis, G., *Drug entrapment in liposomes*. FEBS Lett, 1973. **36**(3): p. 292-6.
136. Immordino, M.L., F. Dosio, and L. Cattel, *Stealth liposomes: review of the basic science, rationale, and clinical applications, existing and potential*. Int J Nanomedicine, 2006. **1**(3): p. 297-315.
137. Allen, T.M. and A. Chonn, *Large unilamellar liposomes with low uptake into the reticuloendothelial system*. FEBS Lett, 1987. **223**(1): p. 42-6.
138. Klibanov, A.L., K. Maruyama, V.P. Torchilin, and L. Huang, *Amphipathic polyethyleneglycols effectively prolong the circulation time of liposomes*. FEBS Lett, 1990. **268**(1): p. 235-7.
139. Udhain, A., K.M. Skubitz, and D.W. Northfelt, *Pegylated liposomal doxorubicin in the treatment of AIDS-related Kaposi's sarcoma*. Int J Nanomedicine, 2007. **2**(3): p. 345-52.
140. Miele, E., G.P. Spinelli, E. Miele, F. Tomao, and S. Tomao, *Albumin-bound formulation of paclitaxel (Abraxane ABI-007) in the treatment of breast cancer*. Int J Nanomedicine, 2009. **4**: p. 99-105.

141. Dass, C.R., T.L. Walker, M.A. Burton, and E.E. Decruz, *Enhanced anticancer therapy mediated by specialized liposomes*. J Pharm Pharmacol, 1997. **49**(10): p. 972-5.
142. Ta, T. and T.M. Porter, *Thermosensitive liposomes for localized delivery and triggered release of chemotherapy*. J Control Release, 2013. **169**(1-2): p. 112-25.
143. Garcia, A.A., R.A. Kempf, M. Rogers, and F.M. Muggia, *A phase II study of Doxil (liposomal doxorubicin): lack of activity in poor prognosis soft tissue sarcomas*. Ann Oncol, 1998. **9**(10): p. 1131-3.
144. Ellerhorst, J.A., A. Bedikian, S. Ring, A.C. Buzaid, O. Eton, and S.S. Legha, *Phase II trial of doxil for patients with metastatic melanoma refractory to frontline therapy*. Oncol Rep, 1999. **6**(5): p. 1097-9.
145. Gill, P.S., J. Wernz, D.T. Scadden, P. Cohen, G.M. Mukwaya, J.H. von Roenn, M. Jacobs, S. Kempin, I. Silverberg, G. Gonzales, M.U. Rarick, A.M. Myers, F. Shepherd, C. Sawka, M.C. Pike, and M.E. Ross, *Randomized phase III trial of liposomal daunorubicin versus doxorubicin, bleomycin, and vincristine in AIDS-related Kaposi's sarcoma*. J Clin Oncol, 1996. **14**(8): p. 2353-64.
146. Harris, L., G. Batist, R. Belt, D. Rovira, R. Navari, N. Azarnia, L. Welles, E. Winer, and T.D.S. Group, *Liposome-encapsulated doxorubicin compared with conventional doxorubicin in a randomized multicenter trial as first-line therapy of metastatic breast carcinoma*. Cancer, 2002. **94**(1): p. 25-36.
147. Shum, P., J.M. Kim, and D.H. Thompson, *Phototriggering of liposomal drug delivery systems*. Adv Drug Deliv Rev, 2001. **53**(3): p. 273-84.
148. Karanth, H. and R.S. Murthy, *pH-sensitive liposomes--principle and application in cancer therapy*. J Pharm Pharmacol, 2007. **59**(4): p. 469-83.
149. Schroeder, A., R. Honen, K. Turjeman, A. Gabizon, J. Kost, and Y. Barenholz, *Ultrasound triggered release of cisplatin from liposomes in murine tumors*. J Control Release, 2009. **137**(1): p. 63-8.



150. Landon, C.D., J.Y. Park, D. Needham, and M.W. Dewhirst, *Nanoscale Drug Delivery and Hyperthermia: The Materials Design and Preclinical and Clinical Testing of Low Temperature-Sensitive Liposomes Used in Combination with Mild Hyperthermia in the Treatment of Local Cancer*. Open Nanomed J, 2011. **3**: p. 38-64.
151. Motamarry, A.A., D.; Haemmerich, D., *Thermosensitive Liposomes*, in *Liposomes*, A. Catala, Ed., Editor. 2017, InTech.
152. Wust, P., B. Hildebrandt, G. Sreenivasa, B. Rau, J. Gellermann, H. Riess, R. Felix, and P.M. Schlag, *Hyperthermia in combined treatment of cancer*. Lancet Oncol, 2002. **3**(8): p. 487-97.
153. Society, A.C. *Survival rates for pancreatic cancer*. [cited 2020 March 5, 2020]; Available from: <https://www.cancer.org/cancer/pancreatic-cancer/detection-diagnosis-staging/survival-rates.html>.
154. Kamisawa, T., L.D. Wood, T. Itoi, and K. Takaori, *Pancreatic cancer*. Lancet, 2016. **388**(10039): p. 73-85.
155. Kleeff, J., M. Korc, M. Apte, C. La Vecchia, C.D. Johnson, A.V. Biankin, R.E. Neale, M. Tempero, D.A. Tuveson, R.H. Hruban, and J.P. Neoptolemos, *Pancreatic cancer*. Nat Rev Dis Primers, 2016. **2**: p. 16022.
156. Hirn, S., M. Semmler-Behnke, C. Schleh, A. Wenk, J. Lipka, M. Schaffler, S. Takenaka, W. Moller, G. Schmid, U. Simon, and W.G. Kreyling, *Particle size-dependent and surface charge-dependent biodistribution of gold nanoparticles after intravenous administration*. Eur J Pharm Biopharm, 2011. **77**(3): p. 407-16.
157. Duan, X. and Y. Li, *Physicochemical characteristics of nanoparticles affect circulation, biodistribution, cellular internalization, and trafficking*. Small, 2013. **9**(9-10): p. 1521-32.
158. Ernsting, M.J., M. Murakami, A. Roy, and S.D. Li, *Factors controlling the pharmacokinetics, biodistribution and intratumoral penetration of nanoparticles*. J Control Release, 2013. **172**(3): p. 782-94.

159. Decuzzi, P., B. Godin, T. Tanaka, S.Y. Lee, C. Chiappini, X. Liu, and M. Ferrari, *Size and shape effects in the biodistribution of intravascularly injected particles*. J Control Release, 2010. **141**(3): p. 320-7.
160. Yohan, D., C. Cruje, X. Lu, and D.B. Chithrani, *Size-Dependent Gold Nanoparticle Interaction at Nano-Micro Interface Using Both Monolayer and Multilayer (Tissue-Like) Cell Models*. Nanomicro Lett, 2016. **8**(1): p. 44-53.
161. Toy, R., P.M. Peiris, K.B. Ghaghada, and E. Karathanasis, *Shaping cancer nanomedicine: the effect of particle shape on the in vivo journey of nanoparticles*. Nanomedicine (Lond), 2014. **9**(1): p. 121-34.
162. Simone, E.A., T.D. Dziubla, and V.R. Muzykantov, *Polymeric carriers: role of geometry in drug delivery*. Expert Opin Drug Deliv, 2008. **5**(12): p. 1283-300.
163. Li, N., Q. Sun, Z. Yu, X. Gao, W. Pan, X. Wan, and B. Tang, *Nuclear-Targeted Photothermal Therapy Prevents Cancer Recurrence with Near-Infrared Triggered Copper Sulfide Nanoparticles*. ACS Nano, 2018. **12**(6): p. 5197-5206.
164. Zhang, L., C. Jiang, F. Zeng, H. Zhou, D. Li, X. He, S. Shen, X. Yang, and J. Wang, *A polymeric nanocarrier with a tumor acidity-activatable arginine-rich (R9) peptide for enhanced drug delivery*. Biomater Sci, 2020.
165. Pan, L., J. Liu, and J. Shi, *Cancer cell nucleus-targeting nanocomposites for advanced tumor therapeutics*. Chem Soc Rev, 2018. **47**(18): p. 6930-6946.
166. Sakiyama, Y., A. Mazur, L.E. Kapinos, and R.Y. Lim, *Spatiotemporal dynamics of the nuclear pore complex transport barrier resolved by high-speed atomic force microscopy*. Nat Nanotechnol, 2016. **11**(8): p. 719-23.
167. Otsuka, S., S. Iwasaka, Y. Yoneda, K. Takeyasu, and S.H. Yoshimura, *Individual binding pockets of importin-beta for FG-nucleoporins have different binding properties and different sensitivities to RanGTP*. Proc Natl Acad Sci U S A, 2008. **105**(42): p. 16101-6.

168. Pan, L., J. Liu, Q. He, L. Wang, and J. Shi, *Overcoming multidrug resistance of cancer cells by direct intranuclear drug delivery using TAT-conjugated mesoporous silica nanoparticles*. *Biomaterials*, 2013. **34**(11): p. 2719-30.

## **Vitae**

Maureen L. Aliru was born in Uganda and moved to Dallas, Texas in 2002 with her family. After completing her work at Skyline High School, Dallas, Texas in 2007, she attended Rice University in Houston, Texas. She received the degree of Bachelor of Science in Biomedical Engineering (BSBE) with a minor in Business in May, 2011. In May 2011, she began her MD/PhD training in the Medical Scientist Training Program at the combined University of Texas Medical School in Houston and UT MD Anderson Cancer Center Graduate School of Biomedical Sciences.